Crystal growth of ErN and ScN via physical vapor transport: synthesis, properties, characterization, and process simulation

by

Hayder Abdulkareem Mohsin Al-Atabi

B.S., the University of Technology, Iraq, 2004
M.S., the University of Technology, Iraq, 2007

AN ABSTRACT OF A DISSERTATION

submitted in partial fulfillment of the requirements for the degree

DOCTOR OF PHILOSOPHY

Department of Chemical Engineering
College of Engineering

KANSAS STATE UNIVERSITY
Manhattan, Kansas

2018

Abstract

Recently, the rare earth nitrides have received a considerable attention from theorists and experimentalists due to their potential applications in spintronic, piezoelectric, and thermoelectric devices. In this work, erbium nitride (ErN) and scandium nitride (ScN) crystals were grown and characterized experimentally, and the growth process was modeled and simulated.

Erbium nitride (ErN) is a rare earth nitride notable for its magnetic and optical properties. Here we report on its growth on a non-native substrate, tungsten foil, via physical vapor transport, and its characterization. The source material was erbium metal that was converted to ErN by heating in nitrogen. Subsequently, it was sublimed to form the ErN crystals. The operating conditions were 1620-1770 ^{o}C and 150-330 Torr in pure nitrogen. The growth rate increased exponentially with temperature with an activation energy of 508 kJ/mol, and inversely with pressure. X-ray diffraction revealed the ErN preferentially adopted a (100) orientation, the same as the dominant orientation of the tungsten sheet. The lattice constant was 4.853 Å. The crystal shapes and sizes were dependent on the temperature, as revealed by SEM and optical microscopy. The ErN crystals were highly faceted, bound by (100) and (111) crystal planes. The ErN compound deviated from stoichiometry: the Er:N atomic ratio ranged from 1:1.15 to 1:1.2 according to EDX and XPS elemental analysis. Raman spectra was in good agreement with theoretical predictions.

Scandium nitride single crystals (14–90 μm thick) were grown on tungsten (100) single crystal substrate by physical vapor transport in the temperature range of 1850-2000 ^{o}C and pressure of 15-35 Torr. Epitaxial growth was confirmed using in-plane ϕ scan and out-of-plane x-ray diffraction techniques which revealed that ScN exhibited cube-on-cube growth with a plane relationship ScN (001) || W (001) and normal direction ScN [100] || W [110]. Atomic force microscopy revealed the surface roughness decreased from 83 nm to 18 nm as the growth temperature was increased. X-ray diffraction (XRD) rocking curves widths decreased indicating the crystal quality improved with increasing growth temperature. The lowest XRC FWHM was 821 arcsec, which is so far the lowest value reported for ScN. Scanning electron microscopy (SEM) exhibited the formation of macrosteps and cracks on the crystal surface with latter due to the mismatch of ScN's and tungsten's coefficients of thermal expansion .

In general for crystal growth, material should deposit on the seed crystal and not on any adjacent supporting structures. This efficiently uses the source material and avoids the possibility of spurious polycrystals encroaching on, and interfering with the single crystal growth. To achieve this goal, a new crucible design with a cooling fin in contact with the seed was simulated and experimentally demonstrated on the physical vapor transport (PVT) crystal growth of scandium nitride. The heat transfer of the growth cavity for a conventional crucible and a modified crucible with the cooling fin were modeled theoretically via computational fluid dynamics (CFD) with FLUENT. The CFD results showed that the seed in the modified crucible was approximately 10 °C cooler than the crucible lid, while in the conventional crucible the temperature of the seed and lid were uniform. The experimental results showed that increasing the temperature gradient between the source and the seed by employing the cooling fin led to a dramatic increase in the growth rate of ScN on the seed and reduced growth on the lid. The relative growth rates were 80 % and 20 % on the seed and lid respectively, in the modified crucible, compared to 25% and 75% with the conventional crucible. Thus, the modified crucible improved the process by increasing the species transporting to the seed by sublimation.

Crystal growth of ErN and ScN via physical vapor transport: synthesis, properties, characterization, and process simulation

by

Hayder Abdulkareem Mohsin Al-Atabi

B.S., the University of Technology, Iraq, 2004
M.S., the University of Technology, Iraq, 2007

A DISSERTATION

submitted in partial fulfillment of the requirements for the degree

DOCTOR OF PHILOSOPHY

Department of Chemical Engineering
College of Engineering

KANSAS STATE UNIVERSITY
Manhattan, Kansas

2018

Approved by:

Major Professor
James H. Edgar

Copyright

Abstract

Recently, the rare earth nitrides have received a considerable attention from theorists and experimentalists due to their potential applications in spintronic, piezoelectric, and thermoelectric devices. In this work, erbium nitride (ErN) and scandium nitride (ScN) crystals were grown and characterized experimentally, and the growth process was modeled and simulated.

Erbium nitride (ErN) is a rare earth nitride notable for its magnetic and optical properties. Here we report on its growth on a non-native substrate, tungsten foil, via physical vapor transport, and its characterization. The source material was erbium metal that was converted to ErN by heating in nitrogen. Subsequently, it was sublimed to form the ErN crystals. The operating conditions were 1620-1770 ^{o}C and 150-330 Torr in pure nitrogen. The growth rate increased exponentially with temperature with an activation energy of 508 kJ/mol, and inversely with pressure. X-ray diffraction revealed the ErN preferentially adopted a (100) orientation, the same as the dominant orientation of the tungsten sheet. The lattice constant was 4.853 Å. The crystal shapes and sizes were dependent on the temperature, as revealed by SEM and optical microscopy. The ErN crystals were highly faceted, bound by (100) and (111) crystal planes. The ErN compound deviated from stoichiometry: the Er:N atomic ratio ranged from 1:1.15 to 1:1.2 according to EDX and XPS elemental analysis. Raman spectra was in good agreement with theoretical predictions.

Scandium nitride single crystals (14–90 µm thick) were grown on tungsten (100) single crystal substrate by physical vapor transport in the temperature range of 1850-2000 ^oC and pressure of 15-35 Torr. Epitaxial growth was confirmed using in-plane ϕ scan and out-of-plane x-ray diffraction techniques which revealed that ScN exhibited cube-on-cube growth with a plane relationship ScN (001) || W (001) and normal direction ScN [100] || W [110]. Atomic force microscopy revealed the surface roughness decreased from 83 nm to 18 nm as the growth temperature was increased. X-ray diffraction (XRD) rocking curves widths decreased indicating the crystal quality improved with increasing growth temperature. The lowest XRC FWHM was 821 arcsec, which is so far the lowest value reported for ScN. Scanning electron microscopy (SEM) exhibited the formation of macrosteps and cracks on the crystal surface with latter due to the mismatch of ScN's and tungsten's coefficients of thermal expansion .

In general for crystal growth, material should deposit on the seed crystal and not on any adjacent supporting structures. This efficiently uses the source material and avoids the possibility of spurious polycrystals encroaching on, and interfering with the single crystal growth. To achieve this goal, a new crucible design with a cooling fin in contact with the seed was simulated and experimentally demonstrated on the physical vapor transport (PVT) crystal growth of scandium nitride. The heat transfer of the growth cavity for a conventional crucible and a modified crucible with the cooling fin were modeled theoretically via computational fluid dynamics (CFD) with FLUENT. The CFD results showed that the seed in the modified crucible was approximately 10 °C cooler than the crucible lid, while in the conventional crucible the temperature of the seed and lid were uniform. The experimental results showed that increasing the temperature gradient between the source and the seed by employing the cooling fin led to a dramatic increase in the growth rate of ScN on the seed and reduced growth on the lid. The relative growth rates were 80 % and 20 % on the seed and lid respectively, in the modified crucible, compared to 25% and 75% with the conventional crucible. Thus, the modified crucible improved the process by increasing the species transporting to the seed by sublimation.

Table of Contents

List of Figures

List of Tables

Acknowledgement

I would like to first express my sincerest appreciation and thanks to Professor James H. Edgar, my major advisor, for his valuable advice, constant support, and effective guidance to be what I am today. I am indebted to him forever.

I wish to deeply thank Professor Mohammad H. Hosni, one of my advisory committee members, for allowing me to audit his heat transfer class, and for his advice which dramatically improved my research path.

I would also like to extend my thanks to my other advisory committee members: Dr. Placidus Amama, Dr. Bin Liu, and Outside Chair Professor Bradley Kramer for their contribution and feedback to improve this work.

I would like to thank all of the members of Prof. Edgar's group: Dr. Balabalaji Padavala, Dr. Clint Frye, Dr. Tim Hoffman, Jared Sperber, Dr. Song Liu, Eli Janzen, and Dylan Evans for assisting me when I faced difficulties with my research. Special thanks are to Jiahan Li, my lab mate, class mate, and friend, for his continuous help and support.

My thanks are also extended to all graduate students in the KSU chemical engineering department for assisting me in several aspects related to my lab work.

Special thanks and appreciations are to the former Iraqi Cultural Attaché, Professor Tahani Alsandook, for her great and continuous efforts devoted to help me succeed and earn the degree.

The Higher Committee for Education Development in Iraq (HCED) is gratefully acknowledged specially Mr. Zeyad T. Flayyeh, the director of student academic affairs department, and Mr. Firas Rafid Saleem.

I am grateful to the support staff in the Chemical Engineering Department at Kansas State University: David Threewit, Danita Deters, Karen Strathman, Debra Wahl, and Cynthia Fowler for their assistance and cooperation.

I wish also to thank the library staff at KSU for providing me with so many references and papers.

Finally, I wish to sincerely thank my dear wife, Dr. Zahraa Al-Auda, for her continuous support when I faced the most challenging times during my PhD journey.

This work was performed under the sponsorship of the National Science Foundation Division of Materials Research (award number 1508172) and Higher Committee for Education Development in Iraq (HCED).

Dedication

To my father in his second life

To my mother

To my brother and best friend, Wissam Al-Atabi

To my sisters, Riyam and Ayat

To my father-in-law, keeping supporting us
Fadhil Al-Auda

To my wife, my soulmate and life partner
Zahraa Al-Auda

To my children
Ghasaq and Ali

Chapter 1: Introduction and Background

1.1 Introduction

This research is a process development study on how best to prepare novel semiconductors, ScN and ErN. The technique employed to produce these materials, physical vapor transport, is novel and has not been widely used before for this purpose. This research involved determining how to grow these materials with high quality and a fundamental study of their most basic properties.

Crystal growth using physical vapor transport process allows one to grow thick layers and bulk materials, and has been studied as a way of growing crystalline materials having use in semiconductor devices such as SiC and AlN. However, several challenges have been identified with this technique. First, it can be difficult to achieve single-crystal epitaxial growth on substrates that are not structurally identical to the sublimed material. Often, this is due to a large lattice constant mismatch. Second, the sublimed materials may react with the crucible and the substrate which is attributed to the poor chemical or thermal stability toward the sublimed material. Third, it can be difficult getting the sublimed materials to deposit on the desired location. For instance, the sublimed material may crystallize on portions of the growth cavity, the crucible, instead of the substrate. This results in reduced crystal growth rates on the substrate and longer sublimation processing times. In this study, these problems were addressed. Tungsten metal was employed as a substrate for ErN and ScN crystal growth, and it proved its thermal and chemical stability at the extreme growth temperature. In addition, single crystal tungsten was used as a seed to achieve single-crystal epitaxial growth of ScN. The grown single crystal was in 45°

rotation with the seed, so the lattice mismatch was reduced to 0.3%. Furthermore, a specially configured crucible comprised of a heat transfer fin in a heat-conductive relationship with the tungsten seed was configured to produce a temperature gradient between the growth zone (the substrate) and the surrounding parts of the crucible; thus creating conditions favorable for selectively growing crystal on the substrate as opposed to the adjacent portions of the crucible.

The present work is also directed toward studying the fundamental properties of the produced crystals, their electrical, optical, thermal, structural, and mechanical properties.

1.2 Motivation

The transition elements represent the ***d*** and ***f*** blocks in the periodic table. ***f*** block elements are comprised of two series of inner transition elements which are the lanthanides or rare earths, atomic number from 57 (La) to 71 (Lu), and the actinides from 89 (AC) to 103 (Lr). Although Sc and Y fall in the ***d*** block, they are often considered in conjunction with rare earth elements because of their strong chemical similarities to the lanthanides.

The rare-earth elements (REs) represent the solely stable elements with more than marginally filled *f*-shell electronic orbitals; consequently, they hold the largest spin and orbital moments.[1] Due to their ionic charge of 3^+, they combine with the group $\mathbf{V}$ elements to form rare-earth monopnictides, REX (X=N, P, As, Sb, Bi).[1, 2] The heavier pnictides are antiferromagnetic, while the nitrides are almost all ferromagnetic.[3-5]

The rare-earth nitrides (RENs) have a wide range of properties. They form the rock salt structure (Figure 1.1) with lattice constants ranging from 4.76 Å for LuN to 5.305 Å for LaN.[1] The magnetic properties of RENs are especially of interest due to their unfilled and highly localized 4*f* orbitals.[6] The electron transport properties and band structures vary from semimetallic to semiconducting.[4] The uncertainty of transport properties is attributed to two issues that strongly affect their stoichiometry, a tendency to rapidly oxidize when exposed to air, and to form high concentrations of nitrogen vacancies (V_N).[1]

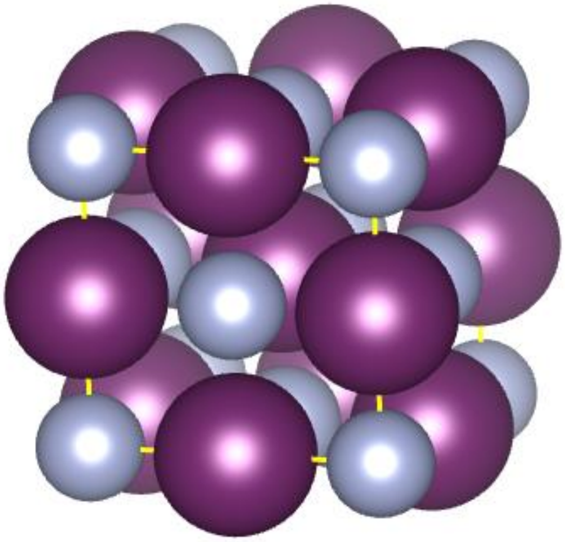

Figure 1.1*: The common rock salt crystal structure of the RENs. The large spheres represent the RE cations while the small spheres are the N anions.*

One reason for the interest in REN's is that the REN-based devices potentially can be amalgamated with group-III nitride semiconductors to develop new functionalities combining both families. Their optical absorption edges lie near 1 eV, and make the REN's applicable to IR detectors. Consequently, the properties of the RENs are compatible and complimentary with those of the wide band-gap group-III nitrides, and a heterojunction comprising the two semiconductors may possess very appealing properties for multi-wavelength photonic devices.[7, 8]

There have been many theoretical studies predicting the properties of RENs. Aerts *et al.*[9] predicted half-metallic (PrN-GdN), insulating (TbN- HoN) and semimetallic (ErN-YbN) behaviors might arise in the REN series. According to Larson *et al.,*[6] the LSDA+U approach, local spin density approximation plus Hubbard-like term, predicts that when only the U_f parameter is involved, the RENs have a small band overlap, thus they are semimetals.

Most studies of REN thin film growth have employed ultra-high vacuum-based methods (UHV) such as molecular beam epitaxy (MBE),[7, 8] pulsed-laser deposition (PLD),[10, 11] and dc/rf magnetron sputtering.[12-14] These techniques are the most common used for growing RE-based materials because high-vacuum and inert-gas ambient facilitates the production of pure and high quality materials. Furthermore, they do not require chemical reactants; the thin films are grown from elemental metals.

MBE has proven to be an excellent method to produce high quality of REN thin films such as GdN and EuN.[7, 15, 16] The epitaxial growths of GdN[7, 11] and SmN[11, 17] as well as polycrystalline films of DyN, ErN, LuN[18] were also produced by MBE. Commonly, solid sources are used for the RE elements, while several nitrogen sources are available. The simplest way is to rely on the catalytic breakdown effect of the RE atoms on the nitrogen molecules by the rare earth atoms.

The growth of EuN required the presence of radical nitrogen, such as using low energy nitrogen ions from a Kaufmann ion source or N_2 plasma.[19, 20] Other common nitrogen precursors are ammonia (NH3),[15, 16] which is decomposed on the surface of the substrate by pyrolysis, and nitrogen plasma obtained by radio-frequency or electron cyclotron resonance.[14, 21]

The lack of native substrates has been a major impediment to RENs epitaxial growth. Furthermore, the tendency of RE to react with silicon (in general the most common substrate for epitaxial and polycrystalline thin film studies) makes it unsuitable. Because the RENs adopt a rock salt (NaCl) crystal structure, (100) oriented substrates have been selected by most researchers. MgO (100) has been employed for the epitaxial growth of many RENs including ScN, TiN, CeN,[22] and GdN.[23] However, the lattice constant mismatch is quite large, +19.2 % and +18.7 % for CeN and GdN respectively, which results in large strains and high defect concentrations, adversely affecting the properties of the films.

Erbium nitride (ErN) and scandium nitride (ScN), belonging to the lanthanide nitrides, have interesting properties, so, potentially, they can be used for several applications. This project is to produce ErN and ScN crystals, study their crystal structure, crystal defects, crystal quality, and optical properties, and simulate the system behavior by CFD method.

1.3 ErN Literature Review

There have been very few studies of ErN. SciFinder scholar returns only 105 journal articles compared to more than 56,000 for GaN. The optical transition of electrons in the

4*f* electron orbital of erbium element is a key property of interest since it produces light at 1.54 µm, which corresponds to the absorption minimum in silica optical fiber. Hence a goal of many studies involving erbium has been to induce this transition electronically, by for example, incorporating erbium into a semiconductor such as silicon or gallium nitride.[24] This may also be possible in a novel, erbium nitride semiconductor, if it can be made with a high crystal quality and low residual impurity concentrations. In this case, the number of erbium atoms per volume would be much higher, since it is a major component of the binary semiconductor rather than just a dopant.

The ErN properties have been studied more in theory than experiment. Brown and Clark[25] studied experimentally the effect of N % composition of ErN powder and reported that the lattice constant decreased as the percent nitrogen content increased, from 4.848 Å to 4.843 Å for 92 at% N to 98 at% N, respectively (Figure 1.2). Table 1.1 summarizes some known ErN properties.

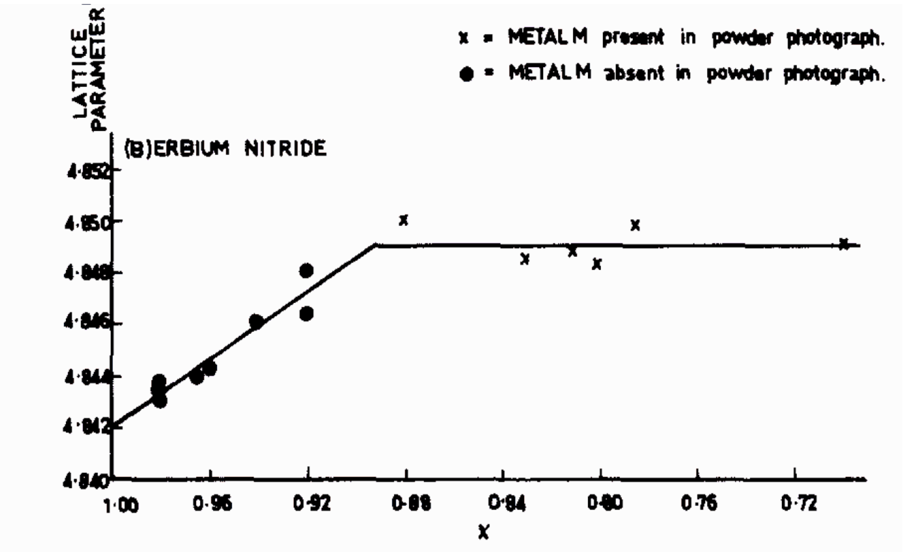

Figure 1.2: *Lattice parameter vs. elemental nitrogen concentration.*[25]

Table 1.1: *Properties of ErN crystal.*

Properties of ErN	
Crystal structure	Rock Salt (NaCl)
Lattice constant (Å)	4.842[26]
Energy bandgap (eV)	1.2, 1.3, 2.4[4, 27]
4*f* shell Optical transition wavelength (μm)	1.54[24]
Theoretical density based on lattice constant (gm/cm^3)	5.3

1.4 ScN Literature Review

ScN is of interest due to its excellent physical properties of high hardness, mechanical strength, and outstanding electronic transport properties. The heat free energy (ΔG_f^o = -60.5 kcal/mol) and heat of formation (ΔH_f^o = -71.2 kcal/mol) of ScN suggest its high thermal stability. Some of its interesting properties include: its melting point (≥ 2600 ^{o}C) making it suitable for high temperature Ohmic contact for the IIIA nitrides; it has a indirect bandgap 1.3 ± 0.3 eV, and a direct band gap of 2.4 ± 0.3;[28] and it's a good candidate as a substrate for growing a high quality gallium nitride (lattice constant is 4.54 Å) due to its low lattice constant mismatch (0.1 %).[29] ScN is also being investigated for thermoelectric and piezoelectric applications.[30] One of the most exciting aspects of ScN is that it can have both *n*-type and *p*-type conductivity.[31]

Most calculations suggest that ScN is a semiconductor with a considerable ionic character. Consequently, its electrical properties are sensitive to impurities, and the reported values have varied dramatically. The electrical resistivity of unintentional doped

ScN was reported as 25, 130, 308, and 461 μohm-cm by Samsonov *et al.*,[32] Sclar,[33] Gschneidner,[34] and Dismukes *et al*. (1970 and 1972)[35, 36] respectively.

ScN is unreactive to water, dilute mineral acids, alkali solutions, and air up to 550-600 °C. However, it is attacked by concentrated mineral acids and is readily oxidized at 700 °C and higher. Table 1.2 summarizes some properties of ScN.[37]

Table 1.2: *Properties of ScN crystal.*[37]

Property	Value
Crystal structure	Rock salt (NaCl)
Lattice constant (nm)	0.4503 ± 0.0002
Bandgap, Eg (eV)	1.3 ± 0.3 indirect and 2.4 ± 0.3 direct
Undoped conductivity type	n-type
Carrier concentration (cm^{-3})	10^{18}-10^{21}
Electron mobility (cm^2/V-s)	28-200
Resistivity (Ωcm)	2×10^{-6} – 0.6
Electron effective mass	0.1–0.2 m_o
Optical dielectric constant (Ɛ)	7 - 10.8
Infrared refractive index (at 400–8000 cm^{-1})	2.56
Young’s modulus (GPa)	270–356
Hardness (GPa)	21.1 ± 1.1
Poisson’s ratio	(0.188 – 0.2) ± 0.04
Thermal expansion coeff. (10^{-6}/°C)	4 – 8.68
T_{melt} (°C)	2,550 ± 50
Thermal conductivity (W/m K)	10 - 20
Oxidation resistance	Inert in air to temperatures of 600 °C
Seebeck coefficient (μV/K)	39 – 86

1.4.1 Microstructure and Electrical Properties of ScN

Burmistrova *et al.*[38] studied the microstructure and the electrical properties of ScN thin films sputtered onto MgO(001) substrates. The electrical resistivity, electron mobility, and carrier concentration (Figure 1.3) were measured for different deposition pressures. All samples showed *n*-type semiconducting behavior. The ScN thin film deposited at the lowest pressure (2 mTorr) yielded the highest electron mobility, while the electrical resistivity exhibited a proportional relationship to increasing pressure. These two inseparable trends, increasing the electrical resistivity and decreasing the electron mobility, could be attributed to the defect scattering. The ScN film crystallinity degraded as the deposition pressure was raised.

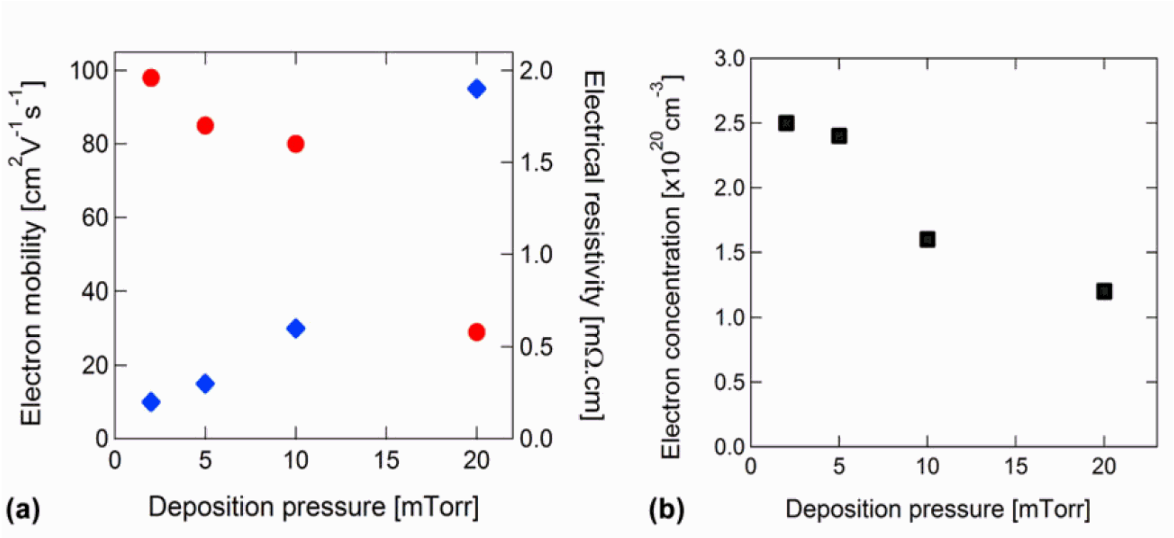

Figure 1.3: *(a) Electrical resistivity (blue diamond) and electron mobility (red circle), and (b) electron concentration of the ScN thin films as a function of the deposition pressure.*[38]

The carrier concentration was measured, and all of the ScN films grown at different pressures were in the degenerate range (> 10^{20} cm^{-3}). The carrier concentration slightly dropped with increasing deposition pressure, due to increased oxygen contamination in the ScN thin film which acts as a donor. Avoiding oxygen contamination is extremely difficult, so even if the base pressure is ultra-high vacuum, 1 % of oxygen can be associated with the film. Due to the high oxygen contamination, the Fermi energy shifted toward and into the conduction band (known as the Burstein–Moss shift[39]); thus leading to increasing the bandgap.

For thermoelectric applications, oxygen incorporation at low concentrations, about 1%, is an advantage, as it enhances the electrical conductivity while reducing the thermal conductivity of ScN thin films.[40]

1.4.2 Thermoelectric Properties of ScN

Based on cheap raw materials, ScN is a promising compound for thermoelectric devices,[30] which convert heat into electricity by generating a potential difference in response to a temperature gradients or vice versa. The efficiency of thermoelectric devices at a certain temperature is a function of the dimensionless figure of merit (ZT), where $Z=S^2/(\kappa\rho)$ and S, κ, and ρ are the Seebeck coefficient, the thermal conductivity, and the electrical resistivity, respectively. The maximum ZT occurs at the maximum of the parameter S^2/ρ, the power factor.[41]

ScN exhibits an anomalously high thermoelectric power factor.[38, 41] Kerdsongpanya *et al.*[41] reported a thermoelectric power factor of 2.5x10^{-3} W/mK^2 at 800K for epitaxial ScN thin films due to a relatively high Seebeck coefficient of ~-86 µV/K with low electrical resistivity of ~2.94 µΩm. Thus, this high power factor for a transition-metal nitrides places ScN-based materials among the most promising candidates for high temperature thermoelectric applications. Burmistrova *et al.*[40] in 2013 grew epitaxial ScN films at 650 °C exhibiting a remarkable thermoelectric power factors of 3.3–3.5x10^{-3} W/mK^2 in the temperature range of 600 K to 840 K.

Later in 2015, Burmistrova *et al.*[38] studied the effects of temperature and deposition pressure on the electrical conductivity, Seebeck coefficient, and power factor of ScN thin films shown in Figure 1.4. The electrical conductivity (Figure 1.4a) decreased with increasing either temperature or pressure.

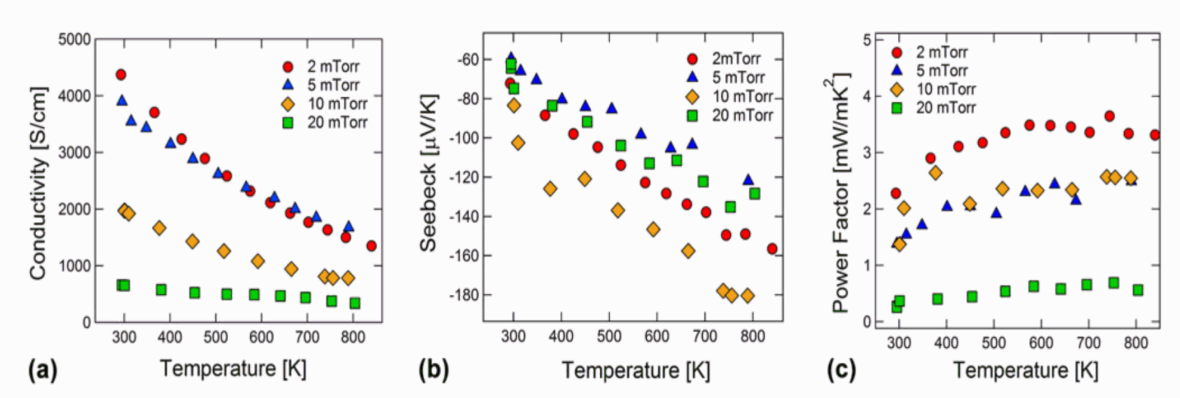

Figure 1.4: *Temperature dependent (a) electrical conductivity, (b) Seebeck coefficient, and (c) power factor of ScN thin films deposited at 2, 5, 10, and 20 mTorr.*[38]

The Seebeck coefficient (Figure 1.4b), however, was proportional to temperature, and the lowest Seebeck coefficient value was -180 µV/K at 800 K. The power factor also increased with increasing temperature (Figure 1.4c), it saturated after about 600 K, and the greatest value was 3.3 mW/mK^2 at 2 mTorr and 800 K

The thermal conductivity of ScN thin films, however, is in the range of 8–12 Wm^{-1}K^{-1}, [38, 42] so the reduced thermal conductivity would be required to enable application of ScN as a thermoelectric material. Several strategies are adopted for reducing the thermal conductivity.[30]

Alloy scattering is one of the standard strategies for thermoelectric materials for reduction of the lattice thermal conductivity.[30] Inclusion of heavy transition metals in ScN enables the reduction the thermal conductivity by an increase of the phonon scattering.[43] The 3d orbitals in Sc are empty, and can be utilized by delocalizing the electrons to reduce the electrical conductivity and the thermal conductivity due to alloy scattering.[30] Tureson *et al.*[43] studied the reduction of the thermal conductivity of ScN by Nb alloying. The Nb inserted ScN thin films exhibited a thermal conductivity as low as 2.2 Wm^{-1}K^{-1}, thus the reduction in the thermal conductivity was by a factor ~5 due to the mass contrast in ScN increasing the phonon scattering in the material.

Other approaches of reducing the thermal conductivity are superlattices, nanoinclusions, or grain boundaries.[44-47]

1.4.3 Piezoelectric Properties of ScN

ScN is also a potential compound for piezoelectric devices,[48] which is the ability of materials to generate an electric charge in response to applied mechanical pressure. Alloys of ScN, such as (Sc,Al)N, produces an extraordinarily high piezoelectric coupling coefficient.[48, 49] In general, piezoelectric materials with a higher Curie temperature possess a lower piezoelectric coefficient,[50, 51] that is the piezoelectric coefficient has an inverse relationship with the maximum use temperature. For instance, the piezoelectric coefficient of lead zirconium titanate (PZT), widely used in electronic devices, is 410 pCN^{-1} at Curie temperature of 250 ^{o}C.[52] The piezoelectric coefficient of aluminum nitride (AlN), a typical high temperature piezoelectric material, is 5.5 pCN^{-1} at a maximum use temperature of 1150 ^{o}C.[51] Akiyama *et al.*[48] produced $Sc_{0.43}Al_{0.57}N$ alloys exhibiting a high piezoelectric coefficient of 27.6 pNC^{-1}, about 500% higher than AlN. This is the highest piezoelectric coefficient among the tetrahedrally bonded semiconductors. This piezoelectricity was not changed by annealing at 500 ^{o}C for 56 h under vacuum. This achievement opens a new route to design this high-temperature piezoelectric material.

1.4.4 Optical Properties

Oshima *et al.*[53] studied the optical and electrical properties of ScN thin layer grow by (HVPE) method at 1050 ^{o}C. The transmittance (T), the reflectance (R), and the absorption coefficient (α) of a ScN(110) film (3.7 µm thick) are shown in Figure 1.5a as a function of the photon energy (hv). T and R are clearly oscillating due to the multiple reflections on both sides. α, estimated from T and R according to Gall *et al.*[54], increased steeply around 2.1 eV. There was no threshold observed around 0.9–1.3 eV, where the existence of the indirect transition is predicted. They also stated that the apparent (α) saturation above 2.1 eV was attributed to the decreasing of transmittance signal below the detection limit of the instrument for the relatively large film thickness. Consequently, the real (α) should have been higher. The band gap energy was determined to be 2.06 eV by plotting a linear fit to the absorption coefficient spectrum $(h\nu\alpha)^2$ vs hv (Figure 1.5b). The data for ScN(100) films showed no significant difference with the results of ScN(110) films.

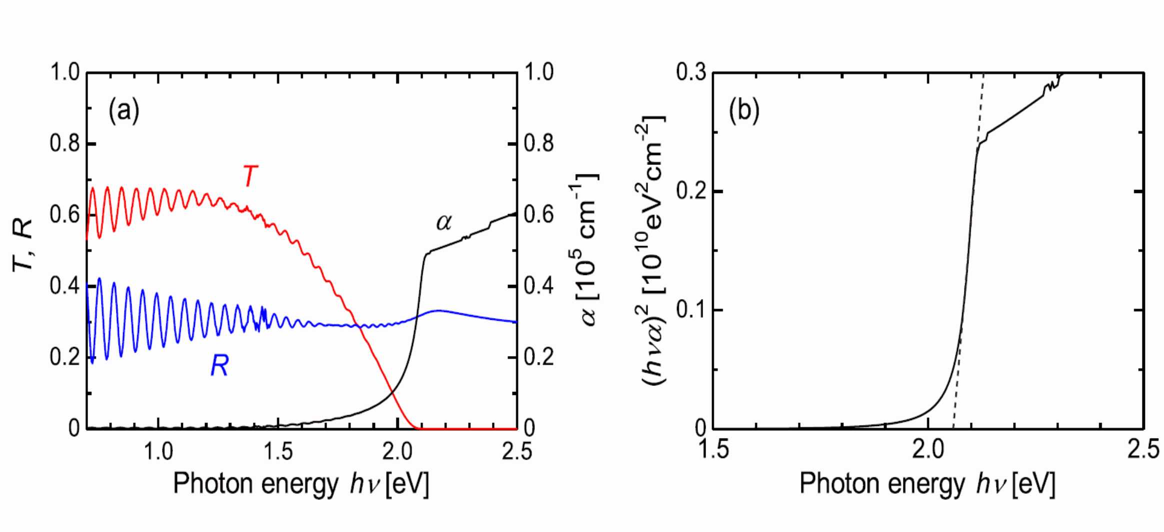

Figure 1.5: *(a) Transmittance and reflectance spectra of ScN (110), (b) Absorption coefficient in $(h\nu\alpha)^2$ vs hv plot.*[53]

Tables 1.3 and 1.4 summarize the recent studies of ScN and its measured structural, electrical, and thermal properties.

Table 1.3: *Recent studies of ScN properties by reactive magnetron sputtering method.*

Substrate and growth conditions	Orientation and Film thickness (μm)	FWHM of XRC (arcsec)	Electron mobility ($cm^2V^{-1}s^{-1}$)	Electrical resistivity (μΩm)	Carrier concentration (cm^{-3})	Seebeck coefficient (μVK^{-1})	Thermal conductivity (W/m-K)	Power Factor ($W/m\text{-}K^{-2}$)
Al_2O_3 (0001) at 800 °C[41]	(111) & (200) 0.18 μm			2.94 at 800K		-86 at 800K		$2.5x10^{-3}$
MgO(001) at 800 °C[40]	(001) 0.48-0.52 μm	2,430	106 at 300K	2.2 at 300K	$2.5x10^{20}$ at 300K	-70 to -156 at 300-840K	8.3 at 800K 20.7 at 300K	$(3.3\text{-}3.5)x10^{-3}$ at 600-840K
Sapphire (0001) at 950°C[43]	(111) 0.095-0.13 μm	2,700		3 at 750K	10^{21} at 300K	-45 at 750K	10.5 at 300K	$6x10^{-4}$
MgO(001) at 750°C[31]	(002) 0.3 μm	2,988		4 at 300K				
Sapphire(0001) at 400-700 °C[55]	(111) 0.2 μm			61-4 at 300K as growth temp. increased			5.4-10.5	
MgO(001) at 650 °C and (2-20) mTorr[38]	(001) 0.47-0.52 μm	1,762-3,960	98-29 as growth pressure increased	2-19 as growth pressure increased	$(2.5\text{-}1.2)x10^{20}$ as growth pressure increased	-120 to -180 at 800K as growth pressure increased		$(3.3\text{-}0.56)$ $x10^{-3}$ as growth pressure increased
MgO(001) at 750 °C[56]	(002) 0.3 μm	2,988		3-9 at 300-850K		-58 to -78 at 200-340K		$3x10^{-3}$ at 600-850K

Table 1.4: *Recent studies of ScN properties.*

Growth method	Substrate and growth condition	Orientation and Film thickness	FWHM of XRC (arcsec)	Electron mobility ($cm^2V^{-1}s^{-1}$)	Electrical resistivity (μΩm)	Carrier concentration (cm^{-3})	Band gap (eV)	hermal conductivity (W/m-K)
MBE[57]	$Sc_2O_3/Y_2O_3/Si(111)$ at 300-800°C	(111)&(200) 0.018-0.02 μm					2.2	
MBE[58]	MgO(100) at 300-850 °C	(100) 0.12-0.23 μm	2,340-1,260	50-130	1 - 5	10^{19}-10^{21}		
HVPE[53]	Various substrates of Sapphire and MgO at 1050°C	(100), (110), and (111) 0.4-40 μm		284		10^{18}-10^{20} at 300K	2.06	
GSMBE[37]	3C-SiC(111)/6H-SiC(0001) at 800-1050 °C	(111) 0.1-0.2 μm	1,047		100	5x10^{16} - 10^{20}	(1.4 - 1.6) ± 0.2	
Theoretical study[59]	DFT + U treatment. U is Hubbard-like term							51.5 at U=2.6eV 64.5 at U=7eV

1.5 Crystal Growth Mechanism

In the melt, solution, or vapor phase crystal growth, a seed crystal must be produced first. The seed formation process requires nucleation, which plays an important role in the process of crystal growth. In vapor deposition, the substrate serves as the seed crystal.[60, 61]

Three essential steps occur in the formation of a crystal from an initially disordered phase:[62]

1. Achievement of supersaturation or supercooling.
2. Nucleation.
3. Growth of the nuclei into single crystals of distinct phases.

1.5.1 Driving force

The conditions in any given system change according to the laws of thermodynamics in which the free energy of the whole system decreases. The growth of the crystal is promoted by the decrease in the free energy accompanying the crystallization process. The difference between the chemical potential of a melt, solution, or vapor phase and the chemical potential of the crystalline phase acts as a driving force towards crystal growth. In the nucleation stage, the atoms that are forming a surface or interface supply the energy needed for the next stage to grow crystals in distinct phase. After a nucleus forms and a crystal grows to a sufficient extent, the contribution of the interface energies becomes negligible. Thus, the difference in the bulk free energy in each phase (the crystal phase and the growth medium liquid or vapor) becomes the difference in the chemical potential.

In the vapor growth methods, crystal growth occurs when the species vapor pressure (*P*) is higher than the equilibrium or saturated vapor pressure (*Pe*). Then, the supersaturation level $\sigma=(P - Pe)/Pe$ becomes the driving force. The difference in the chemical potential ($\Delta\mu$) between the vapor phase and the crystal phase can be expressed as the following formula:[63]

$$\Delta\mu = k_B \mathrm{T} \log(\frac{p}{p_e}) = k_B \mathrm{T} \log(1 + \sigma) \quad (1)$$

Where:

T is the temperature and k_B is Boltzmann's constant.

1.5.2 Rate-determining process

Generally, there are three sequential steps to grow crystals which are:[63]

1. The volume diffusion process in which atoms and molecules in the growth medium are supplied to the growth interface or crystal surface.
2. The interface or surface kinetic process in which atoms and molecules are introduced to the crystal phase through the interface between the crystals and the growth medium.

3. Removing the latent heat generated at the growth interface or crystal surface during the crystallization process.

The growth rate is determined by the rate at which the crystals pass through each of these processes. The process that has the largest impact on the overall rate of growth is clearly the process in which the rate is the slowest. This particular process is therefore known as the *rate-determining process*. Exactly which of the processes becomes the rate-determining process depends on the growth environment and the growth conditions. To accurately identify the rate determining process, the points described below must be considered.

If the growth medium is vapor or solution, many of the crystals in it will grow as polyhedrons. In this case, the growth interface is flat on an atomic scale. Therefore, the rate-determining step is the interface kinetic process (step 2) because the crystal orientation time (surface diffusion) for this particular process is sufficiently long compared with both the atom-supply process (step 1) and the heat removal process (step 3). Process (1) can be ignored if a crystal grows in vapor because the concentration in the growth medium is sufficiently low, and thus volume diffusion can take place easily.

1.5.3 Vapor Growth

In the PVT growth method, the material sublimes and transports from the source toward the substrate surface as vapor. Atoms leaving the vapor phase and attaching to the surfaces of crystals on the substrate provide the crystals with almost all of their energy in the form of kinetic energy. Some atoms escape from the crystal surface to the vapor phase. To identify the atoms included within the crystal phase from those that are not, it is presumed that a sufficiently large number of atoms (*N*) incorporates to form a crystal. The decrease in potential energy (*ΔE*) resulting from interatomic binding can be calculated from the following equation:[63]

$$\frac{\Delta E}{N} = \frac{1}{2}\sum n_i \emptyset_i = \emptyset_{1/2} \tag{2}$$

Where:

$\emptyset_i$ is the binding energy of the nearest neighbor atoms with position $\acute{\imath}$.

$n_{\acute{\imath}}$ is the number of the nearest neighbor atoms for the atom at position $\acute{\imath}$.

The factor 1/2 indicates that two atoms binding to each other share the energy gain generated by their interatomic bonds. When atoms enter the surface of the crystals, they can be included within the crystal if the energy gain is larger than $\emptyset_{1/2}$. However, the atoms on the surfaces of crystals can escape to the vapor phase if they obtain energy larger than the adsorption energy from heat fluctuations.[64, 65]

The surface energies fall into three types: terrace (γ^T), edge (γ^E), and kink (γ^K) surface energies.[66]

On the actual surfaces of the crystals, the energy gain is $\phi_{1/2}$ i when an atom enters the kink site (K). Figure 1.6 shows the (001) plane of a simple cubic lattice which is also known as Kossel model. Each cube represents an atom or a growth unit. The energy gain principle (equation 2) can also apply to other different plane orientations or any plane in the other crystal lattices.[64, 65]

If atoms enter lattice points H (surface vacancies), the energy gain would be greater than when they enter at a kink position (K). The point H disappears once an atom enters it. Consequently, the chance of atoms entering the surface vacancies to contribute to the growth of the crystal is lost. Since the binding energy of atoms at the kink position is half of the internal atoms in the bulk crystal, the kink position is also called the half-crystal position.[63]

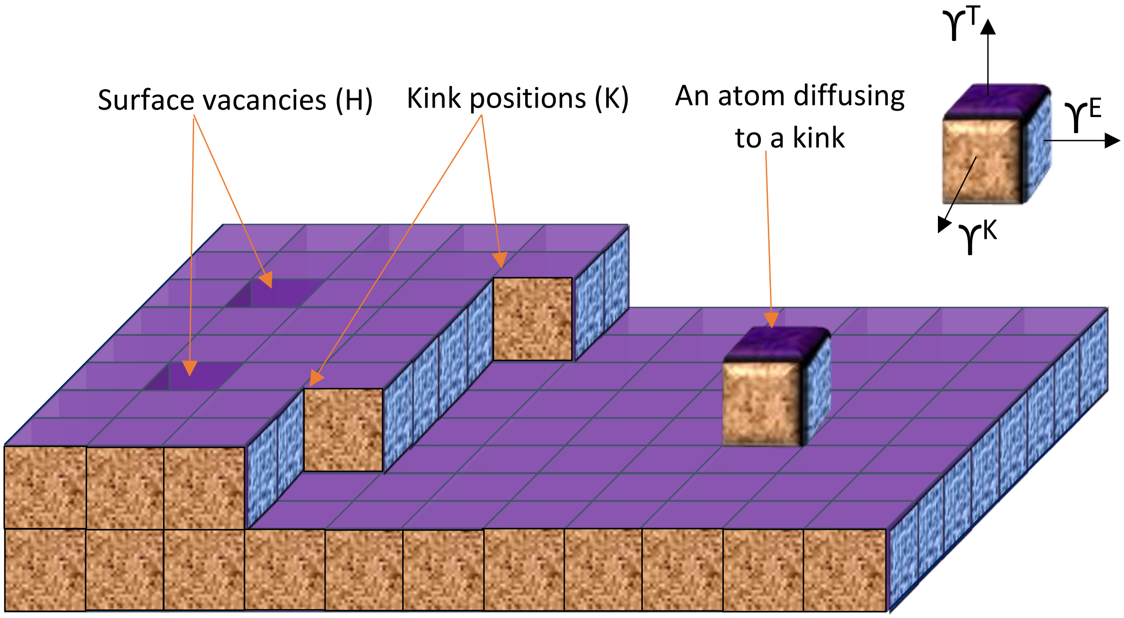

Figure 1.6: *Kossel model for the diffusion of an atom on the crystal surface.*

1.6 Crystal Growth Methods

Crystal growth is a chemical/physical process involving solid, liquid, or gas to produce high quality solid substances with a highly ordered, long range three-dimensional atomic arrangement. The crystal techniques can be broadly classified into three categories:

1. Solid-Solid such strain annealing.
2. Liquid-Solid aka melt method such as Bridgman-Stockbager and Czochralski or solution growth.
3. Gas-Solid such as chemical vapor deposition (CVD) and physical vapor transport (PVT).

The vast majority of commercial bulk semiconductor crystals are grown via melt methods. In case of a high melting temperature, bulk crystal growth from the melt is only possible under high pressure. For instance, stoichiometric SiC is estimated to melt only at 10,000 atm and 3500 ^oC. However, bulk crystal growth by physical vapor transport (PVT) is an alternative method when melt growth is difficult to conduct, such as when the melting point is too high, the material decomposes before it melts, or the melt reacts with the crucible.

Other advantages of the PVT method are:

1. It is near-thermodynamic equilibrium (producing high quality crystals).
2. It’s capable of growing very thick films and bulk crystals.

3. Since sublimation itself is a purification process, it's capable of growing very pure crystals.

1.6.1 The Physical Vapor Transport (PVT) or Sublimation Method

The seeded sublimation crystal growth technique (modified Lely method) has been widely used to produce wide bandgap semiconductor crystals such as silicon carbide and aluminum nitride,[67] as well as titanium nitride,[68] yttrium nitride,[69] and erbium nitride.[70] Recently, we also demonstrated the single crystals growth of the semiconductor scandium nitride (ScN), a group IIIB transition metal nitride, on single crystal tungsten (100) seeds via this method.[71]

Primarily, the sublimation method involves three stages: sublimation; transport; and deposition. The sublimation occurs by heating the solid source to high temperature (hot region) at a low pressure. The vapor species formed transport from the hot region (source) to the cold region (substrate) through a carrier gas, usually nitrogen or argon, and is driven by temperature and concentration differences. Finally, the deposition occurs on a substrate (cold region).

Figure 1.7 elucidates a typical PVT crystal growth system for metal nitrides. This method can be conducted in a tungsten furnace for metal nitrides because tungsten does not form stable nitrides, and is unreactive with several compounds such as AlN, ScN, YN, ErN, and TiN. The metal nitride source is placed in a crucible bottom. The following reversible reaction takes place inside the growth cavity:

$$REN_{(s)} \leftrightarrow RE_{(g)} + \frac{1}{2} N_{2(g)}$$

The solid REN sublimes dissociatively from the hotter zone in the crucible (REN source) via the forward reaction and deposits at the colder region (substrate) via the reverse reaction.

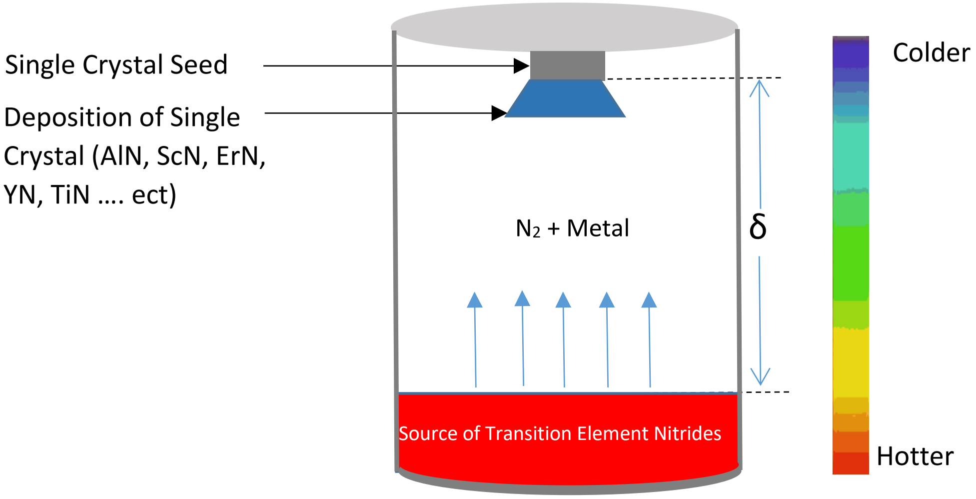

Figure 1.7: *Sublimation growth process.*

1.6.2 Modeling and Kinetic of Sublimation Growth

The kinetics and physical transport phenomena of the sublimation process are complicated and influenced significantly by the process parameters, including temperature, pressure, temperature gradient, the distance between the source and the deposition regions (δ in Figure 1.7), and the geometry. This method includes several physical phenomena, such as conduction, convection and radiation heat transfer, sublimation and condensation, Stefan flow, buoyancy force, mass transport of vapor species, and kinetics of dissociation and deposition.[72, 73] Since crystal growth experiments are expensive, modeling and simulation have become a powerful tool for research and for optimizing the growth processes conditions. In addition, it can provide additional insights into experiments, especially when it becomes difficult or impossible to directly measure parameters inside the reactor.[74]

Although crystal growth is frequently related to the materials chemistry and physics, the process fluid dynamics is also tremendously important. It controls the energy and mass transport, which in turn affect the crystal quality, strain, and impurity distribution. Enormous strides and advancements have been achieved with models for simulating the PVT process utilizing finite element-or finite volume-based software aided design. Therefore, modeling and simulation of the crystal growth processes have attained a point where they can reliably predict the fundamental physical phenomena of the process, and provide guidance for modifying the system design to improve the process.[72]

Liu and Edgar[75] studied the transport-only model for the aluminum nitride (AlN) system. In the transport-only model, Navier-Stokes equations were employed (equations 3 through 7). The sticking coefficient of nitrogen atom on the AlN surface was not considered in the transport-only model, while in the global model it was regarded.

$$\frac{\partial}{\partial r}\left(\frac{1}{r}\frac{\partial \varphi}{\partial r}\right) + A_r^2 \frac{1}{r}\frac{\partial^2 \varphi}{\partial z^2} = -\omega \qquad \mathit{Continuity} \qquad (3)$$

$$\frac{\partial C}{\partial t}+\frac{1}{r}\frac{\partial}{\partial r}(ru_rC)+A_r^2\frac{\partial}{\partial z}(u_zC)$$

$$=\frac{1}{Sc}\left[\frac{1}{r}\frac{1}{\partial r}\left(r\frac{\partial C}{\partial r}\right)+A_r^2\frac{\partial^2 C}{\partial z^2}\right] \qquad Coservation\ of\ mass \qquad (4)$$

$$\frac{\partial T}{\partial t}+\frac{1}{r}\frac{\partial}{\partial r}(ru_rT)+A_r^2\frac{\partial}{\partial z}(u_zT)$$

$$=\frac{1}{Pr}\left[\frac{1}{r}\frac{\partial}{\partial r}\left(r\frac{\partial T}{\partial r}\right)+A_r^2\frac{\partial^2 T}{\partial z^2}\right] \qquad Conservation\ of\ heat \qquad (5)$$

$$\frac{\partial \omega}{\partial t}+\frac{\partial}{\partial r}(u_r\omega)+A_r^2\frac{\partial}{\partial z}(u_z\omega)$$

$$=\left[\frac{\partial}{\partial r}\frac{1}{r}\frac{\partial}{\partial r}(r\omega)+A_r^2\frac{\partial^2\omega}{\partial z^2}\right]-Gr_T\frac{\partial T}{\partial r}$$

$$+Gr_s\frac{\partial C}{\partial r} \qquad Vorticity\ transport \qquad (6)$$

$$V_G=k\frac{\exp(A-B/T)}{P^{1.5}T^{1.2}}\frac{\Delta T}{L} \qquad Growth\ rate \qquad (7)$$

$$\alpha_{N_2}=k\ exp\left(-\frac{E}{RT}\right) \qquad Sticking\ coefficient \qquad (8)$$

$$J_i=\alpha_i\beta_i(p_i-p_i^*) \quad i=Al\ or\ N_2 \qquad Hertz-Knudsen \qquad (9)$$

$$V_G = \frac{J_{Al} M_{AlN}}{\rho_{AlN}} \qquad Growth\ rate \qquad (10)$$

Where:

φ is the stream function

ω is the vorticity

z is the dimensionless height

r is the dimensionless radius

A_r is the dimensionless geometric ratio

C is the dimensionless concentration of Al

t is the dimensionless time

u_r is the dimensionless velocity in r-direction

u_z is the dimensionless velocity in z-direction

Sc is Schmidt number

T is the dimensionless temperature

Gr is thermal Grashof number

Pr is Prandtl number

A and B are thermodynamic constants

J_i is the mole flux of species i

M_{AlN} *is the molecular weight of AlN*

P is the density of AlN

E is the activation energy

R is the universal gas constant

P^* *is the equilibrium pressure of species i and* $\beta_i = 1/\sqrt{2\pi M_i RT}$

Figure 1.8 compares the experimental and predicted results of the transport-only model of aluminum nitride crystal growth at a constant temperature of about 1840 ^oC and temperature gradient (ΔT/ΔL) of 3.53 $^oC/mm$ as a function of pressure. The model and experimental results agree well at the medium pressure and high pressure, but not at the lower pressure. That means the availability of aluminum is not the rate-control step of the growth. At the low system pressure, the pressure of N_2 is no longer much greater than that of aluminum. Since the sticking coefficient of N_2 is extremely low at the crystal surface[76], the availability of nitrogen atoms at the growing surface becomes the rate determining step. Therefore, a surface kinetic model considering the adsorption/desorption of Al and N_2 is necessary to simulate the growth rate precisely at low pressure.

Lui and Edgar[77] later in 2002 revised their transport-only model to be the global model (equation 8 through 10) by considering the sticking coefficient of N_2 on AlN surface, and equations 8 through 10 describe the growth rate process.

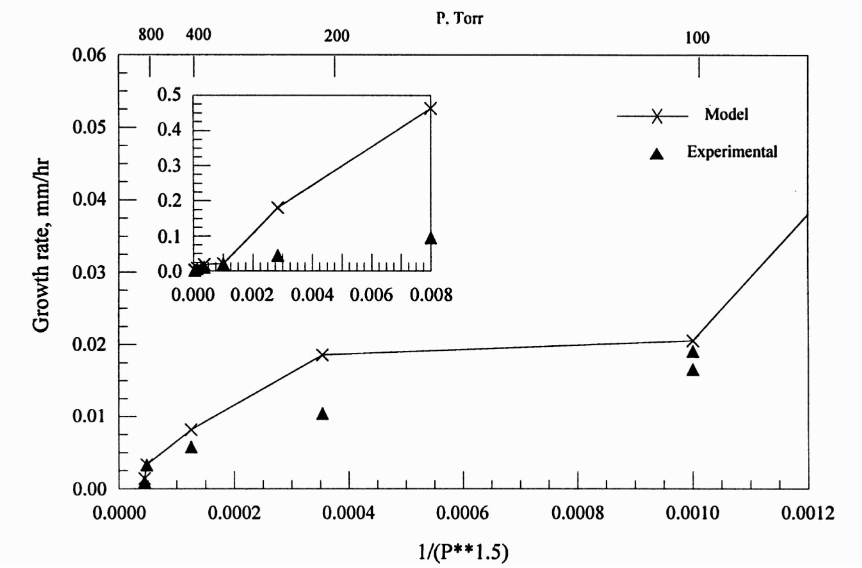

Figure 1.8*: Transport-only model. The growth rate as a function of the system pressure of AlN growth.*[75]

Figure 1.9 shows the effect of system pressure and the variation between the transport-only model and global model at 1800 °C. As is seen, there was a good agreement between the two models at pressures higher than 100 Torr, while at lower pressure the disagreement is evident. This disparity is attributed to the huge excess of N_2 at high pressure, thus causing the sticking coefficient of N_2 to have no effect. On the other hand, at low pressure, the concentration of N_2 becomes the determining growth step, then the N_2 sticking coefficient plays an important role in the growth process. The global model was validated by, and was in agreement with, the experimental results (Figure 1.10).

Chen *et al.*[78] modeled SiC crystal growth by the sublimation method. Figures 1.11a and b show how the rate has an Arrhenius-like dependence on the growth temperature at growth pressures ranging from 5-300 Torr. The growth rate deviates from Arrhenius-like behavior at high temperature, and this was attributed to the pressures at the seed and source being higher than the ambient pressure. In addition, comparing Figures 1.11a and b shows how the high temperature difference between the source and seed (ΔT) causes the Arrhenius-like behavior to shift towards the low temperature region. Consequently, the low temperature growth requires high axial temperature gradients.

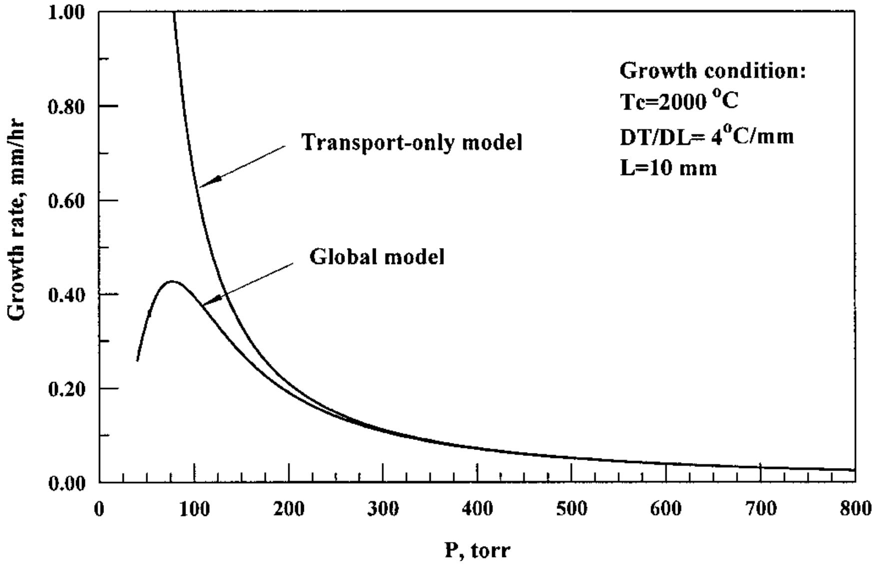

Figure 1.9*: Comparison of transport-only model and global model of AlN growth.*[77]

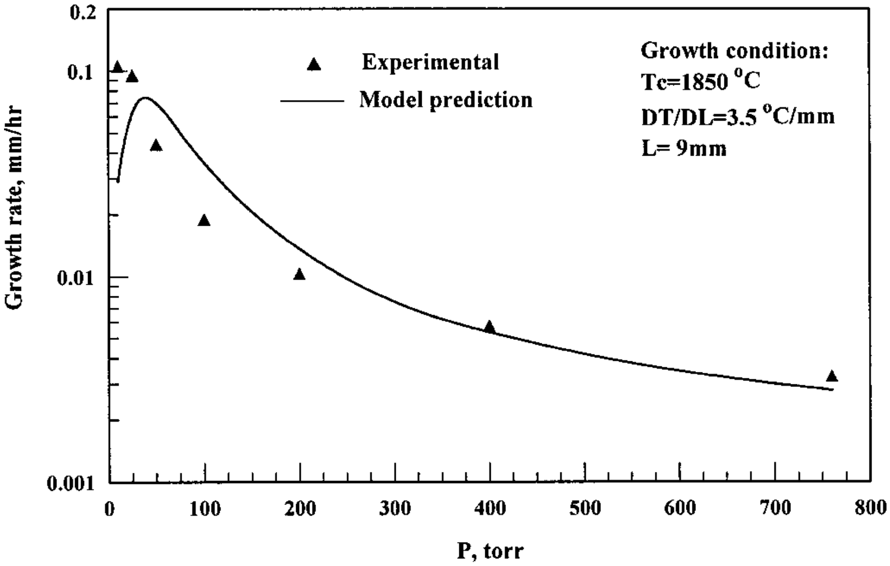

Figure 1.10*: Global model. The growth rate as a function of the system pressure.*[77]

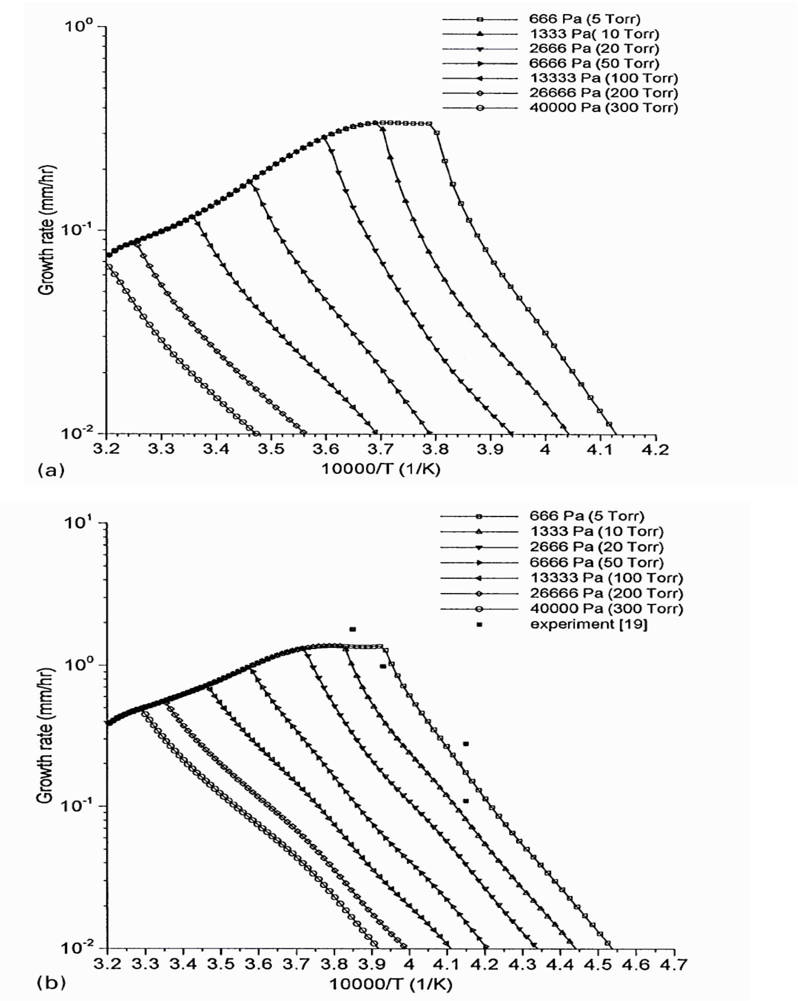

Figure 1.11: *Theoretical predicted growth rate versus temperature: (a) ΔT=2K/cm and (b) ΔT=20 K/cm.*[78]

Karpov *et al.*[79] studied the AlN system and stated that when the summation of Al and N_2 partial pressures is greater than the ambient pressure, the vapor would transport out of the crucible, and the growth fails (Figure 1.12). In other words, if the crucible is not properly sealed, the pressure inside the crucible will fluctuate because it will be higher than the ambient pressure.

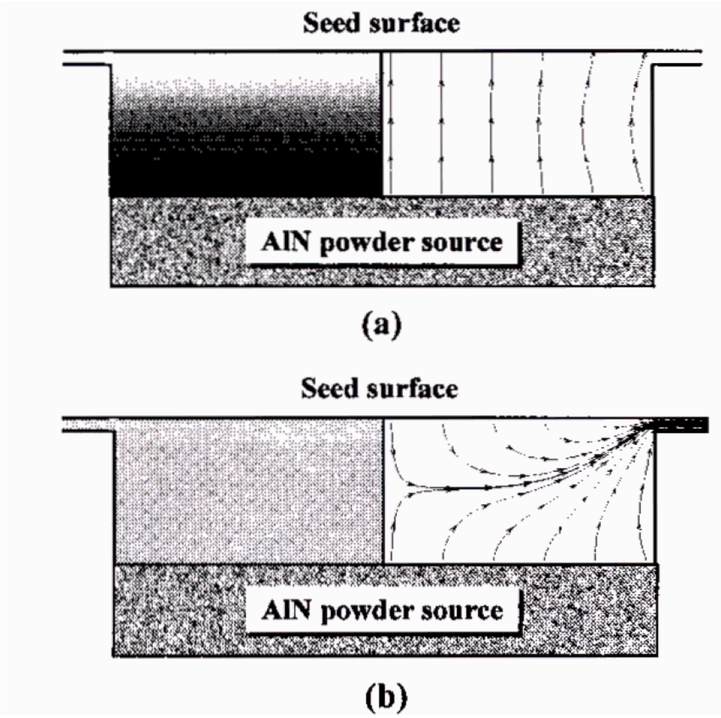

Figure 1.12: *Gas flow stream lines (right) and Al concentration (left) computed (a) for 0.2 atm and (b) for 0.1 atm. The color gradation from white to black corresponds to the increase of concentration.*[79]

Mokhav *et al.*[80] studied the effect of the temperature gradient (ΔT), growth temperature, and N_2 pressure on the sublimation seeded growth of AlN theoretically and experimentally. For large temperature gradients, the sublimation and growth rates increased exponentially with the growth temperature. On the other hand, at small ΔT the sublimation rate exhibited Arrhenius-like behavior, but the growth rate dropped (Figure 1.13), due to the high pressure inside the crucible (Figure 1.12).

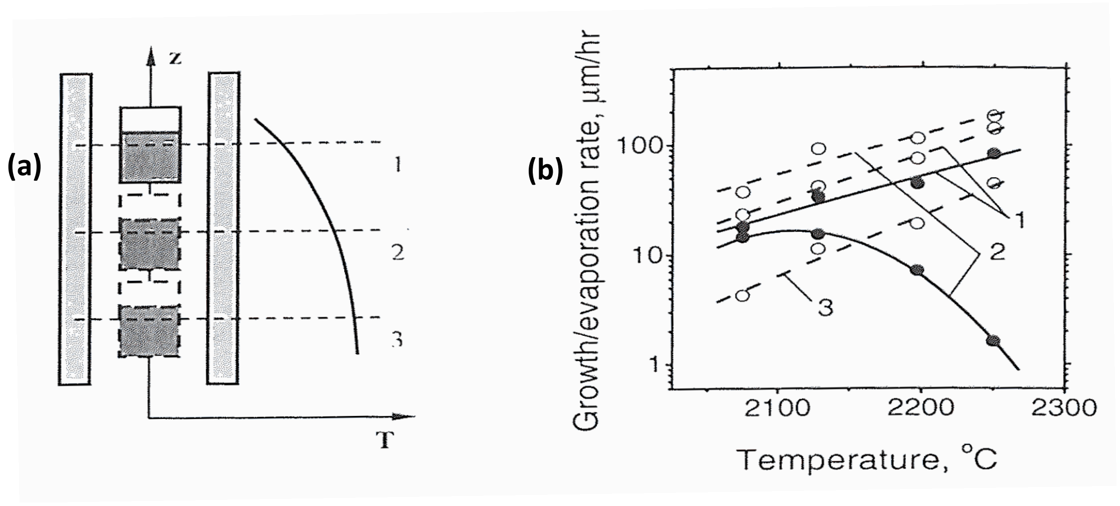

Figure 1.13: *(a) Three crucibles positions and qualitative axial temperature distribution in the furnace, and (b) rate of the AlN powder source evaporation (dash lines, open circles) and crystal growth (solid lines and circles) vs. temperature.*[80]

1.6.3 The Crucible Design Effect on the Growth Rate

Tsvetkov[81] stated that slight changes in the crucible design produce differences in the crystal shapes and the densities of defects formed due to modifications of temperature and temperature gradients inside the crucible. This temperature variation can also change the growth rate over the seed.

In chapter five of this thesis, the effect of the crucible design on the growth rate is reported. To improve the process efficiency, the goal was to get the sublimed material to deposit only at the desired location, the seed crystal. If the temperature is uniform, the sublimed material may crystallize on portions of the growth cavity (the crucible wall and lid) instead of the seed. Not only does this reduce the process efficiency, but material not deposited on the seed is polycrystalline, thus it can interfere with single crystal growth, if it overgrows the seed.

A new crucible was designed to selectively grow ScN crystal on the seed by exploiting the heat transfer phenomenon inside the growth cavity. The specially configured crucible design was comprised of a heat transfer fin in a heat-conductive relationship with the seed. The cooling fin cools the seed surface and increases the temperature gradient between it and its surroundings thereby presenting more favorable conditions for crystal growth. This leads to higher growth rate on the seed. This new design is applicable to all PVT seeded growth, including wide bandgap crystals such as silicon carbide and aluminum nitride.

1.6.3.1 Fin Purpose

The convective removal of heat from a surface is improved by extending the fins to increase its area.[82] The fin geometries can be of a variety of shapes such as plain, wavy, or interrupted , and can be attached to the inside, outside, or both sides of circular, flat, or oval surfaces. Fins are primarily utilized to increase the surface area when the heat transfer coefficient on that fluid side is relatively low so that the total rate of heat transfer increases. In addition, enhanced fin geometries, such as triangular wavy fins, also increase the heat transfer coefficient compared to that for a plain fin. The fins can attached to the heat transfer surface by several ways such as brazing, soldering, welding, adhesive bonding, or mechanical expansion (press fit) or extruded or integrally connected to the surface.[83]

References

1. Franck Natali, Ben J. Ruck, Natalie OV Plank, H. Joe Trodahl, Simon Granville, Claire Meyer and Walter RL Lambrecht, Progress in Materials Science 58, 1316 (2013).

2. Chun-Gang Duan, RF Sabirianov, Wai-Ning Mei, Peter A. Dowben, SS Jaswal and Evgeny Y. Tsymbal, Journal of Physics: Condensed Matter 19, 315220 (2007).

3. F. Hulliger, J Magn Magn Mater 8, 183 (1978).

4. F. Hulliger, Handbook on the physics and chemistry of rare earths 4, 153 (1979).

5. O. Vogt and K. Mattenberger, Lanthanides/actinides: physics-1, magnetic measurements on rare earth and actinide monopnictides and monochalcogenides 17, (1993).

6. P. Larson, Walter RL Lambrecht, Athanasios Chantis and Mark van Schilfgaarde, Physical Review B 75, 045114 (2007).

7. F. Natali, NOV Plank, J. Galipaud, BJ Ruck, HJ Trodahl, F. Semond, S. Sorieul and L. Hirsch, J. Cryst. Growth 312, 3583 (2010).

8. TF Kent, J. Yang, L. Yang, MJ Mills and RC Myers, Appl. Phys. Lett. 100, 152111 (2012).

9. CM Aerts, Paul Strange, M. Horne, WM Temmerman, Zdzislawa Szotek and Axel Svane, Physical Review B 69, 045115 (2004).

10. BJ Ruck, HJ Trodahl, JH Richter, JC Cezar, F. Wilhelm, A. Rogalev, VN Antonov, Binh Do Le and Claire Meyer, Physical Review B 83, 174404 (2011).

11. Franck Natali, Bart Ludbrook, Jules Galipaud, Natalie Plank, Simon Granville, Andrew Preston, Bin Le Do, Jan Richter, Ian Farrell and Roger Reeves, physica status solidi (c) 9, 605 (2012).

12. RM Osgood III, JE Pearson, CH Sowers and SD Bader, J. Appl. Phys. 84, 940 (1998).

13. Hiroaki Yoshitomi, Shinya Kitayama, Takashi Kita, Osamu Wada, M. Fujisawa, Hitoshi Ohta and T. Sakurai, Physical Review B 83, 155202 (2011).

14. Reddithota Vidyasagar, Shinya Kitayama, Hiroaki Yoshitomi, Takashi Kita, Takahiro Sakurai and Hitoshi Ohta, The European Physical Journal B: Condensed Matter and Complex Systems 86, 1 (2013).

15. Franck Natali, BJ Ruck, HJ Trodahl, S. Vezian, B. Damilano, Y. Cordier, F. Semond and Claire Meyer, Physical Review B 87, 035202 (2013).

16. Michael A. Scarpulla, CS Gallinat, S. Mack, JS Speck and AC Gossard, J. Cryst. Growth 311, 1239 (2009).

17. Eva-Maria Anton, BJ Ruck, Claire Meyer, F. Natali, Harry Warring, Fabrice Wilhelm, Andrei Rogalev, VN Antonov and HJ Trodahl, Physical Review B 87, 134414 (2013).

18. S. Granville, C. Meyer, ARH Preston, BM Ludbrook, BJ Ruck, HJ Trodahl, TR Paudel and WRL Lambrecht, Physical Review B 79, 054301 (2009).

19. Franck Natali, Bart Ludbrook, Jules Galipaud, Natalie Plank, Simon Granville, Andrew Preston, Bin Le Do, Jan Richter, Ian Farrell and Roger Reeves, physica status solidi (c) 9, 605 (2012).

20. K. Shimomoto, J. Ohta, T. Fujii, R. Ohba, A. Kobayashi, M. Oshima and H. Fujioka, J. Cryst. Growth 311, 4483 (2009).

21. Hiroaki Yoshitomi, Shinya Kitayama, Takashi Kita, Osamu Wada, M. Fujisawa, Hitoshi Ohta and T. Sakurai, Physical Review B 83, 155202 (2011).

22. T-Y Lee, D. Gall, C-S Shin, N. Hellgren, I. Petrov and JE Greene, J. Appl. Phys. 94, 921 (2003).

23. JW Gerlach, J. Mennig and B. Rauschenbach, Appl. Phys. Lett. 90, 061919 (2007).

24. JM Zavada, SX Jin, N. Nepal, JY Lin, HX Jiang, P. Chow and B. Hertog, Appl. Phys. Lett. 84, 1061 (2004).

25. RC Brown and NJ Clark, Journal of Inorganic and Nuclear Chemistry 36, 2507 (1974).

26. Giorgio L. Olcese, Journal of Physics F: Metal Physics 9, 569 (1979).

27. F. Bommeli, L. Degiorgi and P. Wachter, J Magn Magn Mater 140, 1159 (1995).

28. D. Gall, M. Städele, Kenneth Järrendahl, I. Petrov, P. Desjardins, RT Haasch, T-Y Lee and JE Greene, Physical Review B 63, 125119 (2001).

29. Zheng Gu, JH Edgar, J. Pomeroy, M. Kuball and DW Coffey, J. Mater. Sci. : Mater. Electron. 15, 555 (2004).

30. Per Eklund, Sit Kerdsongpanya and Björn Alling, Journal of Materials Chemistry C 4, 3905 (2016).

31. Bivas Saha, Magnus Garbrecht, Jaime A. Perez-Taborda, Mohammed H. Fawey, Yee Rui Koh, Ali Shakouri, Marisol Martin-Gonzalez, Lars Hultman and Timothy D. Sands, Appl. Phys. Lett. 110, 252104 (2017).

32. GV Samsonov, MD Lyutaya and VS Neshpor, Zh.Prikl.Khim. 36, (1963).

33. N. Sclar, J. Appl. Phys. 35, 1534 (1964).

34. JR GSCHNEIDNER In: C. T. Horovitz, Scandium : its occurrence, chemistry, physics, metallurgy, biology, and technology, (London; New York : Academic Press, London; New York, 1975), p. 165.

35. JP Dismukes, WM Yim, JJ Tietjen and RE Novak, RCA Rev 31, 680 (1970).

36. JP Dismukes, WM Yim and VS Ban, J. Cryst. Growth 13, 365 (1972).

37. Sean W. King, Robert F. Davis and Robert J. Nemanich, Journal of Vacuum Science & Technology A: Vacuum, Surfaces, and Films 32, 061504 (2014).

38. Polina V. Burmistrova, Dmitri N. Zakharov, Tela Favaloro, Amr Mohammed, Eric A. Stach, Ali Shakouri and Timothy D. Sands, J. Mater. Res. 30, 626 (2015).

39. Elias Burstein, Physical Review 93, 632 (1954).

40. Polina V. Burmistrova, Jesse Maassen, Tela Favaloro, Bivas Saha, Shuaib Salamat, Yee Rui Koh, Mark S. Lundstrom, Ali Shakouri and Timothy D. Sands, J. Appl. Phys. 113, 153704 (2013).

41. Sit Kerdsongpanya, Ngo Van Nong, Nini Pryds, Agnė Žukauskaitė, Jens Jensen, Jens Birch, Jun Lu, Lars Hultman, Gunilla Wingqvist and Per Eklund, Appl. Phys. Lett. 99, 232113 (2011).

42. Vijay Rawat, Yee Kan Koh, David G. Cahill and Timothy D. Sands, J. Appl. Phys. 105, 024909 (2009).

43. Nina Tureson, Ngo Van Nong, Daniele Fournier, Niraj Singh, Somnath Acharya, Susann Schmidt, Laurent Belliard, Ajay Soni, Arnaud Le Febvrier and Per Eklund, J. Appl. Phys. 122, 025116 (2017).

44. Christopher J. Vineis, Ali Shakouri, Arun Majumdar and Mercouri G. Kanatzidis, Adv Mater 22, 3970 (2010).

45. Ali Shakouri, Annual Review of Materials Research 41, 399 (2011).

46. Eric S. Toberer, Lauryn L. Baranowski and Chris Dames, Annual Review of Materials Research 42, 179 (2012).

47. Kanishka Biswas, Jiaqing He, Qichun Zhang, Guoyu Wang, Ctirad Uher, Vinayak P. Dravid and Mercouri G. Kanatzidis, Nature chemistry 3, 160 (2011).

48. Morito Akiyama, Toshihiro Kamohara, Kazuhiko Kano, Akihiko Teshigahara, Yukihiro Takeuchi and Nobuaki Kawahara, Adv Mater 21, 593 (2009).

49. Miguel A. Caro, Siyuan Zhang, Tommi Riekkinen, Markku Ylilammi, Michelle A. Moram, Olga Lopez-Acevedo, Jyrki Molarius and Tomi Laurila, Journal of Physics: Condensed Matter 27, 245901 (2015).

50. Shujun Zhang, Ru Xia, Laurent Lebrun, Dean Anderson and Thomas R. Shrout, Mater Lett 59, 3471 (2005).

51. RC Turner, Pa A. Fuierer, RE Newnham and TR Shrout, Appl. Acoust. 41, 299 (1994).

52. Yasuyoshi Saito, Hisaaki Takao, Toshihiko Tani, Tatsuhiko Nonoyama, Kazumasa Takatori, Takahiko Homma, Toshiatsu Nagaya and Masaya Nakamura, Nature 432, 84 (2004).

53. Yuichi Oshima, Encarnación G. Víllora and Kiyoshi Shimamura, J. Appl. Phys. 115, 153508 (2014).

54. D. Gall, I. Petrov, LD Madsen, J-E Sundgren and JE Greene, Journal of Vacuum Science & Technology A: Vacuum, Surfaces, and Films 16, 2411 (1998).

55. Sit Kerdsongpanya, Olle Hellman, Bo Sun, Yee Kan Koh, Jun Lu, Ngo Van Nong, Sergei I. Simak, Björn Alling and Per Eklund, Physical Review B 96, 195417 (2017).

56. Bivas Saha, Jaime Andres Perez-Taborda, Je-Hyeong Bahk, Yee Rui Koh, Ali Shakouri, Marisol Martin-Gonzalez and Timothy D. Sands, Physical Review B 97, 085301 (2018).

57. L. Lupina, MH Zoellner, T. Niermann, B. Dietrich, G. Capellini, SB Thapa, M. Haeberlen, M. Lehmann, P. Storck and T. Schroeder, Appl. Phys. Lett. 107, 201907 (2015).

58. Takeshi Ohgaki, Ken Watanabe, Yutaka Adachi, Isao Sakaguchi, Shunichi Hishita, Naoki Ohashi and Hajime Haneda, J. Appl. Phys. 114, 093704 (2013).

59. Chunhua Li and David Broido, Physical Review B 95, 205203 (2017).

60. S. Haussühl, Berichte der Bunsengesellschaft für physikalische Chemie 78, 1276 (1974).

61. Alexander A. Chernov, Modern crystallography III: crystal growth, (Springer Science & Business Media, 2012),

62. Govindhan Dhanaraj, Kullaiah Byrappa, Vishwanath Prasad and Michael Dudley, Springer handbook of crystal growth, (Springer Science & Business Media, 2010),

63. Kullaiah Byrappa and Tadashi Ohachi, Crystal growth technology, (Elsevier, 2003),

64. Iwan N. Stranski, Zeitschrift für physikalische Chemie 136, 259 (1928).

65. W. Kossel, Nachrichten von der Gesellschaft der Wissenschaften zu Göttingen, Mathematisch-Physikalische Klasse 1927, 135 (1927).

66. Carl J. Tilbury, Daniel A. Green, William J. Marshall and Michael F. Doherty, Crystal Growth & Design 16, 2590 (2016).

67. B. Liu, JH Edgar, Z. Gu, D. Zhuang, B. Raghothamachar, M. Dudley, A. Sarua, Martin Kuball and HM Meyer III, Materials Research Society Internet Journal of Nitride Semiconductor Research 9, (2004).

68. Li Du, James H. Edgar, Edward A. Kenik and Harry Meyer, J. Mater. Sci. : Mater. Electron. 21, 78 (2010).

69. Li Du, JH Edgar, Roberta A. Peascoe-Meisner, Yinyan Gong, Silvia Bakalova and Martin Kuball, J. Cryst. Growth 312, 2896 (2010).

70. Hayder A. Al Atabi, Zahraa F. Al Auda, B. Padavala, M. Craig, K. Hohn and James H. Edgar, Cryst. Growth Des. 18, 3762 (2018).

71. Hayder A. Al Atabi, N. Khan, E. Nour, J.Mondoux, Y. Zhang, and J.H. Edgar, Appl. Phys. Lett. (2018).

72. Qisheng Chen, Yanni Jiang, Junyi Yan and Ming Qin, Progress in Natural Science 18, 1465 (2008).

73. Ronghui Ma, Hui Zhang, Vish Prasad and Michael Dudley, Cryst. Growth Des. 2, 213 (2002).

74. M. Pons, M. Anikin, K. Chourou, JM Dedulle, R. Madar, E. Blanquet, A. Pisch, C. Bernard, P. Grosse and C. Faure, Materials Science and Engineering: B 61, 18 (1999).

75. Lianghong Liu and James H. Edgar, J. Cryst. Growth 220, 243 (2000).

76. S. Yu Karpov and MA Maiorov, Surf. Sci. 393, 108 (1997).

77. Lianghong Liu and JH Edgar, J. Electrochem. Soc. 149, G12 (2002).

78. Q-S Chen, H. Zhang, V. Prasad, CM Balkas, NK Yushin and S. Wang, J. Cryst. Growth 224, 101 (2001).

79. S. Yu Karpov, AV Kulik, MS Ramm, EN Mokhov, AD Roenkov, Yu A. Vodakov and Yuri N. Makarov, 353, 779 (2001).

80. EN Mokhov, SN Smirnov, AS Segal, D. Bazarevskiy, Yuri N. Makarov, MG Ramm and Heikki Helava, 457, 1545 (2004).

81. Valeri F. Tsvetkov, RC Glass, D. Henshall, D. Asbury and Calvin H. Carter Jr, 264, 3 (1998).

82. John H. Lienhard, A heat transfer textbook, (Courier Corporation, 2013),

83. Warren M. Rohsenow, James P. Hartnett and Young I. Cho, Handbook of heat transfer, (McGraw-Hill New York, 1998),

84. LJ Huang and RK Shah, Int J Heat Fluid Flow 13, 282 (1992).

Chapter 2: The Experimental Work and Process Simulation

2.1 System Description

In this work, ErN and ScN were grown in a tungsten furnace reactor. Photos of the whole furnace system are shown in Figure 2.1. Tungsten metal had previously proved to be a good unreactive metal for the sublimation growth of AlN [1], TiN [2], and YN [3]. The maximum temperature of the furnace is 2400 ^{o}C. The furnace chamber is made of stainless steel. Tungsten wire mesh heating elements are configured to heat a tungsten crucible to a temperature sufficient to sublime the metal nitride source (ErN or ScN). Eight layers of tungsten plate surrounding the heating elements acted as thermal shields to contain the heat generated, so extreme temperatures could be reached. Surrounding the heat shield was a cooling system, consisting of a shell and tube copper jacket heat exchanger. It is placed between the thermal shields and the stainless steel chamber walls and ensured the outside chamber wall temperature was at room temperature. The metal nitride source (ErN or ScN) was placed in the tungsten crucible with a 25 mm i.d., 30 mm o.d., and 50 mm long.

To provide an axial temperature difference, the driving force of the growth, between the metal source and the growth zone, the top of the crucible was not insulated by the tungsten thermal shields. Thus, it was colder than the crucible bottom. Figure 2.2 presents a detailed schematic of the furnace chamber.

Two thermocouples are positioned in the chamber. One is connected to a Honeywell UDC2000 controller which turns off the furnace automatically if the temperature exceeds the limit of the furnace. It is located between the heating shields.

Figure 2.1: *Pictures of the tungsten furnace apparatus showing the front and back sides.*

The other is connected to a Honeywell UDC3000 controller and is located close to the crucible inside the heating elements region. This thermocouple functions as a sensor to control the programmed temperature for heating or cooling the furnace. The growth temperature is measured via a pyrometer which is focused on the top of the crucible where the crystal growth takes place. The pyrometer and the thermocouple in the heating elements region are calibrated to facilitate setting the growth temperature.

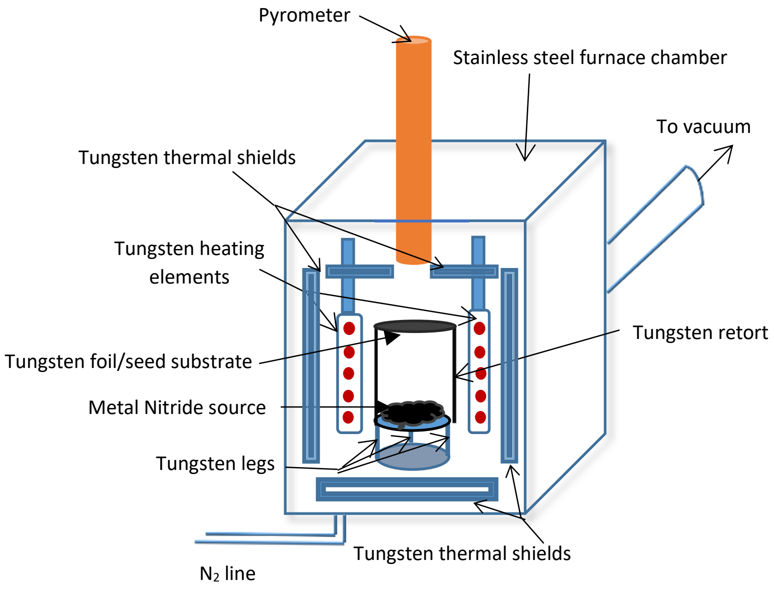

Figure 2.2: *The growth chamber of the furnace*

Ultra-high-purity gases, nitrogen (99.999% N_2) and forming gas (95% Ar and 5% H_2), were used in the experiments. The nitrogen and forming gases were further purified with three inline purifiers: a moisture purifier, a high oxygen concentration purifier in ppm level, and low oxygen concentration purifier in ppb level before the gas (either nitrogen or forming gas) enters the furnace chamber.

The ScN source, the crucible, and the substrate were baked at 1000 ^{o}C for two hours in forming gas to reduce and to remove oxygen present as native oxides on their surfaces. Then, the furnace chamber was cooled down to the room temperature, and the gas line was switched to nitrogen and purged several times to remove any forming gas from the system before starting the growth experiments in the nitrogen environment. However, in the ErN experiments the baking process was not performed because ErN was reactive to the forming gas.

Prior to growth, the metal sources were nitridized. The ScN source was synthesized by heating small chunks of pure Sc metal (99.9% Sc) in the forming gas. Then the nitridation process took place in the ultra-high-purity nitrogen at 1100 ^{o}C and 500 Torr for ten hours. The ErN source was synthesized by nitridizing small chunk of pure Er metal (99.9%) at 1460 °C and 400 Torr. For ErN crystal growth, polycrystalline tungsten foil was used as the substrate and resulted in a polycrystalline ErN deposit. For ScN, a tungsten (100) oriented single crystal substrate (tungsten seed) was used as the substrate and produced ScN single crystal growth.

The tungsten seed was prepared by cutting a tungsten rod into slices that were then machined to a specific design to fit inside the tungsten crucible. The diameter of the seed side facing the ScN source was 8 mm, while the diameter of the other side was 9 mm. A tungsten lid with a 25 mm i.d. and 30 mm o.d. was designed to hold the seed. A circular cooling fin with 30 mm diameter was set on the outer side of the seed. This configuration selectively cooled the seed and provided a higher driving force for crystal growth, and consequently higher growth rate of ScN single crystal. Figure 2.3 shows the configuration of the crucible, seed, lid, and fin used in the experiments. The distance between the metal nitride source (ErN or ScN) and the growth area (the tungsten substrate) was kept constant at approximately 2.5 cm. The tungsten substrate (the foil or the seed) and the lid were weighed before and after the growth to calculate the growth rate.

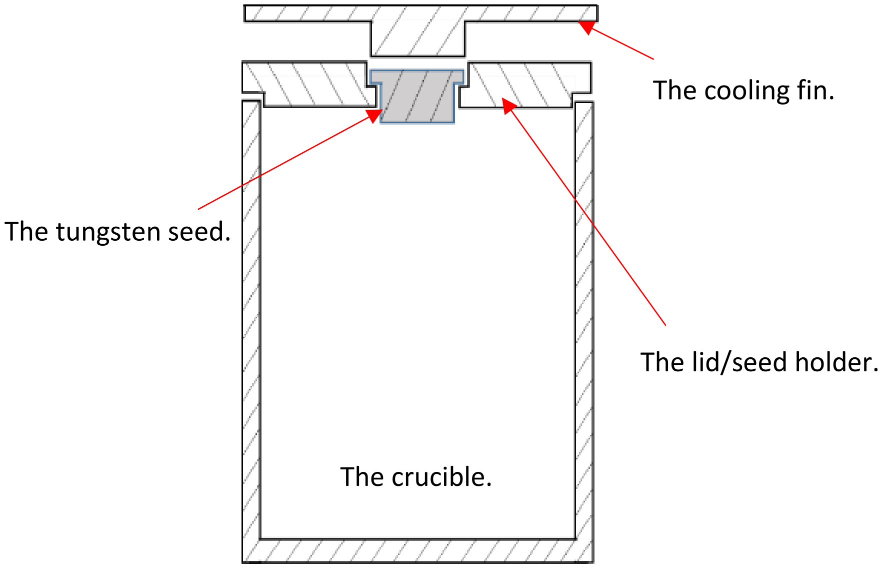

Figure 2.3*: The configuration of the modified PVT crucible.*

2.2 Polishing the Tungsten Seed

The tungsten seed requires a very smooth surface to produce large crystal grains. It was double side polished. The side of 9 mm diameter was roughly polished by 400 grit SiC sand paper just to remove some rust that remained after the tungsten rod was cut. On the crystal growth surface, nine stages of mechanical polishing using Techprep, Allied High

Tech, Inc. were performed to achieve an optical surface. The nine stages consisted of polishing with:

1. SiC sand paper 400 grit size and water. The polishing time varied from 15 to 30 minutes based on the roughness and shape of the surface since the cutting and machining process resulted in non-uniform surfaces among the different seed.
2. SiC sand paper 600 grit size and water for about 15 to 20 minutes, based on the result of step one.
3. Diamond slurry of 15 µm particle size with an Acetasilk cloth for 10 to 15 minutes depending on the result.
4. Diamond slurry of 9 µm particle size with Acetasilk cloth for 10 minutes.
5. Diamond slurry of 6 µm particle size with Synthetic Velvet cloth for 10 minutes.
6. Diamond slurry of 3 µm particle size with Synthetic Velvet cloth for 10 minutes.
7. Diamond slurry of 1 µm particle size with Synthetic Velvet cloth for 10 minutes.
8. Diamond slurry of 0.25 µm particle size with MultiTex cloth for 10 minutes.
9. Diamond slurry of 0.05 µm particle size with MultiTex cloth for 10 minutes.

Each polishing cloth in the steps 3 to 9 gives different surface roughness. The Acetasilk cloth is suitable for rough to intermediate polishing, while the Synthetic Velvet cloth is better for intermediate to final polishing. The MultiTex cloth used in the last two steps is a superior fine polishing cloth capable of producing an optical quality finish. In each step, a new polishing cloth was used, and the seed was washed by distilled water to remove any residual slurry from the previous step. During the polishing process, any dust contamination must be avoided because it causes scratches to the seed surface which consequently requires to repeat some polishing steps depending on the scratch size. The final polishing step was followed by sequentially cleaning in distilled water, acetone, methanol, and isopropanol in an ultrasonic cleaner.

2.3 The Vacuum System

The vacuum system consists of: two pumps, a mechanical pump and a diffusion pump; a rough valve; a foreline valve; and a high vacuum valve. The furnace chamber is equipped with three pressure gauges including two thermocouple pressure sensors with different pressure ranges, 0-1000 Torr and 0-1 Torr, and an ion gauge ($0\text{-}10^{-4}$ Torr). The chamber was evacuated in two stages to remove all oxygen. In the first stage (rough vacuum mode), only the mechanical pump was used, to reach a pressure of about $4\text{x}10^{-2}$ Torr. Then, in the second stage (high vacuum mode) both the mechanical and diffusion pumps were run to reach a pressure of about $3\text{x}10^{-6}$ Torr at 22 ^{o}C. To obtain the base pressure ($3\text{x}10^{-6}$ Torr), the chamber was left under high vacuum mode for 24 hours.

2.4 The Operating Temperatures and Pressures

The temperature and pressure conditions for sublimation were 1620-1770 ^{o}C and 150-510 Torr for ErN, and 1850–2000 ^{o}C and pressure of 15-35 Torr for ScN. Ultra-high-purity nitrogen gas continuously flowed through the system during growth. During start-up, the furnace was heated at a rate of 400 ^{o}C/hr up to the final growth temperature. The ErN and ScN crystals were grown by maintaining that dwell temperature. The growth time varied from 15 to 100 hours for ErN, and from 100 to 350 hours for ScN.

2.5 Characterization Methods

The ErN and ScN crystals were characterized quantitatively and qualitatively by several methods including structure determination, vibrational properties, surface roughness, chemical composition, and the surface morphology.

2.5.1 Crystal Structure, Orientation, and Quality: X-ray Diffraction

X-rays are high-energy electromagnetic radiations with a wavelength between 10^{-3} to 10^{1} nm [4]. X-ray diffraction for crystal analysis was started by Laue, Friedrich, and Knipping in 1912. Since then, the method has been thoroughly developed so now it is a very powerful characterization technique in materials science and engineering. It’s a nondestructive tool, and can reveal various information on the materials such as crystal structure, phases present, phase transitions, crystalline quality, orientation, and internal stress. Wavelengths below 0.1-0.2 nm are called hard x-rays, while longer wavelength are called soft x-ray. In the materials science, hard x-rays are most often used because they can penetrate deeply in all substances [5].

Figure 2.4 shows the difference between θ-2θ scan and Omega (ω) scan. In θ-2θ scan (see Figure 2.4a), both the sample holder and the x-ray detector rotate, and it gives x-ray intensity as a function of 2θ. This scan is used to determine the crystal structure and orientation and lattice constant.

The crystal quality can be determined by Omega (ω) scan or rocking curve. The rocking curve is obtained by changing ω angle and fixing 2θ as shown in Figure 2.4b. It gives a plot of ω vs. x-ray intensity. Rocking curve is used to study the crystal imperfection such as dislocation, curvature, misorientation, mosaic spread. Crystal defects create disruptions in the perfect parallelism of atomic plane, thus rocking curve broadens. The Full Width at Half Maximum (FWHM) of the rocking curve is usually calculated as an indication of the crystal quality where the lower FWHM, the better crystal is.

In this work, the orientation and lattice constants of the ErN and ScN crystals were determined by θ-2θ x-ray diffraction. The patterns were taken with a Miniflex Rigaku diffractometer using a copper Kα source with a wavelength of 1.54 Å. To confirm the epitaxial growth of ScN, XRD ϕ scans were taken via Rigaku Smartlab diffractometer. The 45° angle rotation relationship between the ScN film and W seed was confirmed with a Bruker D8 Discover diffractometer. The structural quality ScN layer was determined by ω scan in which the Full Width at Half Maximum (FWHM) was calculated.

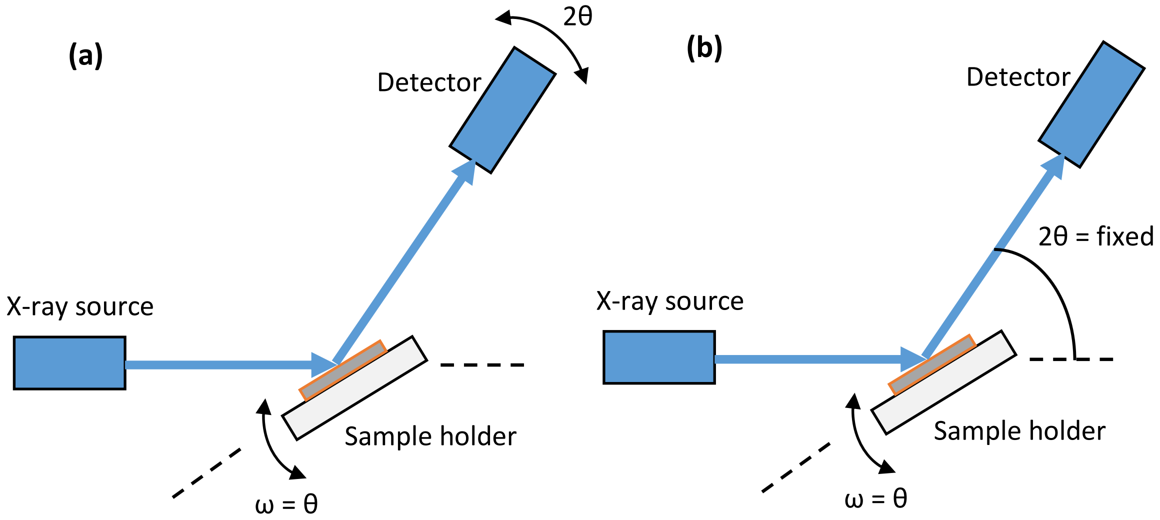

Figure 2.4: *The measurements of: (a) θ-2θ x-ray diffraction scan. (b) Omega (ω) scan or rocking curve.*

2.5.2 Vibrational Spectroscopy: Raman Spectroscopy

Molecules and crystals can be described as systems of balls (atoms) connected by springs (chemical bonds). These systems can vibrate with frequencies determined by the mass of the balls (atomic weights) and by the stiffness of the springs (bond force constants).

Raman spectroscopy is sensitive to the details of atomic arrangement and chemical bonding, thus making it a good structural characterization tool. The spectrum is more sensitive to the strengths, lengths, and arrangement of bonds in a material than the chemical composition, so in crystals it responds more to details of defects and disorder than to impurities [6].

In this study, the vibrational properties of ErN crystals were determined by Raman spectroscopy.

2.5.3 Surface Roughness Measurement: Atomic Force Microscope (AFM)

Atomic force microscopy (AFM), also called scanning force microscopy (SFM), is utilized to measure surface topography and roughness. It measures the force between a sample surface and a very sharp probe tip mounted on a cantilever beam which has a spring constant of about 0.1—1.0 N/m, which is lower than the typical spring constant between two atoms by more than an order of magnitude. The raster scanning motion is controlled by piezoelectric tubes. To obtain the surface topography, the force is determined as a function of the sample's position [7]. Detection is most made optically by interferometry or beam deflection. In the AFM measurement, the tip is held in contact with the sample. The resolution is a few nanometers for scans up to 130 µm, and can be at the atomic scale for smaller ranges. This measurement can be utilized for both conducting and insulating materials without sample preparation [6].

The effect of the growth temperature on the surface topography and roughness of the ScN crystal and the step heights were investigated by atomic force microscopy (AFM) using an Innova AFM system in contact mode with MSCT cantilevers.

2.5.4 Electron Emission Spectroscopies: X-Ray Photoelectron Spectroscopy (XPS)

X-Ray photoelectron spectroscopy (also known as electron spectroscopy for chemical analysis, ESCA) provides atomic or chemical state identification, or both. The x-rays involved in XPS are soft (usually 1486 eV from an Al anode) ejecting photoelectrons from the sample surface. It measures the energy distribution of electrons ejected from a material due to absorbing the incident x-rays by core electrons. XPS is a nondestructive surface sensitive technique in which electronic energy level excitations are involved. It's sensitive to less than monolayer amounts of material, and the probing depths is not greater than about 50 Å without using sputter profiling.

The electrons photo emitted from the core levels are used to identify the elements of the sample from their binding energies. Additional chemical state information can provided by the chemical shifts in the binding energies. The compositions of the different elements can be determined from relative peak intensities. All elements can be identified by XPS except hydrogen and helium. It is a very powerful tool due to good quantification, excellent chemical state determination capabilities, applicability to a wide variety of materials from biological materials to metals, and its generally nondestructive nature.

The depth of the measured solid material range from the top 2 atomic layers to 20 layers. The examined area can be as large as 1 cm x 1 cm or as small as 70 µm x 70 µm.

XPS has become the most broadly applicable surface analysis technique due to its capability of quantitative and chemical state analysis combined with the surface sensitivity [6].

In this work, XPS technique was used to find the surface composition of the grown crystals.

2.5.5 Imaging Techniques (Microscopy)

Two imaging techniques, optical light microscopy and scanning electron microscopy (SEM) were employed in this work to evaluate the morphology of the deposited ScN and ErN crystals and to measure the feature sizes.

2.5.5.1 Light Microscopy

The objective of the light microscope is to provide a magnified image of a specimen. Since the human eye uses visible wavelength light, the light microscope is the only technique which can do this directly. Reflected or transmitted light from the specimen passes through a magnification column. The light microscope can provide the topological contrast by shadowing in reflection.

A Nikon Eclipse LV100 optical microscope was utilized in this work to image and determine the surface morphologies of the produced crystals.

2.5.5.2 Scanning Electron Microscopy (SEM)

The main advantage of SEM over the light microscope is the image resolution. The magnification range of the SEM is typically in the range of 10-500,000 times [4], and the resolution can approach a few nanometers [6]. In the light microscope, topological contrast can be provided by shadowing in reflection, while in SEM the measured signal intensity varies across the imaged sample due to variations in the local microstructure, orientation, and shape. Consequently, it alters the mechanisms of the formation and collection of the signal [4]. In addition to the surface imaging, the chemical composition of materials and the distribution can be obtained by carrying out the chemical imaging in SEM.

The compositional analysis can be performed by energy dispersive spectroscopy (EDS). The incoming electron beam interacts with the specimen to produce detectable signals (visible light and x-rays for example) as a result of the ionization of an atom by high-energy radiation where an inner shell electron is removed. To return the ionized atom to the ground state, an electron from a higher energy outer shell fills the vacancy in the inner shell and releases an energy equal to the potential energy difference between the two shells. This energy is specific to the elements present. This technique is capable of detecting x-rays from all the elements in the periodic table [6].

EDS and high magnification images of the ErN and ScN crystals were taken with FEI Versa 3D Dual Beam Field Emission Scanning Electron Microscope (SEM) to determine the crystal surface morphology and image and measure defects such as steps and cracks.

2.6 The Process Simulation

The process simulation was performed with FLUENT, a CFD package from ANSYS Inc. to investigate the behavior of the new crucible design with the cooling fin, and the results were verified experimentally.

Computational fluid dynamics (CFD) technique is one of the most advanced computational technologies evolved from academic research into widespread industrial application [8]. It has been widely used to predict the thermal performance of heating processes to ensure thermal uniformity in the crystal growth systems. The thermal modeling employed to simulate the crystal growth systems has been proven to be within an error of 2.5% of the experimentally measured temperature distributions in laboratories and industries [9].

A conventional crucible and a modified crucible with a cooling fin (extended surface) were simulated to investigate the effect of the fin on the local ScN growth rate on the seed.

The growth temperature and temperature distribution in the growth chamber can significantly affect the local growth rate along the growth interface [10]. Knowing these parameters can help to control on the local temperature distribution inside the crucible where the crystal growth occurs. Since the PVT process takes place in a black box [11, 12], and is difficult to be monitored, the simulated temperature field provides qualitative and quantitative information on the growth history as a function of the process parameters and geometry. The global heat transfer phenomena fundamentally comprise conduction, convection, radiation, induction heating, and the heat of sublimation and crystallization at the source-vapor interface and crystal vapor-vapor [13].

The simulation results are shown and demonstrated in chapter five.

References

[1] B. Liu, J. Edgar, Z. Gu, D. Zhuang, B. Raghothamachar, M. Dudley, A. Sarua, M. Kuball, H. Meyer III, The durability of various crucible materials for aluminum nitride crystal growth by sublimation, Materials Research Society Internet Journal of Nitride Semiconductor Research. 9 (2004).

[2] L. Du, J. Edgar, E.A. Kenik, H.M. Meyer III, Sublimation Growth of Titanium Nitride Crystals, J. Mater. Sci. : Mater. Electron. 21 (2009) 78.

[3] L. Du, J. Edgar, R.A. Peascoe-Meisner, Y. Gong, S. Bakalova, M. Kuball, Sublimation crystal growth of yttrium nitride, J. Cryst. Growth. 312 (2010) 2896-2903.

[4] G. Hübschen, I. Altpeter, R. Tschuncky, H. Herrmann, Materials characterization using Nondestructive Evaluation (NDE) methods, Woodhead Publishing, 2016.

[5] M. Lee, X-Ray Diffraction for Materials Research: From Fundamentals to Applications, CRC Press, 2016.

[6] C.R. Brundle, C.A. Evans, S. Wilson, Encyclopedia of materials characterization: surfaces, interfaces, thin films, Gulf Professional Publishing, 1992.

[7] S. Gaspar, K. Hickman, J. McNeil, R. Jacobson, G. Lindauer, Y. Strausser, E. Krosche, Metal Surface Morphology Characterization Using Laser Scatterometry, MRS Online Proceedings Library Archive. 181 (1990).

[8] A.I. Zhmakin, Modelling of Heat Transfer in Single Crystal Growth, arXiv preprint arXiv:1410.1674 (2014).

[9] D.R. Hemenway, , Computational modeling of cadmium sulfide deposition in the CdS/CdTe solar cell manufacturing process (2013).

[10] R. Ma, H. Zhang, V. Prasad, M. Dudley, Growth kinetics and thermal stress in the sublimation growth of silicon carbide, Crystal growth & design. 2 (2002) 213-220.

[11] S. Nishizawa, H. Yamaguchi, T. Kato, M.N. Khan, K. Arai, N. Oyanagi, Y. Kitou, W. Bahng, New crucible design for SiC single crystal growth by sublimation, MRS Online Proceedings Library Archive. 640 (2000).

[12] S.I. Nishizawa, T. Kato, Y. Kitou, N. Oyanagi, F. Hirose, H. Yamaguchi, W. Bahng, K. Arai, High-quality SiC bulk single crystal growth based on simulation and experiment. 457 (2004) 29-34.

[13] S.G. Müller, R. Eckstein, J. Fricke, D. Hofmann, R. Hofmann, R. Horn, H. Mehling, O. Nilsson, Experimental and theoretical analysis of the high temperature thermal conductivity of monocrystalline SiC. 264 (1998) 623-626.

Chapter 3: Sublimation Growth and Characterization of Erbium Nitride Crystals

. As published in Crystal Growth & Design journal, 2018, 18, 3762-3766.

ACS Publication.

Sublimation Growth and Characterization of Erbium Nitride Crystals

Hayder A. Al-Atabi[a,c], *Zahraa F. Al-Auda*[a,c], *B. Padavala*[a], *M. Craig*[b], *K. Hohn*[a], *and James H. Edgar*[a*]

(a) Department of Chemical Engineering, Kansas State University, Manhattan, KS 66506, United States

(b) Department of Geology, The University of Kansas, Lawrence, KS 66045, United States

(c) Department of Chemical Engineering, The University of Technology, Baghdad, Iraq

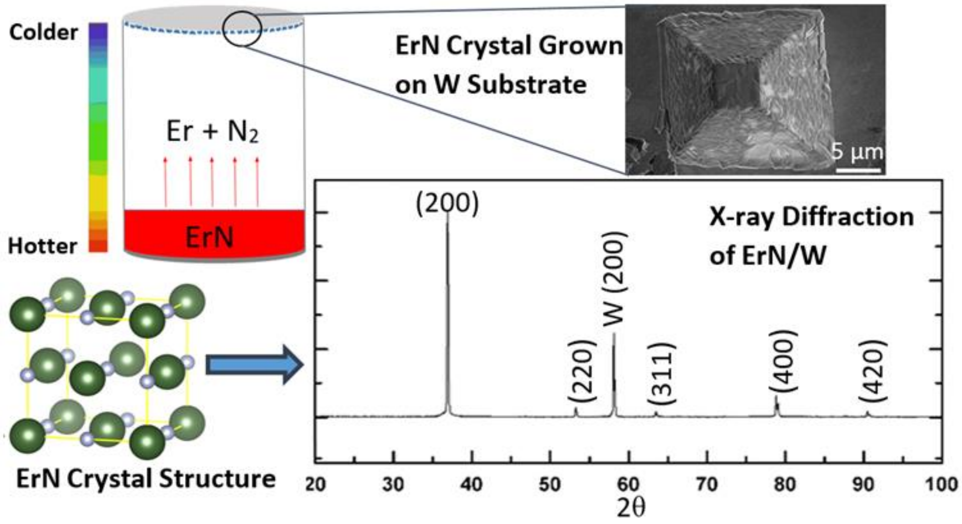

Graphical abstract of ErN crystal growth.

---

[*] Corresponding author.

E-mail address: edgarjh@ksu.edu (J. H. Edgar)

3.1 Abstract

Erbium nitride (ErN) is a rare earth nitride notable for its magnetic and optical properties. Here we report on its growth on a non-native substrate, tungsten foil, via physical vapor transport, and its characterization. The source material was erbium metal that was converted to ErN by heating in nitrogen. Subsequently, it was sublimed to form the ErN crystals. The operating conditions were 1620-1770 ^{o}C and 150-330 Torr in pure nitrogen. The growth rate increased exponentially with temperature with an activation energy of 508 kJ/mol, and inversely with pressure. X-ray diffraction revealed the ErN preferentially adopted a (100) orientation, the same as the dominant orientation of the tungsten sheet. The lattice constant was 4.853 Å. The crystal shapes and sizes were dependent on the temperature, as revealed by SEM and optical microscopy. The ErN crystals were highly faceted, bound by (100) and (111) crystal planes. The ErN compound deviated from stoichiometry: the Er:N atomic ratio ranged from 1:1.15 to 1:1.2 according to EDX and XPS elemental analysis. Raman spectra was in good agreement with theoretical predictions.

Keywords: *Crystal Growth, Sublimation Growth, Erbium Nitride*

3.2 Introduction

The rare-earth elements (REs), having atomic numbers from 57 (La) to 71 (Lu), are characterized by the filling of 4*f* electron orbitals. They represent the solely stable elements with more than marginally filled *f*-shell electronic orbitals; consequently, they hold the largest spin and orbital moments.[1] Due to their ionic charge of 3+, they can combine with other elements to result in rare-earth monopnictides, REX (X=N, P, As, Sb, Bi).[1, 2] The heavier pnictides were reported to be antiferromagnetic, while the nitrides are almost all ferromagnetic.[3-5]

The rare-earth nitrides (RENs) have a wide range of properties. They form the rock salt structure with lattice constants ranging from 4.76 Å for LuN to 5.305 Å for LaN.[1] The magnetic properties of RENs are especially of interest due to their unfilled and highly localized 4*f* orbitals[6] making them interesting candidate for spintronic devices.[7] The electron transport properties and band structures have only recently been determined;[1] they vary from metallic or semimetallic to semiconducting.[4] The uncertainty of their charge transport properties is attributed to two issues that strongly affect their stoichiometry: a tendency to expeditiously oxidize when exposed to air, and to form nitrogen vacancies (V_N).[1] RENs can potentially be combined with group-III nitrides to develop new functional devices. RENs with narrow band gaps, of approximately 1 eV optical absorption and absolute gaps with the order of one half of the optical absorption, have promising properties for IR detectors. Consequently, the heterojunction of the wide band-gap group-III nitrides and RENs could result in interesting properties for multi-wave length photonic devices.[8, 9]

ErN has not been extensively studied. There have been more theoretical than experimental studies of RENs. Aerts *et al.*[10] predicted half-metallic (PrN-GdN), insulating

(TbN- HoN) and semimetallic (ErN-YbN) behaviors might arise in the REN series. According to Larson *et al.,*[6] the LSDA+U approach predicts that when only the U_f parameter is involved, the RENs have a small band overlap, thus they are semimetals.

In prior studies, REN thin films were grown by UHV-based methods such as pulsed-laser deposition (PLD),[11, 12] dc/rf magnetron sputtering,[13-15] and molecular beam epitaxy (MBE).[9, 16, 17] The lack of native substrates has been a major difficulty that has impeded the RENs epitaxial growth. Furthermore, the tendency of RE to react with silicon (in general the most common substrate for all epitaxial and polycrystalline thin film studies) makes it an unsuitable substrate. Because the RENs adopt a rock salt (NaCl) crystal structure, (100) oriented crystals have been the substrate of choice by most researchers. MgO (100) was employed in the epitaxial growth of both CeN by Lee *et al*.[18] and GdN by Gerlach *et al*.[19] However, the lattice constant mismatch is quite large, +19.2 % and +18.7 % for CeN and GdN respectively, which results in large strains and high defect concentrations, adversely affecting the properties of the films.

Brown and Clark[20] studied the effect of N % composition and reported that the lattice constant decreased as the percent nitrogen content increased, from 4.848 Å to 4.843 Å for 92 at% N to 98 at% N, respectively. Table 3.1 summaries some known ErN properties.

Granville *et al.*[24] studied the vibration properties of ErN and reported one Raman shift peak at 550 cm^{-1}. In their study, a thin film of ErN was grown by evaporating Er in the presence of 10^{-4} mbar of ultra-high pure nitrogen, and depositing on an ambient temperature substrate.

Table 3.1: *Properties of ErN crystals.*

Crystal structure	Rock Salt
Lattice Constant (Å)	4.842[21]
Energy bandgap (eV)	1.2, 1.3, 2.4[4, 22]
4*f* shell Optical Transition wavelength (μm)	1.54[23]

A key erbium property of interest is the optical transition of its electrons in the 4*f* orbital. This produces light at 1.54 μm, which corresponds to the absorption minimum in silica optical fiber.[23] Hence a goal of many studies involving erbium has been to induce this transition electronically, by for example, incorporating erbium into a semiconductor such as silicon or gallium nitride. This may also be possible in a novel, erbium nitride semiconductor, if it can be made with a high crystal quality and low residual impurity concentrations. In this case, the number of erbium atoms per volume would be much higher, since it is a major component of the binary semiconductor rather than just a dopant.[23]

The goal of this study was to demonstrate ErN crystal growth by the sublimation-recondensation method and to characterize the crystal properties. This method produces crystals at a much higher temperature (>1600 °C) than epitaxial growth techniques (<1100 °C), enabling much better crystal quality since it operates closer to thermal equilibrium, has higher adatom diffusivities and because diatomic nitrogen is more reactive. This study examined the impact of process parameters on the crystal growth rates and the properties of the resulting crystals.

3.3 Experimental Work

The sublimation growth was conducted in a tungsten furnace that was previously described.[25] The erbium nitride crystals were grown unseeded on polycrystalline tungsten foils with a predominately (100) textures. These foils were cleaned by the acetone, methanol, and iso-propyl alcohol respectively. Tungsten had previously proved to be a good, unreactive substrate for the sublimation of TiN[26] and AlN.[27] The distance between ErN source and the growth area was kept constant at approximately 2 cm.

The sublimation was carried out over the temperature range of 1620 –1770 ^{o}C and in ultra-high-purity nitrogen at pressures of 150–510 Torr. During start-up, the temperature of the furnace was increased at a rate of 240 ^{o}C/hr up to the growth temperature. The ErN crystals were grown by maintaining that dwell temperature for 20 hr. Overall, each experiment needed 30 to 36 hr to complete, depending on the growth temperature.

The ErN source was synthesized by heating small chunks of Er metal (99.9 % purity) in pure nitrogen at 1500 ^{o}C. The starting pressure at room temperature was 400 Torr, and it increased gradually to 427 Torr at the nitridizing temperature. After stopping the experiment, the pressure was 350 Torr which means 50 Torr of N_2 was consumed. The resulting ErN source was blue-grey and brittle.

The morphology and size of the resulting deposits were characterized by optical and scanning electron microscopy. X-ray diffraction patterns were taken to determine the structure, lattice constant, and orientation of the crystals. A copper Kα x-ray source was employed with a wavelength of 0.15418 nm. Raman spectra was employed to characterize the ErN's vibrational properties. The elemental analysis was estimated via X-ray Photoelectron Spectroscopy (XPS) and Energy Dispersive x-ray Spectroscopy (EDS).

3.4 Results and Discussion

The following reversible reaction takes place in the tungsten furnace:

$$ErN_{(s)} \leftrightarrow Er_{(g)} + \frac{1}{2} N_{2(g)} \tag{1}$$

The solid ErN sublimes dissociatively at the hotter point in the crucible (at the ErN source) via the forward reaction and condensates at the colder tungsten foil via the reverse reaction.

Figure 3.1 shows the effect of growth temperature on the crystal growth rate. The growth rate increased exponentially with increasing temperature. This trend is attributed to increasing the sublimation rate, thus the tungsten substrate was saturated with Er-N_2 gases.

The reaction of sublimation-recondensation was assumed to be zero order, thus the activation energy was estimated as 508 kJ/mol via Arrhenius equation (2):

$$\text{Rate} = A\, exp(-E/RT) \qquad (2)$$

Where, A is the frequency factor, E is the activation energy, R is the universal gas constant (8.314 kJ/(mol·K)), and T is the growth temperature (K).

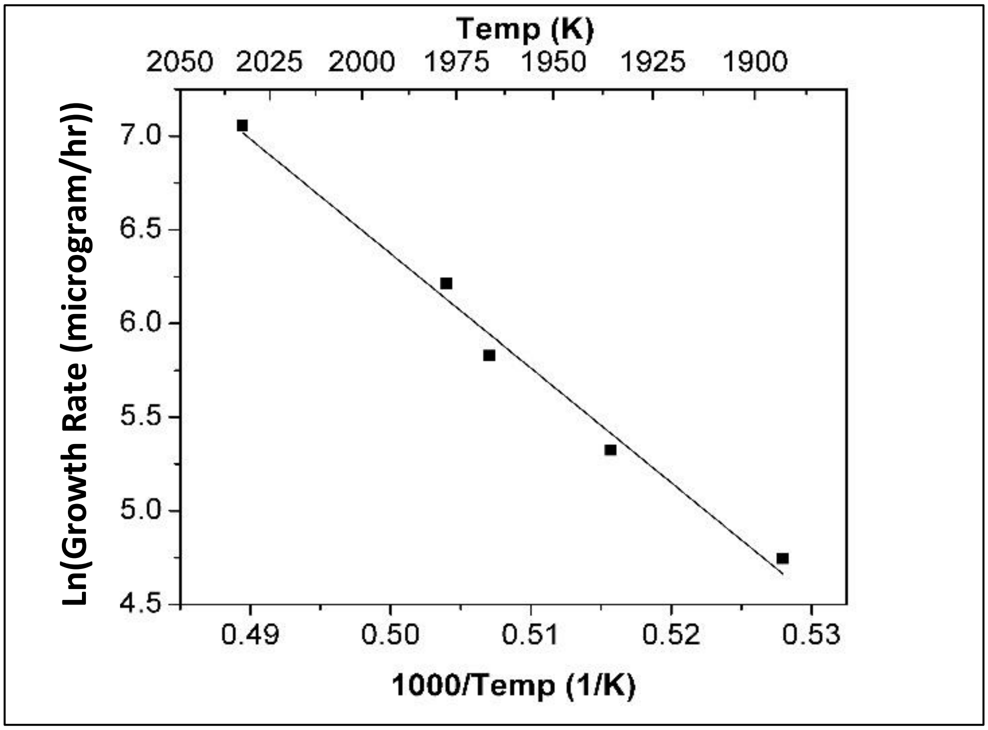

Figure 3.1: *The effect of temperature on the growth rate. Pressure = 150 Torr.*

Comparing to our previous studies, the activation energy of ErN (508 kJ/mol) is lower than that of AlN (681 kJ/mol)[28] and close to that of YN (467 kJ/mol)[29] and ScN (456 kJ/mol).[25]

Since sublimation has an inverse relationship to pressure, the growth rate was inversely proportional to pressure (Figure 3.2).

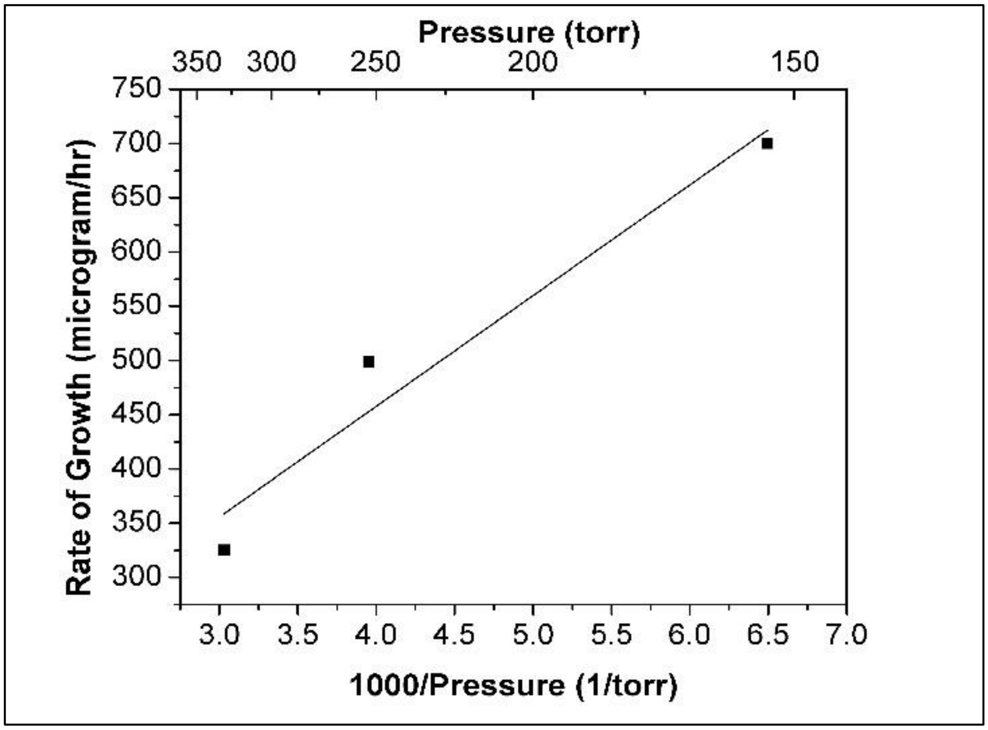

Figure 3.2*: The effect of pressure on the growth rate. Growth temperature= 1750 °C.*

The SEM images elucidate how the crystal morphology was influenced by the growth temperature. Figures 3.3-3.5 show the SEM images for crystals grown at 1620, 1700, and 1770 °C and 250 Torr. Grain boundaries defects appeared at 1620 °C; the facets of the crystals were rough. Clearly, specific crystal planes could be discerned, but their surfaces were rough, possibly due to low adatom mobility. However, at higher temperatures (>1620 °C), the crystal facets became smooth, suggesting higher surface adatom diffusion rates. In other words, the ErN source generated Er vapor in large amount at a far greater growth rate than the speed of enlargements of defects in the substrate. Consequently, smooth crystals were grown. Two facets are predominant, the (111) and (100) plane, in Figure 3.4. The (111) facet has the highest growth rate, while (100) facet has the lowest growth rate. Facets with higher growth rate usually inclined to the ones having lower growth rate during the growth process. Figure 3.5 demonstrates the evolution of the (111) planes to the ones with lower growth rate like (311). However the (100) facet still has the lowest growth rate, remains unchangeable, and increases in size.

Figure 3.6 shows how the ErN crystals nucleate preferentially at tungsten substrate grain boundaries. Defects, such as screw dislocations, are known to reduce or completely eliminate the activation energy barrier to nucleation. Furthermore, the crystal size was significantly affected by temperature.

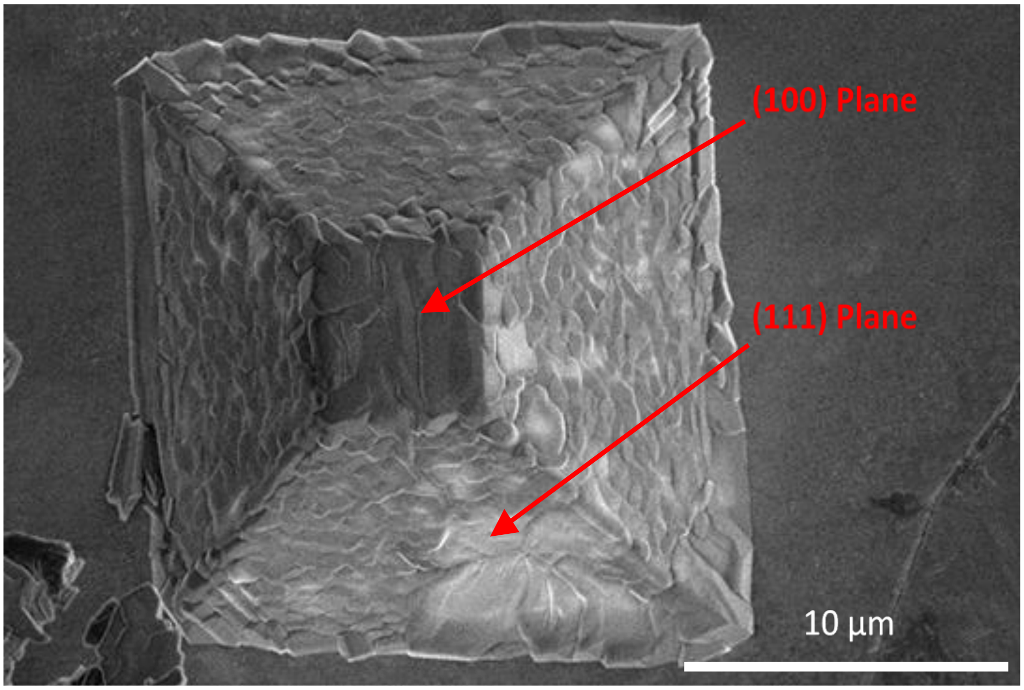

Figure 3.3*: SEM image of ErN crystals grown at 1620 ^{o}C and 250 Torr for 20 hours.*

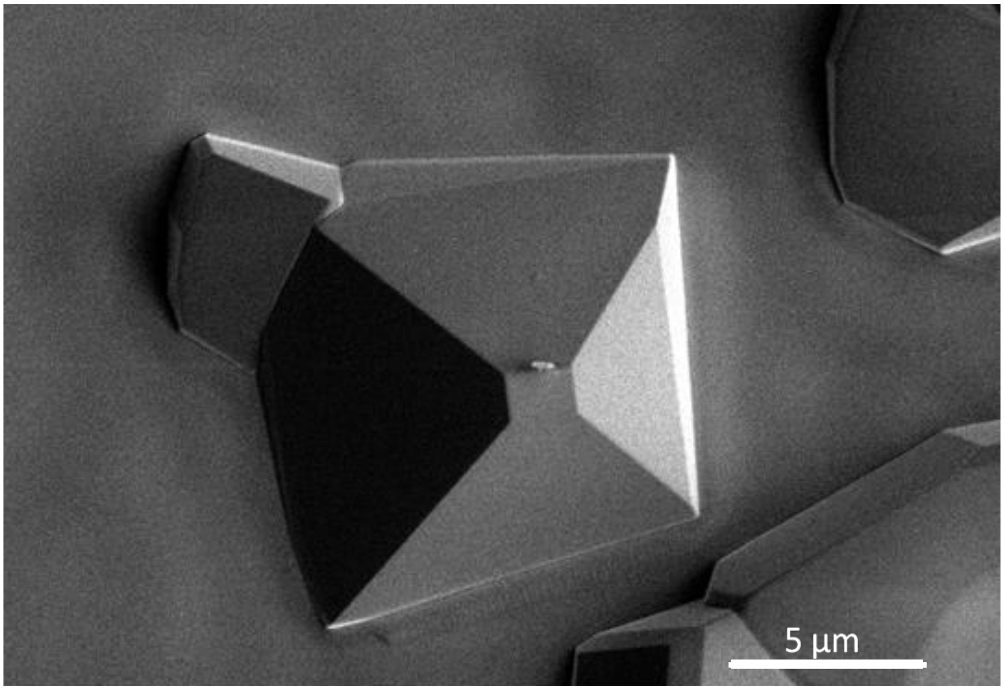

Figure 3.4*: SEM image of ErN crystals grown at 1700 ºC and 250 Torr for 20 hours.*

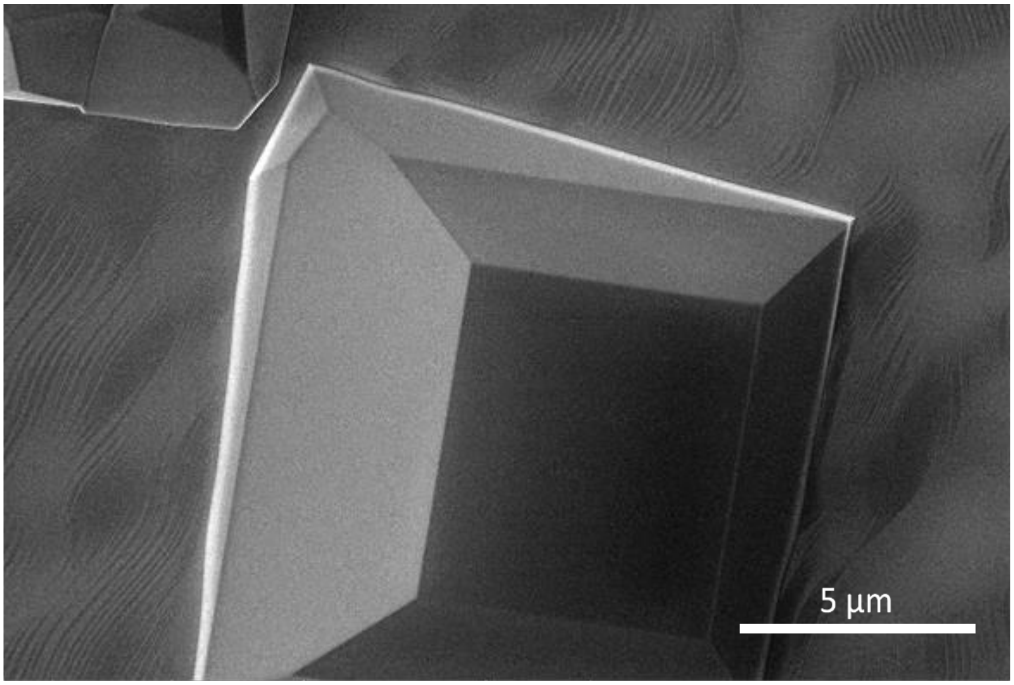

Figure 3.5*: SEM image of ErN crystals grown at 1770 ºC and 250 Torr for 20 hours.*

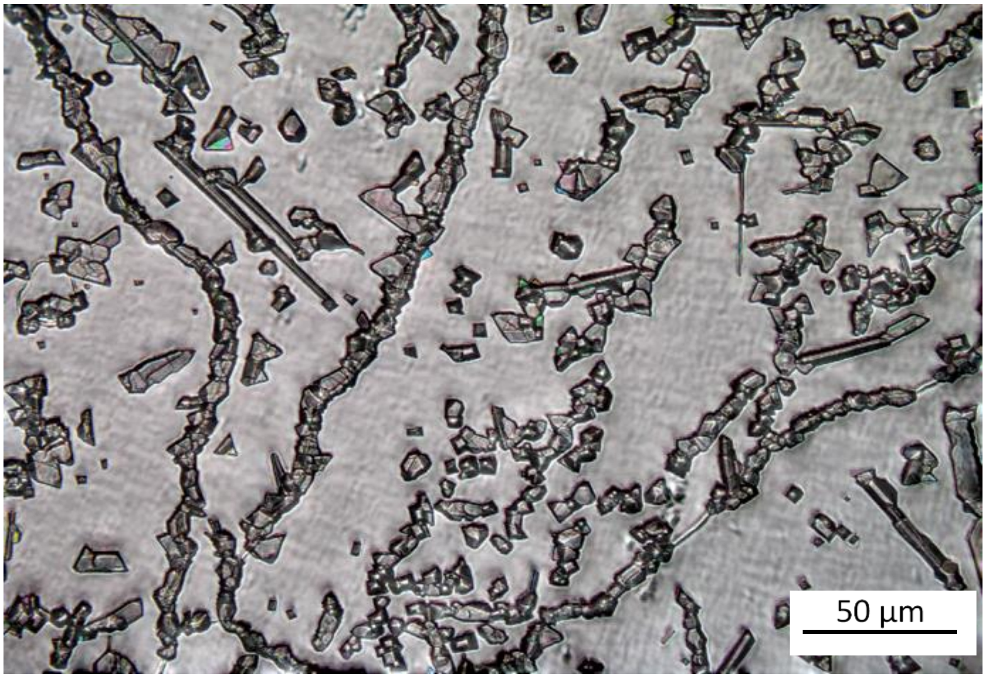

Figure 3.6*: ErN crystals preferentially position the grain boundaries of the tungsten substrate.*

ErN degrades upon air exposure. To test whether this is due to water vapor or oxygen, two samples of ErN crystals were investigated. The first sample was exposed to ambient air which contains water vapor; micrograph images were taken every 30 minutes. The crystals almost all converted to Er_2O_3 after 11 hours. The second ErN crystal sample was successfully stored in a desiccator under atmospheric pressure air surrounding with silica gel pellets for more than a month, and it was still stable. This means ErN is mostly sensitive to moisture which reacts with ErN to form Er_2O_3.

The structures and crystal orientations of tungsten foil (substrate), ErN source, and ErN crystals grown on the tungsten foil were characterized by XRD as shown in Figure 3.7. The tungsten foil was mainly dominated by the (200) orientation. The XRD pattern of the

ErN source included (111), (200), (220), (311), (222), and (400) reflections. ErN crystals grown on the tungsten foil were polycrystalline, but textured and exhibited fewer peaks: the (200), (220), (311), and (400) diffraction peaks. The (200) and (400) orientations of the ErN were more intense than is present in a randomly oriented powder. Thus ErN tends to adopt the (100) orientation because the tungsten substrate is also primarily (100) oriented. The average lattice constant calculated from the XRD pattern of grown ErN crystals was 4.853 Å which matches the reported value 4.842 Å[21] taking into account the higher nitrogen content in the grown ErN crystals.

XPS detected the electrons of 4d region for erbium metal (Er4d) and 1s region for nitrogen (N1s). The Er4d region exhibits complex multiple peaks. The energy dispersive x-ray spectroscopy (EDS) was also employed to characterize ErN crystals. The surface elemental analysis calculated via XPS and the bulk elemental analysis via EDS revealed that the ErN crystals were nitrogen-rich. The stoichiometry (Er:N) was 1:1.2 and 1:1.1 according to XPS and EDS. This trend is attributed to the high partial pressure of nitrogen, so the nitrogen atoms occupied interstitial sites with sublattices. The oxygen contamination was 0.1 - 0.2 atomic %.

Raman spectra (Figure 3.8) showed diagnostic phonon modes that can be attributed to ErN. The transverse acoustic phonon mode activated at the Brillouin zone folded point L occurs at ca. 123 cm^{-1}, the longitudinal acoustic phonon at the L point occurs at ca. 258 cm^{-1}, The transverse optical phonon at the Brillouin zone center occurs at ca. 330 cm^{-1}, the longitudinal optical phonon at the L point occurs at ca. 574 cm^{-1}, and the second order phonon of this mode occurs at ca. 1184 cm^{-1}. The broad feature from 600 to 1000 cm^{-1} is a photoluminescence band. Table 3.2 is a comparison among our Raman shift results and the theoretical and experimental results of Granville *et al.* (2009)[24]. They are in good agreement.

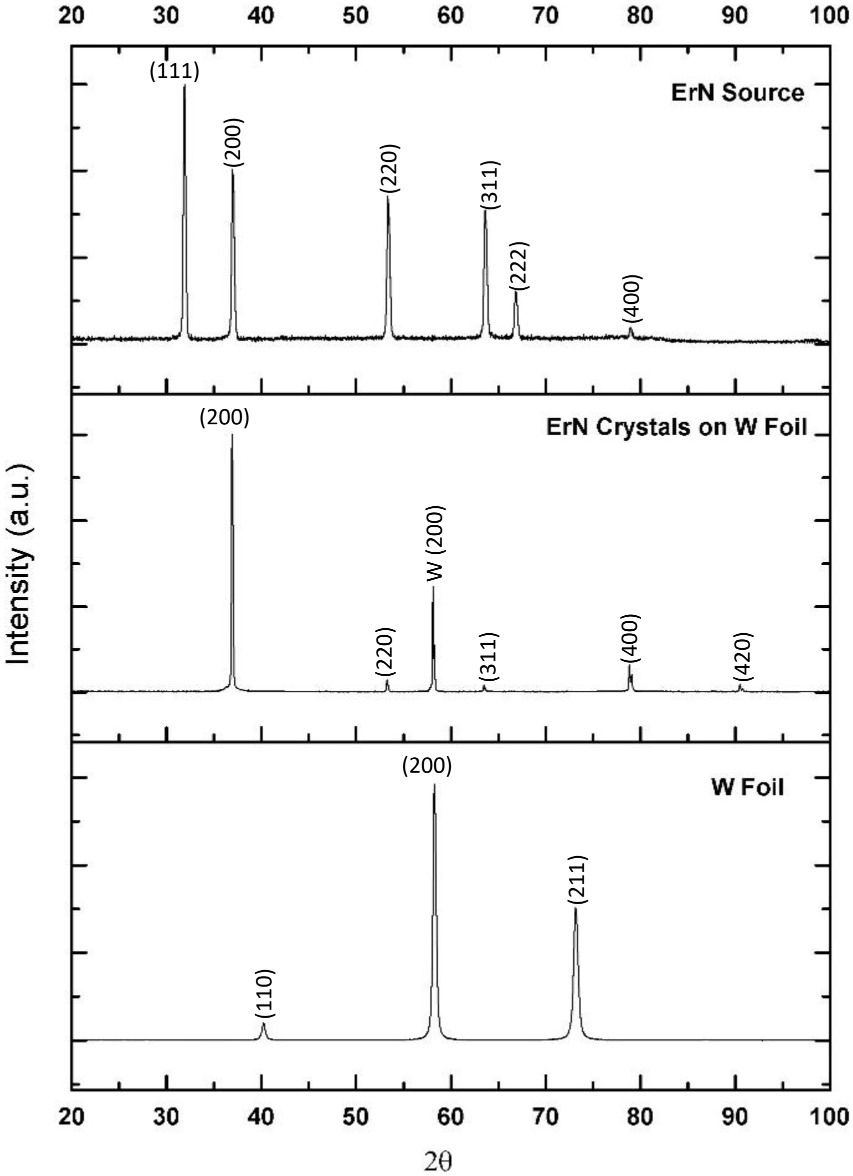

Figure 3.7*: XRD patterns of the tungsten substrate, ErN source, and ErN crystals grown at 1770 °C and 150 Torr.*

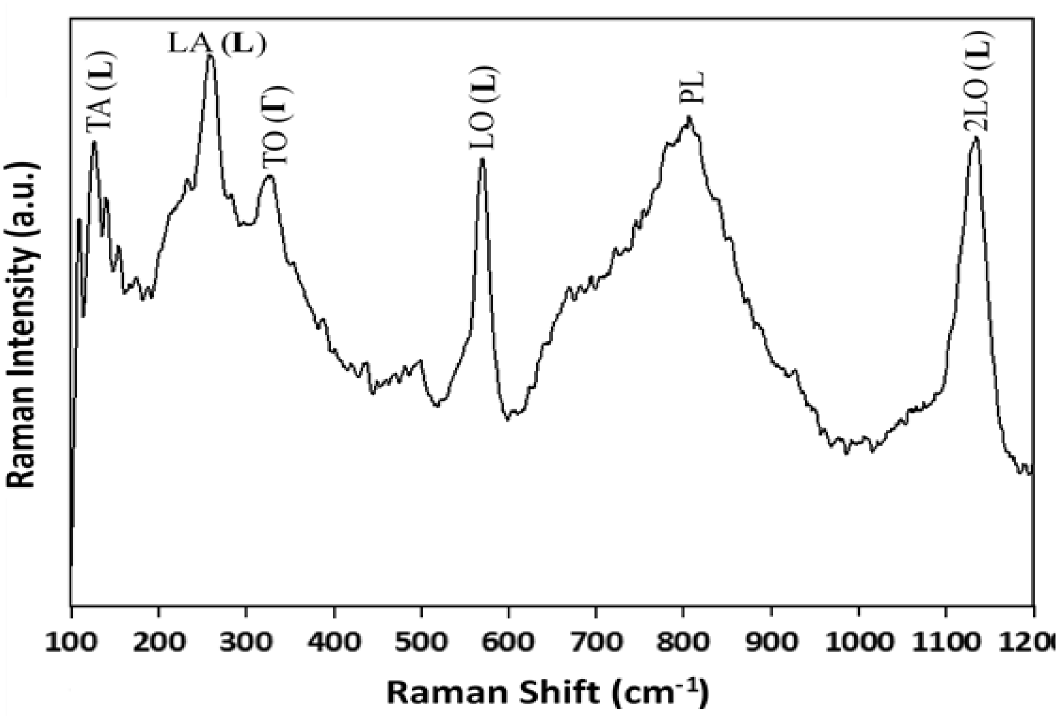

Figure 3.8: *Raman shift of ErN crystals grown at 1770 °C and 150 Torr.*

Table 3.2: *Comparison of Raman shifts of ErN crystals.*

Mode	Frozen Phonon Approach[24]	Exp.[24]	Our Exp.
TA (L)	122		123
TA(X)	147		
LA(X)	207		
LA(L)	243		258
TO(Γ)	340		330
TO(X)	373		
TO(L)	426		
LO(X)	517		
LO(L)	592	550	574
2LO (L)			1184

3.5 Conclusion and Future Work Recommendations

The growth temperature had a dramatic impact on the ErN crystal growth, both the rate and crystal morphology. The growth rate increased exponentially with increasing temperature. At 1620 ^{o}C, small crystals with rough surfaces were grown. As the temperature increased (>1620 ^{o}C), the crystal size increased, and the surface morphology changed from rough to smooth. On the other hand, the growth rate was inversely proportional to the growth pressure. The ErN crystals were sensitive to ambient air exposure, and they degraded to erbium oxide powder presumably from moisture in air. XRD pattern revealed that there was a strong preference for (200) orientation which is attributed to the dominant orientation of the tungsten substrate (200). XPS and EDX elemental analyses showed that the ErN crystals were nitrogen-rich. Raman shift spectra of ErN crystal were in a good agreement with the theoretical results of the Frozen Phonon Approach.

For future work, it's recommended grow bigger crystals, using single crystal substrates such as 4H-SiC or AlN as seed crystals, and to characterize other ErN properties such as its magnetism, electron transport properties, and thermal transport properties.

Acknowledgement

Support for this project from the National Science Foundation Division of Materials Research (award number 1508172) and Higher Committee for Education Development in Iraq is greatly appreciated.

References

1. Franck Natali, Ben J. Ruck, Natalie OV Plank, H. Joe Trodahl, Simon Granville, Claire Meyer and Walter RL Lambrecht, Progress in Materials Science 58, 1316 (2013).

2. Chun-Gang Duan, RF Sabirianov, Wai-Ning Mei, Peter A. Dowben, SS Jaswal and Evgeny Y. Tsymbal, Journal of Physics: Condensed Matter 19, 315220 (2007).

3. F. Hulliger, J Magn Magn Mater 8, 183 (1978).

4. F. Hulliger, Handbook on the physics and chemistry of rare earths 4, 153 (1979).

5. O. Vogt and K. Mattenberger, Handbook on the Physics and Chemistry of Rare Earths 17, 301 (1993).

6. P. Larson, Walter RL Lambrecht, Athanasios Chantis and Mark van Schilfgaarde, Physical Review B 75, 045114 (2007).

7. Premlata Pandit, Vipul Srivastava, M. Rajagopalan and Sankar P. Sanyal, Physica B: Condensed Matter 405, 2245 (2010).

8. F. Natali, NOV Plank, J. Galipaud, BJ Ruck, HJ Trodahl, F. Semond, S. Sorieul and L. Hirsch, J. Cryst. Growth 312, 3583 (2010).

9. TF Kent, J. Yang, L. Yang, MJ Mills and RC Myers, Appl. Phys. Lett. 100, 152111 (2012).

10. CM Aerts, Paul Strange, M. Horne, WM Temmerman, Zdzislawa Szotek and Axel Svane, Physical Review B 69, 045115 (2004).

11. BJ Ruck, HJ Trodahl, JH Richter, JC Cezar, F. Wilhelm, A. Rogalev, VN Antonov, Binh Do Le and Claire Meyer, Physical Review B 83, 174404 (2011).

12. Franck Natali, Bart Ludbrook, Jules Galipaud, Natalie Plank, Simon Granville, Andrew Preston, Bin Le Do, Jan Richter, Ian Farrell and Roger Reeves, physica status solidi (c) 9, 605 (2012).

13. RM Osgood III, JE Pearson, CH Sowers and SD Bader, J. Appl. Phys. 84, 940 (1998).

14. Hiroaki Yoshitomi, Shinya Kitayama, Takashi Kita, Osamu Wada, M. Fujisawa, Hitoshi Ohta and T. Sakurai, Physical Review B 83, 155202 (2011).

15. Reddithota Vidyasagar, Shinya Kitayama, Hiroaki Yoshitomi, Takashi Kita, Takahiro Sakurai and Hitoshi Ohta, The European Physical Journal B 86, 52 (2013).

16. F. Natali, NOV Plank, J. Galipaud, BJ Ruck, HJ Trodahl, F. Semond, S. Sorieul and L. Hirsch, J. Cryst. Growth 312, 3583 (2010).

17. Franck Natali, BJ Ruck, HJ Trodahl, S. Vezian, B. Damilano, Y. Cordier, F. Semond and Claire Meyer, Physical Review B 87, 035202 (2013).

18. T-Y Lee, D. Gall, C-S Shin, N. Hellgren, I. Petrov and JE Greene, J. Appl. Phys. 94, 921 (2003).

19. JW Gerlach, J. Mennig and B. Rauschenbach, Appl. Phys. Lett. 90, 061919 (2007).

20. RC Brown and NJ Clark, Journal of Inorganic and Nuclear Chemistry 36, 2507 (1974).

21. Giorgio L. Olcese, Journal of Physics F: Metal Physics 9, 569 (1979).

22. F. Bommeli, L. Degiorgi and P. Wachter, J Magn Magn Mater 140, 1159 (1995).

23. JM Zavada, SX Jin, N. Nepal, JY Lin, HX Jiang, P. Chow and B. Hertog, Appl. Phys. Lett. 84, 1061 (2004).

24. S. Granville, C. Meyer, ARH Preston, BM Ludbrook, BJ Ruck, HJ Trodahl, TR Paudel and WRL Lambrecht, Physical Review B 79, 054301 (2009).

25. Zheng Gu, JH Edgar, J. Pomeroy, M. Kuball and DW Coffey, J. Mater. Sci. : Mater. Electron. 15, 555 (2004).

26. Li Du, James H. Edgar, Edward A. Kenik and Harry Meyer, J. Mater. Sci. : Mater. Electron. 21, 78 (2010).

27. B. Liu, JH Edgar, Z. Gu, D. Zhuang, B. Raghothamachar, M. Dudley, A. Sarua, Martin Kuball and HM Meyer III, Materials Research Society Internet Journal of Nitride Semiconductor Research 9, (2004).

28. Lianghong Liu and James H. Edgar, J. Cryst. Growth 220, 243 (2000).

29. Li Du, JH Edgar, Roberta A. Peascoe-Meisner, Yinyan Gong, Silvia Bakalova and Martin Kuball, J. Cryst. Growth 312, 2896 (2010).

Chapter 4: Bulk (100) scandium nitride crystal growth by sublimation on tungsten single crystal seeds

- *As published in Applied Physics Letters journal, 113, 122106 (2018). AIP publication.*
- *It is also a part of the provisional invention titled "METHODS OF GROWING SINGLE CRYSTAL MATERIALS" KSURF Disclosures 2017-065 and 2018-023.*

Bulk (100) scandium nitride crystal growth by sublimation on tungsten single crystal seeds

Hayder A. Al-Atabi[a,b] , *Neelam Khan*[c], *Edil Nour*[c], *Joseph Mondoux*[c], *Yi Zhang.*[d],*and J. H. Edgar*[a*]

a: Department of Chemical Engineering, Kansas State University, Manhattan, KS 66506, United States

b: Chemical Engineering Department, The University of Technology, Baghdad, Iraq

c: School of Science and Technology, Georgia Gwinnett College, Lawrenceville, Georgia, 30043, United States

d: Nitride Solutions Inc., 3333 West Pawnee Street, Wichita, Kansas 67213, United States

4.1 Abstract

Scandium nitride single crystals (14–90 µm thick) were grown on tungsten (100) single crystal substrate by physical vapor transport in the temperature range of 1850-2000 °C and pressure of 15-35 Torr. Epitaxial growth was confirmed using in-plane ϕ scan and out-of-plane x-ray diffraction techniques which revealed that ScN exhibits cube-on-cube growth with a plane relationship ScN (001) || W (001) and normal direction ScN [100] || W [110]. Atomic force microscopy revealed the surface roughness decreased from 83 nm

---

[*] Corresponding author.

E-mail address: edgarjh@ksu.edu (J. H. Edgar)

to 18 nm as the growth temperature was increased. X-ray diffraction (XRD) rocking curves widths decreased indicating the crystal quality improved with increasing growth temperature. The lowest XRD FWHM was 821 arcsec, which is so far the lowest value reported for ScN. Scanning electron microscopy (SEM) exhibited the formation of macrosteps and cracks on the crystal surface with latter due to the mismatch of ScN's and tungsten's coefficients of thermal expansion .

4.2 Introduction

Recently, there has been a remarkable interest in the properties and applications of transition metal nitrides [1]. In particular, the crystal growth and characterization of the group IIIB transition metal nitride scandium nitride (ScN), a semiconductor, is of interest for both fundamental science and potential electronic device applications. It possesses excellent physical properties such as high hardness, mechanical strength, and outstanding electronic transport properties. The heat, free energy, and entropy of formation of ScN suggest its high thermal stability. Its melting point is ≥ 2600 ^{o}C [2]. It has the rock salt crystal structure with a lattice constant of 4.503 ±0.002 Å [2-7]. It has a direct bandgap of 2.0 eV and an indirect band gap of 0.9 eV [8] and typically has a high electron carrier concentration ($>10^{20}$ cm^{-3}) [4,9]. One of the most exciting aspects of ScN is that it can have either *n*-type or *p*-type conductivity (with magnesium doping) [10]. The electrical properties of ScN are sensitive to impurities [10]. The electrical resistivity of unintentionally doped ScN varies dramatically, with reported values of 25, 130, 308, and

461 µohm-cm by Samsonov *et al*. [11], Sclar [12], Gschneidner [13], and Dismukes *et al*. [3,4] respectively.

Scandium nitride has several potential device applications. Moram *et al.* [14] and Lupina *et al.* [15] used ScN as a buffer layer Si substrates to support the subsequent growth of GaN. Free-standing ScN crystals could serve as lattice-matched, electrically conductive substrates for other semiconductors such as zinc blende GaN (a = 4.52 Å) [16] and boron phosphide (a = 4.55 Å) [17]. ScN could also be utilized for high temperature ohmic contacts to IIIA nitrides [18]. Large piezoelectric coefficients can be achieved by alloying scandium nitride with aluminum nitride [19,20]. For all of these applications, control over the material's structure and crystal quality is essential.

It has proven to be difficult to produce high quality ScN layers and bulk crystals for several reasons. First, the maximum temperature employed in epitaxial growth studies have been relatively low, 1100 °C for hydride vapor phase epitaxy (HVPE) [21], 1050 °C for molecular beam epitaxy [22], and 950 °C for reactive magnetron sputtering. Such low temperatures result in thin films (<1 µm) with small grain sizes, i.e. high densities of grain boundaries. Second, defects and cracking are often caused by the mismatch of substrate and ScN layer properties (crystal structure, lattice constants, and coefficients of thermal expansion).

ScN has been deposited on many different substrates. Gall *et al.* [23] produced ScN(001) single crystal on MgO(001) and TiN(001) buffer layer on MgO(001) by ultrahigh vacuum reactive magnetron sputter deposition. Ohgaki *et al.* [24] also synthesized ScN films on MgO(110) and α-$Al_2O_3(10\overline{1}0)$ substrates by (MBE), and XRD revealed ScN(220) for both substrates. Edgar *et al*. [21] used (HVPE) to deposit ScN on 6H-SiC(0001), and reported that ScN exhibited (111) orientation and a mixture of (100) and (111) orientations at substrate temperatures of 800-900 ^{o}C and 1000-1100 ^{o}C respectively. Moram *et al.* [25] grew epitaxial 100-oriented ScN films on 100-oriented Si, and mixed orientation of ScN(111) and (100) on Si(111) via (MBE) growth method. Inevitably, this heteroepitaxy results in high dislocation densities and cracking of the films.

Here we demonstrate two advances: the use of physical vapor transport (PVT) for preparing epitaxial ScN layers and a single crystal tungsten (100) substrate. PVT technique is widely employed for the bulk crystal growth of silicon carbide [26] and aluminum nitride [27].

The present study builds on our previous work [2], in which polycrystalline ScN was grown on polycrystalline tungsten foil, by employing (100) tungsten single crystal seeds to produce ScN single crystal. The lattice constant mismatch was minimized by this orientation preference between ScN crystal and the tungsten seed. The lattice constant of tungsten is 3.165 Å, and about ~4.49 - 4.51 Å for ScN. The directed cube-on-cube lattice mismatch is very large, 42.18 % (based on tungsten). However, rotating the unit cell by 45^{o} and considering the square that is formed by the nearest 4 tungsten atoms (Figure 4.1) produce a new square. The diagonal of this new square is about 4.48 Å thus reducing the mismatch dramatically to 0.3 % (based on tungsten). Therefore, the ScN crystal orients on tungsten to minimize the lattice mismatch. A 45° angle exists between the ScN and tungsten unit cells, and results in a plane relationship ScN (001) || W (001) with normal direction ScN [100] || W [110]. This orientational relationship also occurs with titanium nitride on tungsten [28].

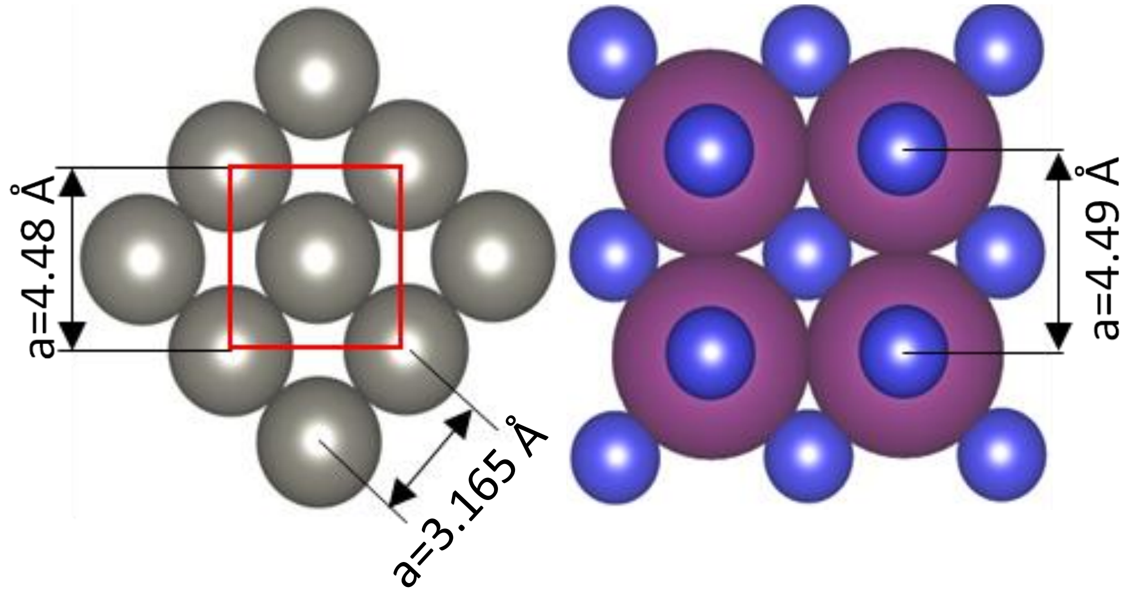

Figure 4.1: *A schematic representation of ScN (200) crystals grown on (200) tungsten. Dark gray spheres are tungsten, large purple spheres and small blue spheres are Sc and N respectively.*

4.3 Experimental Work

The sublimation growth was conducted in a tungsten heating element furnace with a maximum temperature of 2400 °C. Tungsten previously proved to be a good unreactive metal for the sublimation growth of TiN [28] and ErN [29], so it was used as a substrate for the deposited ScN crystals, and to manufacture crucibles used in the experiments.

Ultra-high-purity gases, nitrogen (99.999% N_2) and forming gas (95% Ar and 5% H_2), were used in the experiments. The nitrogen and forming gases were further purified with inline moisture and oxygen purifiers to reduce the impurity concentrations from ppm level to ppb level. Baking in forming gas helped to reduce and to remove oxygen present as native oxides on the surface of the ScN source, the crucible, and the substrate (the tungsten seed). During the baking stage, the furnace was held at 1000 ^oC for two hours. The ScN source was synthesized by heating small chunks of pure Sc metal (99.9 % purity) in ultra-high-purity nitrogen at 1100 ^oC and 500 Torr for 10 hours.

The ScN crystal was grown on a single crystal tungsten seed with a (100) orientation. The tungsten seed was mechanically polished to achieve an optical surface. Cleaning by distilled water, acetone, methanol, and isopropanol sequentially in an ultrasonic cleaner followed the polishing process.

The sublimation was carried out at the temperature range 1850–2000 ^oC and pressure range of 15–35 Torr in the ultra-high-purity nitrogen gas. The growth time varied from 100 hours to 360 hours. The grown ScN crystals were carefully detached from the tungsten seed with a razor blade.

A Rigaku MiniFlex II diffractometer was employed to determine the orientation and lattice constants of the ScN layer by θ-2θ x-ray diffraction. To confirm the epitaxial growth, XRD ϕ scans were taken by Rigaku Smartlab diffractometer. To establish epitaxy, the dome reflections of film and substrate peaks were needed to assure that they are oriented as expected from their crystal symmetry. To do so, the x-ray detector was fixed at $2\theta = 39.9^{o}$, the location of the ScN (200) peak. The post-growth seed (ScN crystal upon W seed) was rotated 360^{o}. Then, the x-ray detector was fixed at $2\theta = 40.2^{o}$ which represents the diffraction of W (110) plane, and 360^{o} the post-growth seed was rotated again. The 45° angle rotation relationship between the ScN film and W seed was confirmed with a Bruker D8 Discover diffractometer. In this measurement, the ScN crystal upon the W seed was rotated to $2\theta =40.2^{o}$ which represents W (110) orientation. Then, it was rotated to $2\theta =57.7^{o}$ which represents ScN (110) orientation.

To determine the structural quality ScN, rocking curve scan was performed to calculate the Full Width at Half Maximum (FWHM) of the ScN (200) peak.

High magnification images of the ScN layer were taken with a scanning electron microscope (SEM) to determine the crystal surface morphology and defects such as steps and cracks.

The surface topography and roughness of the ScN crystal were investigated by atomic force microscopy (AFM).

4.4 Results and Discussions

4.4.1 Out-of-Plane and In-Plane X-ray Diffraction to Confirm the Epitaxilal Growth of ScN Single Crystal

For a ScN crystal removed from the tungsten substrate, only two peaks were evident, the (200) and (400) reflections, at 39.9° and 86.2° respectively in the XRD θ–2θ pattern (Figure 4.2). This suggests that only ScN single crystal of the (100) family was produced.

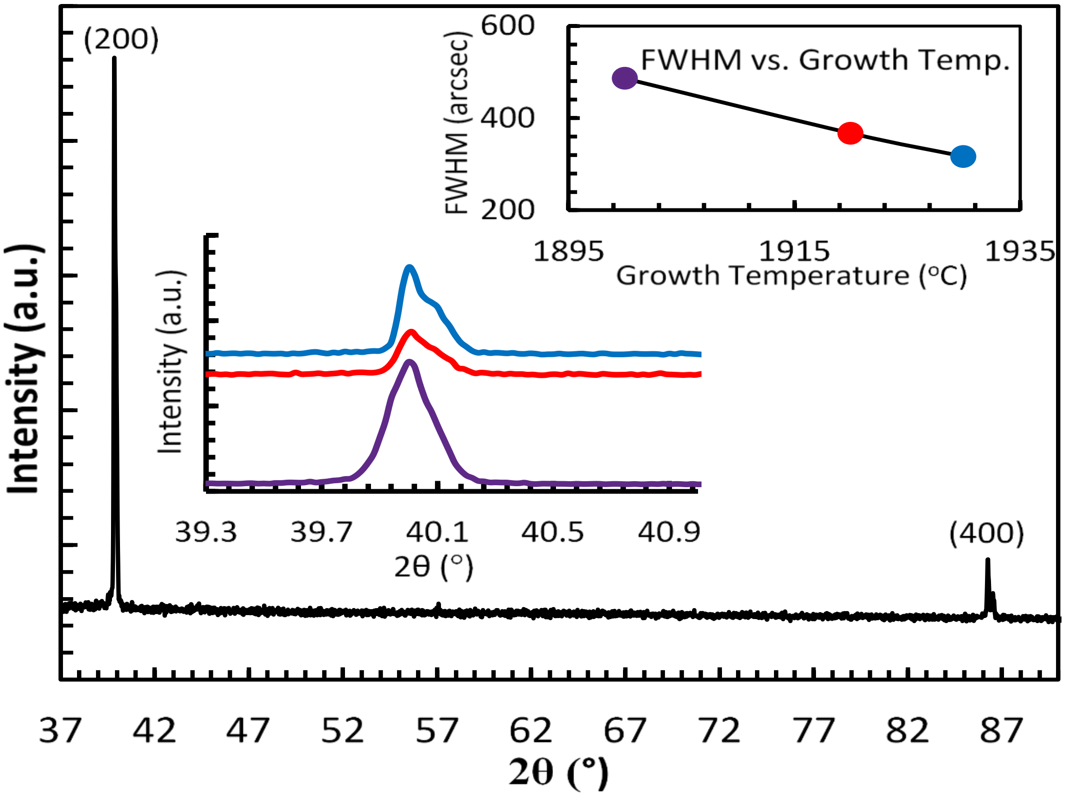

Figure 4.2: *θ-2θ XRD pattern for ScN crystal grown at 1930 °C and 15 Torr. The insets are the FWHM's of ScN (200) at different temperatures.*

The FWHM's of θ-2θ scans decrease as the growth temperature increases, showing that the crystallinity of ScN films improved at higher growth temperature (the insets in Figure 4.2). This was due to greater atom mobility at higher temperatures and the tendency of threading dislocation to recombine with increasing the layer thickness.

In the XRD ϕ scans (not shown) at 39.9° ($ScN_{(200)}$) and 40.2° ($W_{(110)}$) detector positions, peaks appeared at ϕ values of 17°, 107°, 197°, and 287°. For $ScN_{(200)}$, the peaks had different intensities, and this is related to the steps presenting on the crystal surface, which will be explained later. For $W_{(110)}$ the peaks were not intense because the ScN layer has steps, and is so thick and blocks the x-rays from reaching the tungsten substrate.

4.4.2 X-ray Diffraction to Confirm 45° Rotation

XRD analysis of the ScN layer and the tungsten single crystal revealed an orientational relationship of ScN (001) || W (001) with normal direction ScN [100] || W [110], a 45° rotation between the ScN and W lattices, as defined by their primary unit cell directions [100]. The ScN (200) planes are parallel to the substrate surface when the tungsten seed (100) is parallel to the growth surface. However, the tungsten substrate surface was unintentionally slightly tilted away from the (100) plane during cutting and machining the seed. This results in ScN surfaces with steps, but the ScN planes were still parallel with the tungsten (100) plane, and with the in-plane directions ScN [100] || W [110]. To confirm this, the in-plane XRD pattern of ScN (220) and W (110) was performed as shown in Figure 4.3. When the post-growth ScN(100) on W(100) composite was tilted 45°, only two x-ray diffraction peaks were evident: one at 2θ = 57.7° from the ScN(220) plane (ScN (100) plane with 45° tilt) and a second at 2θ = 40.2° which is for W(110) plane (underlying W(100) plane with 45° tilt). This confirms the planes (100) of the ScN and W are parallel, with a 45° angle between the perpendicular ScN [200] and W [110] directions.

4.4.3 Structural Quality of ScN Crystal by X-Ray Rocking Curves

The crystal quality greatly improved with the ScN layer thickness, as evidenced by the decreasing FWHM of x-ray rocking curves (the inset in Figure 4.3). With the ScN layer thickness ranged from 14 to 90 μm, the FWHM decreased from 1438 to 821 arcsec. This improving crystal quality is attributable to a reduction in the dislocation density. The dislocations with opposite Burger's vectors are attracted toward each other as the ScN layer becomes thicker, and ultimately combine and are annihilated. Although XRD ω-2θ pattern revealed a relatively wide FWHM compared to the conventional high quality semiconductors, the ScN grown in this work has the lowest value reported up to date. XRD ω-2θ pattern revealed a relatively wide FWHM for the tungsten seed, which consequently affected the quality of ScN crystal. Table (1) lists the previously reported FWHM's for XRD peaks taken from ScN films.

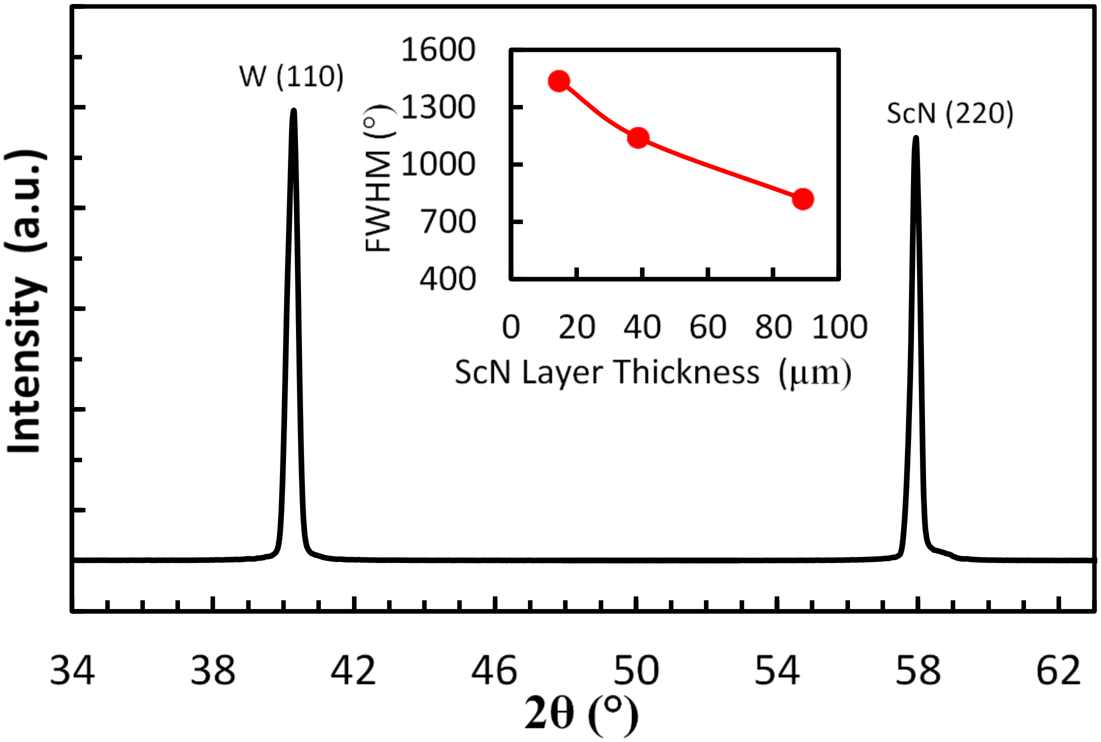

Figure 4.3*: XRD pattern for 45ᵒ (200) plane rotation. The inset is the effect of ScN layer thickness on the FWHM of x-ray rocking curve.*

Table 4.1: *FWHM of Rocking Curve for ScN Single Crystal.*

Growth Method	**Growth Temp. (^oC)**	**Substrate**	**ScN Orientation**	**ScN Layer Thickness (µm)**	**FWHM (arcsec)**
Reactive Magnetron Sputter Deposition[31]	750	MgO (001)	(002)	0.345	3,132
Reactive Magnetron Sputter Deposition[31]	750	MgO (001)	(111)	0.345	7,668
MBE[32].	600 – 1,000	Si (111)	(111)	0.225	1,983 – 7,900
rf-MBE[25]	800	Si (100)	(100)	0.8	2,520
dc- Reactive Magnetron Sputtering[33]	850	MgO (001)	(001)	0.48 – 0.52	2,430
RSMBE[9]	300 - 850	MgO (100)	(200)	0.12 – 0.320	1,260 - 2,340
GSMBE[22]	800	3C-SiC (111)/6H-SiC(0001)	(111)	0.2	1,047
dc- Reactive Magnetron Sputtering[34]	650	MgO (001)	(001)	0.47 – 0.52	2,487 – 2,754
MBE[24]	750 - 900	MgO (110)	(220)	0.1 – 0.15	1,800 – 2,520
MBE[24]	750 - 900	α-Al2O3 (1010)	(110)	0.1 – 0.15	1,760 – 3,960
Present Work by PVT	1,850 – 2,000	W (100)	(200)	14 – 90	821 - 1438

4.4.4 SEM Images

The mismatch in the thermal expansions between the ScN layer and the tungsten seed generated stresses, resulting in cracks on the ScN crystal. Figure 4.4a shows how the cracks were oriented regularly generating square and rectangular shapes of the ScN crystal.

No individual grain boundaries are apparent in the SEM image, but large macrosteps, several microns high, can be seen on the ScN surfaces, as a result of step bunching (Figure 4.4b). In general, step bunching can be caused by the misorientation of the substrate surface from the (100) plane, substrate polishing damage, and extended defects running through the ScN layer. Step bunching is caused by a difference between the distance of neighboring kinks and the surface diffusion distance. In the case of steps forming, the average distance between neighboring kinks is far smaller than the average surface diffusion distance of the adatoms [30]. In other words, the step velocity is higher than the diffusion speed of adatoms. When the kink density is adequately high, steps perform as holes through which adatoms can be drawn in a continuous flow.

4.4.5 AFM

The surface morphologies of the ScN layers grown at different temperatures are compared in Figure 4.5. The morphology of ScN crystal surface was uniform at different growth temperatures and well-ordered steps with step height of about 15 nm were observed when temperature was increased to 2000 ^{o}C . The surface roughness of the ScN

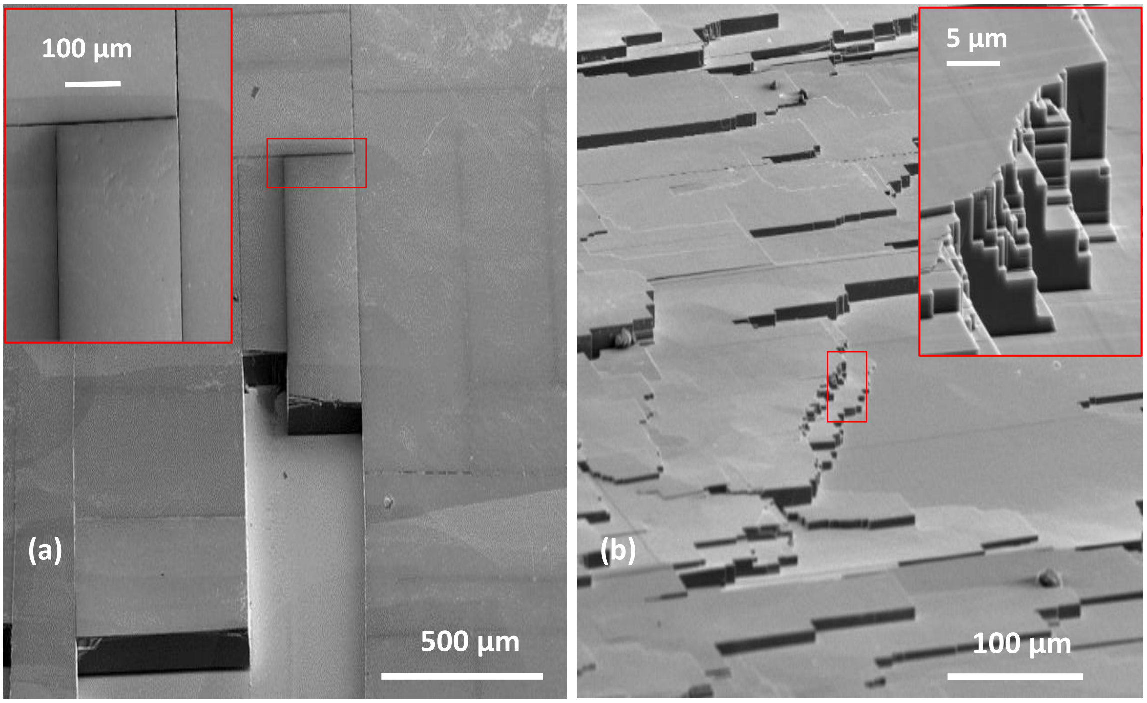

Figure 4.4: *The SEM images of ScN.* ***a*** *shows the cracking of ScN crystal grown at 1950 ^{o}C and 35 Torr due to the difference in the thermal expansion coefficient.* ***b*** *is ScN grown at 1900 ^{o}C and 15 Torr showing the steps formed on the crystal surface.*

films decreased from 83 nm to 18 nm as the growth temperature was increased from 1870 ^{o}C to 2000 ^{o}C because the adatom mobility increases with temperature. The relationship between the log of the film roughness and inverse temperature was linear. This trend indicates that the inverse relationship is a consequence of the thermally activated process which is in accordance with the limited adatom mobility at lower temperature. AFM and SEM showed the ScN surface consisted of both nanometer steps (Figure 4.5d) and much larger micrometer scale steps (Figure 4.4).

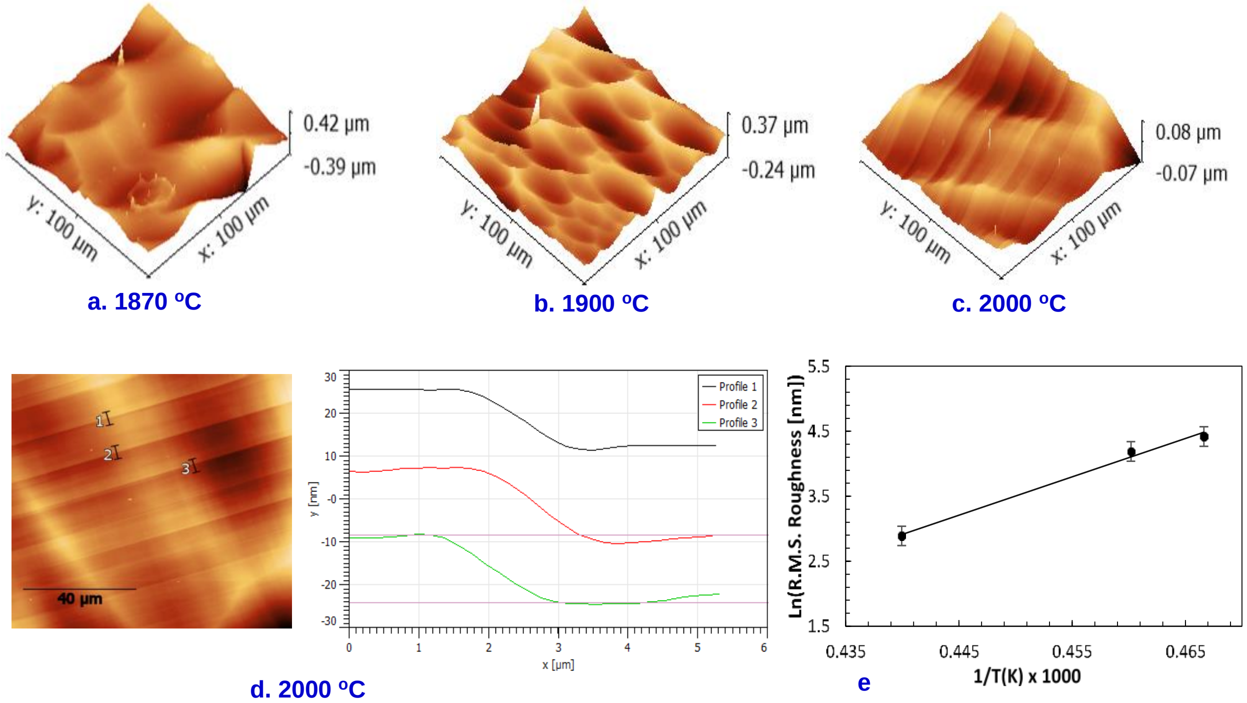

a. 1870 °C

b. 1900 °C

c. 2000 °C

d. 2000 °C

e

Figure 4.5: *AFM images of ScN grown at different temperature, and at 15 Torr. Plot* **e** *represents the effect of growth temperature on the surface roughness.*

4.5 Conclusion

ScN (200) single crystals were grown on W (100) by physical vapor transport method in the temperature range of 1850-2000 °C. Out-of-plane θ-2θ and in-plane ϕ x-ray diffraction scans revealed the epitaxial growth of ScN with a cube-on-cube plane relationship ScN (200) || W (200) and with normal direction ScN [200] || W [110]. The crystal surface exhibited layer-by-layer fashion with steps, and cracks formed due to the difference in the thermal expansion between ScN and W. AFM showed that the growth temperature has a dramatic impact on the roughness of the crystal with an inverse relationship. X-ray rocking curve (XRC) showed that the crystal quality is excellent comparing to the previously reported qualities, and FWHM of ScN produced in this work is the lowest value reported to date.

Acknowledgments

Support for this project from the National Science Foundation Division of Materials Research (award number 1508172) and Higher Committee for Education Development in Iraq is greatly appreciated. This material is based upon work supported by the National Science Foundation under CHE - 1621665.

References

[1] P. Eklund, S. Kerdsongpanya, B. Alling, Transition-metal-nitride-based thin films as novel energy harvesting materials, Journal of Materials Chemistry C. 4 (2016) 3905-3914.

[2] Z. Gu, J. Edgar, J. Pomeroy, M. Kuball, D. Coffey, Crystal growth and properties of scandium nitride, J. Mater. Sci. : Mater. Electron. 15 (2004) 555-559.

[3] J. Dismukes, W. Yim, J. Tietjen, R. Novak, Vapor deposition of semiconducting mononitrides of scandium, yttrium, and the rare-earth elements, RCA Review. 31 (1970) 680-691.

[4] J. Dismukes, W. Yim, V. Ban, Epitaxial growth and properties of semiconducting ScN, J. Cryst. Growth. 13 (1972) 365-370.

[5] W. Lengauer, Investigations in the scandium-nitrogen system, Journal of Solid State Chemistry. 76 (1988) 412-415.

[6] D. Gall, M. Stoehr, J. Greene, Vibrational modes in epitaxial Ti 1− x Sc x N (001) layers: An ab initio calculation and Raman spectroscopy study, Physical Review B. 64 (2001) 174302.

[7] M.A. Moram, Z.H. Barber, C.J. Humphreys, T. Joyce, P. Chalker, Young's modulus, Poisson's ratio, and residual stress and strain in (111)-oriented scandium nitride thin films on silicon, J. Appl. Phys. 100 (2006) 023514.

[8] Y. Kumagai, N. Tsunoda, F. Oba, Point Defects and p-Type Doping in ScN from First Principles, Physical Review Applied. 9 (2018) 034019.

[9] T. Ohgaki, K. Watanabe, Y. Adachi, I. Sakaguchi, S. Hishita, N. Ohashi, H. Haneda, Electrical properties of scandium nitride epitaxial films grown on (100) magnesium oxide substrates by molecular beam epitaxy, J. Appl. Phys. 114 (2013) 093704.

[10] B. Saha, M. Garbrecht, J.A. Perez-Taborda, M.H. Fawey, Y.R. Koh, A. Shakouri, M. Martin-Gonzalez, L. Hultman, T.D. Sands, Compensation of native donor doping in ScN: Carrier concentration control and p-type ScN, Appl. Phys. Lett. 110 (2017) 252104.

[11] G. Samsonov, M. Lyutaya, V. Neshpor, PREPARATION AND PHYSICO-CHEMICAL PROPERTIES OF SCANDIUM NITRIDE, Zh.Prikl.Khim. 36 (1963).

[12] N. Sclar, Properties of Rare-Earth Nitrides, J. Appl. Phys. 35 (1964) 1534-1538.

[13] C.T. Horovitz, Scandium : its occurrence, chemistry, physics, metallurgy, biology, and technology, London; New York : Academic Press, London; New York, 1975.

[14] M. Moram, M. Kappers, T. Joyce, P. Chalker, Z. Barber, C. Humphreys, Growth of dislocation-free GaN islands on Si (1 1 1) using a scandium nitride buffer layer, J. Cryst. Growth. 308 (2007) 302-308

[15] L. Lupina, M. Zoellner, T. Niermann, B. Dietrich, G. Capellini, S. Thapa, M. Haeberlen, M. Lehmann, P. Storck, T. Schroeder, Zero lattice mismatch and twin-free single crystalline ScN buffer layers for GaN growth on silicon, Appl. Phys. Lett. 107 (2015) 201907.

[16] T. Lei, T. Moustakas, R. Graham, Y. He, S. Berkowitz, Epitaxial growth and characterization of zinc-blende gallium nitride on (001) silicon, J. Appl. Phys. 71 (1992) 4933-4943.

[17] T. Chu, J. Jackson, A. Hyslop, S. Chu, Crystals and epitaxial layers of boron phosphide, J. Appl. Phys. 42 (1971) 420-424.

[18] R. Kaplan, S. Prokes, S. Binari, G. Kelner, Growth and properties of scandium epitaxial films on GaN, Appl. Phys. Lett. 68 (1996) 3248-3250.

[19] M. Akiyama, T. Kamohara, K. Kano, A. Teshigahara, Y. Takeuchi, N. Kawahara, Enhancement of piezoelectric response in scandium aluminum nitride alloy thin films prepared by dual reactive cosputtering, Adv Mater. 21 (2009) 593-596.

[20] Y. Lu, M. Reusch, N. Kurz, A. Ding, T. Christoph, M. Prescher, L. Kirste, O. Ambacher, A. Žukauskaitė, Elastic modulus and coefficient of thermal expansion of piezoelectric Al1− xScxN (up to x= 0.41) thin films, APL Materials. 6 (2018) 076105.

[21] J.H. Edgar, T. Bohnen, P. Hageman, HVPE of scandium nitride on 6H–SiC (0 0 0 1), J. Cryst. Growth. 310 (2008) 1075-1080.

[22] S.W. King, R.F. Davis, R.J. Nemanich, Gas source molecular beam epitaxy of scandium nitride on silicon carbide and gallium nitride surfaces, Journal of Vacuum Science & Technology A: Vacuum, Surfaces, and Films. 32 (2014) 061504.

[23] D. Gall, M. Städele, K. Järrendahl, I. Petrov, P. Desjardins, R. Haasch, T. Lee, J. Greene, Electronic structure of ScN determined using optical spectroscopy, photoemission, and ab initio calculations, Physical Review B. 63 (2001) 125119.

[24] T. Ohgaki, I. Sakaguchi, N. Ohashi, H. Haneda, Heteroepitaxial growth and electric properties of (110)-oriented scandium nitride films, J. Cryst. Growth. 476 (2017) 12-16.

[25] M. Moram, S. Novikov, A. Kent, C. Nörenberg, C. Foxon, C. Humphreys, Growth of epitaxial thin films of scandium nitride on 100-oriented silicon, J. Cryst. Growth. 310 (2008) 2746-2750.

[26] T. Kimoto, Bulk and epitaxial growth of silicon carbide, Progress in Crystal Growth and Characterization of Materials. 62 (2016) 329-351.

[27] J. Edgar, L. Liu, B. Liu, D. Zhuang, J. Chaudhuri, M. Kuball, S. Rajasingam, Bulk AlN crystal growth: self-seeding and seeding on 6H-SiC substrates, J. Cryst. Growth. 246 (2002) 187-193.

[28] L. Du, J.H. Edgar, E.A. Kenik, H. Meyer, Sublimation growth of titanium nitride crystals, J. Mater. Sci. : Mater. Electron. 21 (2010) 78.

[29] H.A. Al Atabi, Z.F. Al Auda, B. Padavala, M. Craig, K. Hohn, J.H. Edgar, Sublimation Growth and Characterization of Erbium Nitride Crystals, Crystal Growth & Design. 18 (2018) 3762.

[30] Y. Li, X. Chen, J. Su, Study on formation of step bunching on 6H-SiC (0001) surface by kinetic Monte Carlo method, Appl. Surf. Sci. 371 (2016) 242-247.

[31] D. Gall, I. Petrov, N. Hellgren, L. Hultman, J. Sundgren, J. Greene, Growth of poly- and single-crystal ScN on MgO (001): Role of low-energy N 2 irradiation in determining texture, microstructure evolution, and mechanical properties, J. Appl. Phys. 84 (1998) 6034-6041.

[32] M. Moram, T. Joyce, P. Chalker, Z. Barber, C. Humphreys, Microstructure of epitaxial scandium nitride films grown on silicon, Appl. Surf. Sci. 252 (2006) 8385-8387.

[33] P.V. Burmistrova, J. Maassen, T. Favaloro, B. Saha, S. Salamat, Y. Rui Koh, M.S. Lundstrom, A. Shakouri, T.D. Sands, Thermoelectric properties of epitaxial ScN films deposited by reactive magnetron sputtering onto MgO (001) substrates, J. Appl. Phys. 113 (2013) 153704.

[34] P.V. Burmistrova, D.N. Zakharov, T. Favaloro, A. Mohammed, E.A. Stach, A. Shakouri, T.D. Sands, Effect of deposition pressure on the microstructure and thermoelectric properties of epitaxial ScN (001) thin films sputtered onto MgO (001) substrates, J. Mater. Res. 30 (2015) 626-634.

Chapter 5: A cooling fin to enhance the efficiency of crystal growth by physical vapor transport

- *This chapter was the basis for a paper submitted to Materials Science and Engineering: B journal, 2018.*
- *It is also a part of the provisional invention titled "METHODS OF GROWING SINGLE CRYSTAL MATERIALS" KSURF Disclosures 2017-065 and 2018-023.*

A cooling fin to enhance the efficiency of crystal growth by physical vapor transport

Hayder A. Al-Atabi[a,b], *Mohamad I. Cheikh*[c], *M. H. Hosni*[d], *and J. H. Edgar*[a*]

a: Department of Chemical Engineering, Kansas State University, Manhattan, KS 66506, United States.

b: Chemical Engineering Department, The University of Technology, Baghdad, Iraq.

c: Department of Mechanical and Aerospace Engineering, University at Buffalo, Buffalo, NY 14260, United States.

d: Department of Mechanical and Nuclear Engineering, Kansas State University, Manhattan, KS 66506, United States.

5.1 Abstract

In general for crystal growth, material should deposit on the seed crystal and not on any adjacent supporting structures. This efficiently uses the source material and avoids the possibility of spurious polycrystals encroaching on, and interfering with the single crystal growth. In this paper a new crucible design with a cooling fin in contact with the seed was simulated and experimentally demonstrated on the physical vapor transport (PVT)

---

[*] Corresponding author
E-mail address: edgarjh@ksu.edu (J. H. Edgar)

crystal growth of scandium nitride. The heat transfer of the growth cavity for a conventional crucible and a modified crucible with the cooling fin were modeled theoretically via computational fluid dynamics (CFD) with FLUENT. The CFD results showed that the seed in the modified crucible was approximately 10 °C cooler than the crucible lid, while in the conventional crucible the temperature of the seed and lid were uniform. The experimental results showed that increasing the temperature gradient between the source and the seed by employing the cooling fin led to a dramatic increase in the growth rate of ScN on the seed and reduced growth on the lid. The relative growth rates were 80 % and 20 % on the seed and lid respectively, in the modified crucible, compared to 25% and 75% with the conventional crucible. Thus, the modified crucible improved the process by increasing the growth rate of single crystals grown by sublimation.

Key words: Seeded Crystal Growth, Physical Vapor Transport, Crystal growth Simulation

5.2 Introduction

The seeded sublimation crystal growth technique (modified Lely method) has been widely used to produce wide bandgap semiconductor crystals such as silicon carbide and aluminum nitride [1], as well as titanium nitride [2], yttrium nitride [3], and erbium nitride [4]. Recently, we also demonstrated the single crystal growth of the semiconductor scandium nitride (ScN), a group IIIB transition metal nitride, on single crystal tungsten

(100) seeds via this method [5]. Since the growth rate in this process was relatively slow, less than 1.0 micron/h, it is important to make it as efficient as possible.

To improve the process efficiency, our goal was to get the sublimed material to deposit only at the desired location, the seed crystal. If the temperature is uniform, the sublimed material may crystallize on other parts of the growth cavity (the crucible wall and lid) instead of the seed. Not only does this reduce the process efficiency, but material not deposited on the seed is polycrystalline, thus it can interfere with single crystal growth, if it overgrows the seed.

The present work was undertaken to design a new crucible that is capable of selectively growing ScN crystal on the seed by exploiting the heat transfer phenomenon inside the growth cavity. The specially configured crucible design incorporates a heat transfer fin that is in a heat-conductive relationship with the seed. The cooling fin increases the temperature gradient between the seed and the surrounding parts inside the crucible, slightly cooling the seed surface and creating a stronger driving force for crystal growth there as compared to other surfaces within the crucible; thus leading to higher growth rate on the seed. This new design can be applied to all PVT seeded growth including wide bandgap crystals such as silicon carbide and aluminum nitride. The behavior of the new crucible design was predicted theoretically by computation fluid dynamics (CFD) simulation and verified experimentally.

The bulk growth of crystals via the physical vapor transport (PVT) method includes: the global heat transfer phenomena which is fundamentally comprised of conduction, convection, radiation, induction heating, and the heat of sublimation and crystallization at the source-vapor and vapor-crystal interfaces [6]; mass transport by sublimation and condensation; Stefan flow; buoyancy force; and the kinetics of dissociation and deposition [7,8]. Modeling and simulation have become attractive alternatives to expensive and time consuming crystal growth experiments for optimizing the growth processes conditions. In addition, it can provide additional insights into experiments, especially when it becomes difficult or impossible to directly measure parameters inside the reactor [9].

Although the crystal growth process is frequently related to the materials chemistry and physics, the fluid dynamics is also tremendously important. It controls the momentum, energy, and mass transport [7]. In the energy term, the growth temperature and temperature distribution in a growth chamber can significantly affect the local growth rate along the growth interface [8]. Knowing these parameters can help to control the local temperature distribution inside the crucible where the crystal growth occurs. Since the PVT process takes place in a black box [10,11] and is difficult to monitor, the simulated temperature field provides qualitative and quantitative information on the growth history as a function of the process parameters and geometry. Enormous strides and advancements have been achieved with models for simulating the PVT process utilizing finite element-or finite volume-based software aided design. Therefore modeling and simulation of the crystal growth processes have attained a point where they can reliably predict the fundamental physical phenomena of the process, and provide guidance for modifying the system design to improve the process [7].

Tsvetkov [12] stated that slight changes in crucible design produces differences in the crystal shapes and the densities of defects formed due to modifications of the temperature and temperature gradients inside the crucible. This temperature variation can also change the growth rate over the seed.

5.3 Simulation and Experimental Work

The steady state process simulation was performed with FLUENT, a CFD package from ANSYS Inc. A conventional and a modified crucible with a cooling fin (extended surface) were simulated to investigate the effect of the fin on the ScN growth rate on the seed. Gravity was set to 9.81 m/sec^2 in the negative z-direction. The gas inside and outside the crucible was modeled using the ideal gas law, while the viscosity and specific heat where modeled using kinetic theory. As for nitrogen outside the domain, a pressure inlet was implemented with a gauge pressure equal to zero and absolute pressure equal to 35 Torr. A linear temperature profile was set at the boundaries of the domain (solid W-wall, and N_2 pressure inlet), in accordance with Müller *et al*. [13]. The profile varied in the z-direction starting at 2000 ^oC at the lowest point and ending at 1850 ^oC at the highest point. For the top boundary condition, the top surface of the fin in the modified crucible or the external top surface of the lid in the conventional crucible, the temperature was fixed at

1850 ^{o}C whether the boundary was a pressure-inlet as the conventional case, or a solid tungsten wall as the modified case.

Two different computational meshes were constructed for each case. The two meshes were constructed in a similar way. The solid regions were filled with hexahedral cells, while the fluid regions consist of a hybrid mesh with tetrahedral and hexahedral cells. Near the seed, the region was mostly filled with unstructured tetrahedral mesh cells. The mesh was refined towards the walls and solid structures in order to resolve the flow and physical phenomena near the wall in more detail. The total number of cells for the conventional case was 3,912,317 with 436,495 hexahedral cells, while the total number of cells for the modified case was 4,096,867 with 356,651 hexahedral cells. The largest cell size for both cases was 0.4mm.

The experimental sublimation growth was conducted in a tungsten heating element furnace with a maximum temperature of 2400 ^{o}C. The furnace chamber is stainless steel. Tungsten had previously proved to be a good unreactive metal for the sublimation growth of AlN [1], TiN [2], and ErN [4], so it was used as a substrate for the deposited ScN crystals, and for the crucibles used in the experiments. The scandium nitride source was placed in the tungsten crucible with 25 mm i.d., 30 mm o.d., and 50 mm long. Two pairs of tungsten wire mesh elements heat the crucible. Tungsten thermal shields were employed to contain the heat on the crucible. Between the thermal shields and the chamber was a water cooling system comprised of a shell and tube copper jacket.

To provide an axial temperature difference between the ScN source and growth zones, which is the driving force of the growth, the top of the crucible was not insulated by the tungsten thermal shields. Thus, it was colder than the crucible bottom.

Ultra-high-purity gases, nitrogen and forming gas (95% Ar and 5% H_2), were used in the experiments. To purify the gases, three purifiers were installed on the gas line: a moisture purifier, a high oxygen concentration purifier in ppm level, and low oxygen concentration purifier in ppb level before the gas (either nitrogen or forming gas) enters the furnace chamber. Baking in forming gas helped to reduce and to remove oxygen present as native oxides on the surfaces of the ScN source, the crucible, and the substrate (the tungsten seed). During the baking stage, the furnace was held at 1000 ^oC for two hours. Then, the furnace chamber was cooled down to the room temperature, and the gas line was switched to nitrogen to start the growth experiments. The ScN source was synthesized by heating small chunks of pure Sc metal (99.9 % purity) in the ultra-high-purity nitrogen at 1100 ^oC and 500 Torr for ten hours.

The tungsten (100) substrate (the seed) was prepared by cutting slices that were then machined to a specific design to fit inside the tungsten crucible. The diameter of the seed side facing the ScN source was 8 mm, while the diameter of the other side was 9 mm. The seed was polished and followed by cleaning with distilled water, acetone, methanol, and isopropanol sequentially using a sonicator. A tungsten lid with 25 mm i.d. and 30 mm o.d. was designed to hold the seed. A circular cooling fin with a 30 mm diameter was set on the other side of the seed to selectively cool the seed to provide a higher driving force for crystal growth between the seed and the ScN source, and consequently higher growth rate on the seed. In other words, ScN would deposit on the seed (the colder spot) rather than the crucible lid. Figure 5.1 shows the configuration of the crucible, seed, lid, and fin used in the experiments.

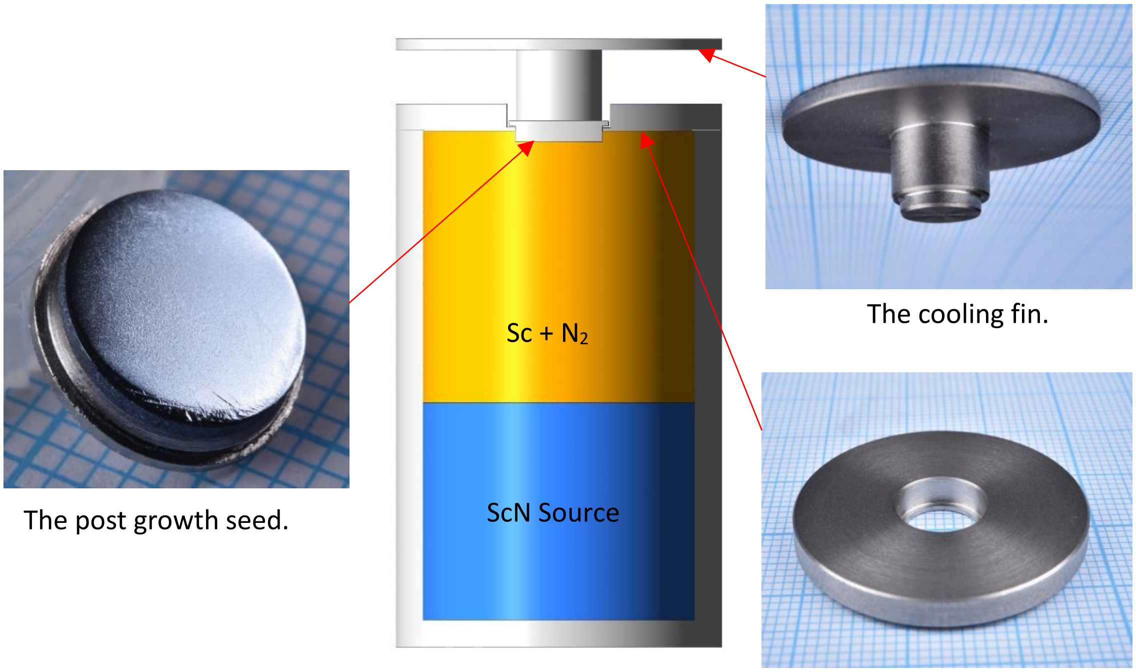

The cooling fin.

The post growth seed.

The crucible.

The lid/seed holder.

Figure 5.1*: The configuration of the modified PVT crucible.*

The distance between the ScN source and the growth area (the tungsten single crystal seed) was kept constant at approximately 2.5 cm. The sublimation was carried out over a temperature range of 1850–2000 ^{o}C (from the bottom of the crucible to the seed) and pressure of 35 Torr in the ultra-high-purity nitrogen gas. During start-up, the furnace temperature was ramped up at 400 ^{o}C/hr to the growth temperature. The ScN crystals were grown by maintaining that dwell temperature. The growth time was 100 hours.

The seed and the lid were weighed before and after the growth to calculate the growth rate. An optical microscope was used to image the resulting ScN crystals.

5.4 Results and Discussion

5.4.1 Axial temperature distribution and the difference between the crucibles

The axial temperature distribution along the crucibles was simulated as shown in Figure 5.2a for the conventional crucible without a fin, and a modified crucible with a fin (Figure 5.2b). As can be seen, the region around the seed (the vapor region) in the case of the modified crucible was colder than the region in the case of the conventional crucible. This shows how the fin affected not only the solid phase (the tungsten seed and lid) but also the vapor phase.

5.4.2 Radial temperature distribution along the crucible

Figure 5.3 shows the radial temperature distribution. In the bottom of the crucible, the temperature is higher in the center, while in the top half of the crucible the radial temperature distribution starts to flip and is cooler in the center especially when the fin is present. The thermal conductivity of tungsten (104 W/m·K) [14] is much higher than that of N_2 (0.11 W/m·K) [15] thus including the fin created a lower thermal resistance in the center of the crucible than other regions leading to an inflection in the radial temperature profile from convexity to concavity.

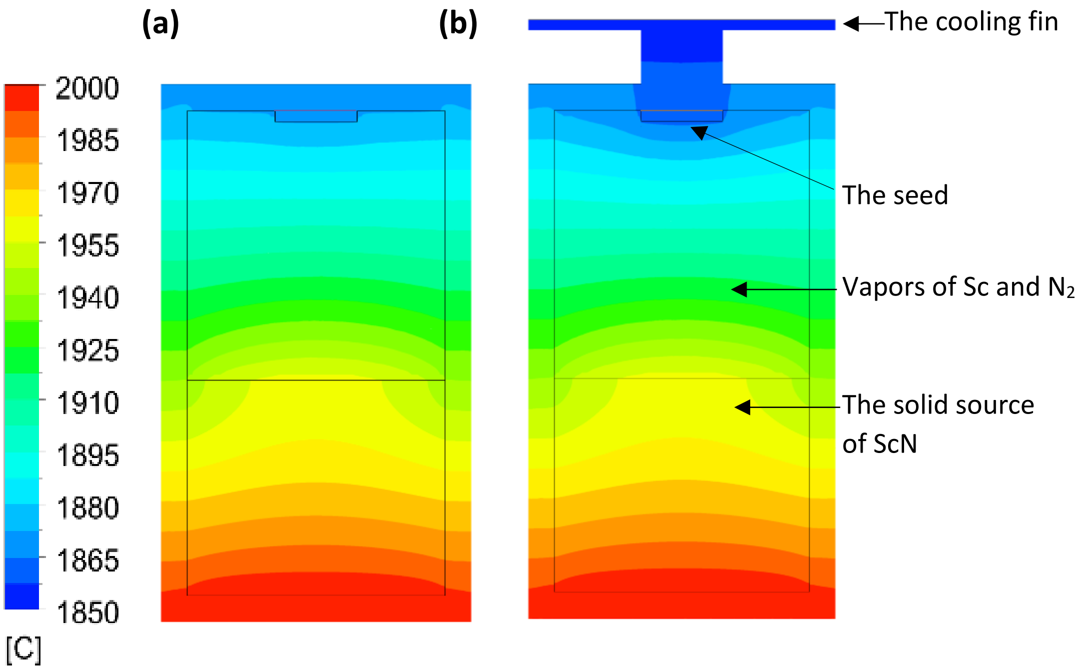

Figure 5.2: *The axial temperature distribution in (a) the conventional crucible and (b) the modified crucible. The solid lines inside the growth cavity are the boundaries of the solid phase, the crucible wall, the lid, ScN source, and the seed.*

5.4.3 The effect of the cooling fin on the ScN growth rate on the seed

Figure 5.4 shows the radial temperature distribution on the seed and the internal lid surface (only the solid phase) for both cases, the no-fin case and fin case. In the no-fin case, the temperature is higher at the seed than that at the holder, and is equal to the holder temperature at some spots leading to an equal growth rate on the seed and the holder. The growth rate on the holder could even be higher than on the seed. This phenomena is attributed to the higher thermal resistance in the seed region than that of the lid. In other words, installing the seed on the internal surface of the lid increases the thickness of the solid in this region (seed thickness plus lid thickness) which consequently increases the resistance of heat transfer through the solid phase in the seed region. However, the trend was opposite after installing the fin: the seed became colder than the lid surface because the cooling fin draws the heat from the seed only to the outside of the crucible.

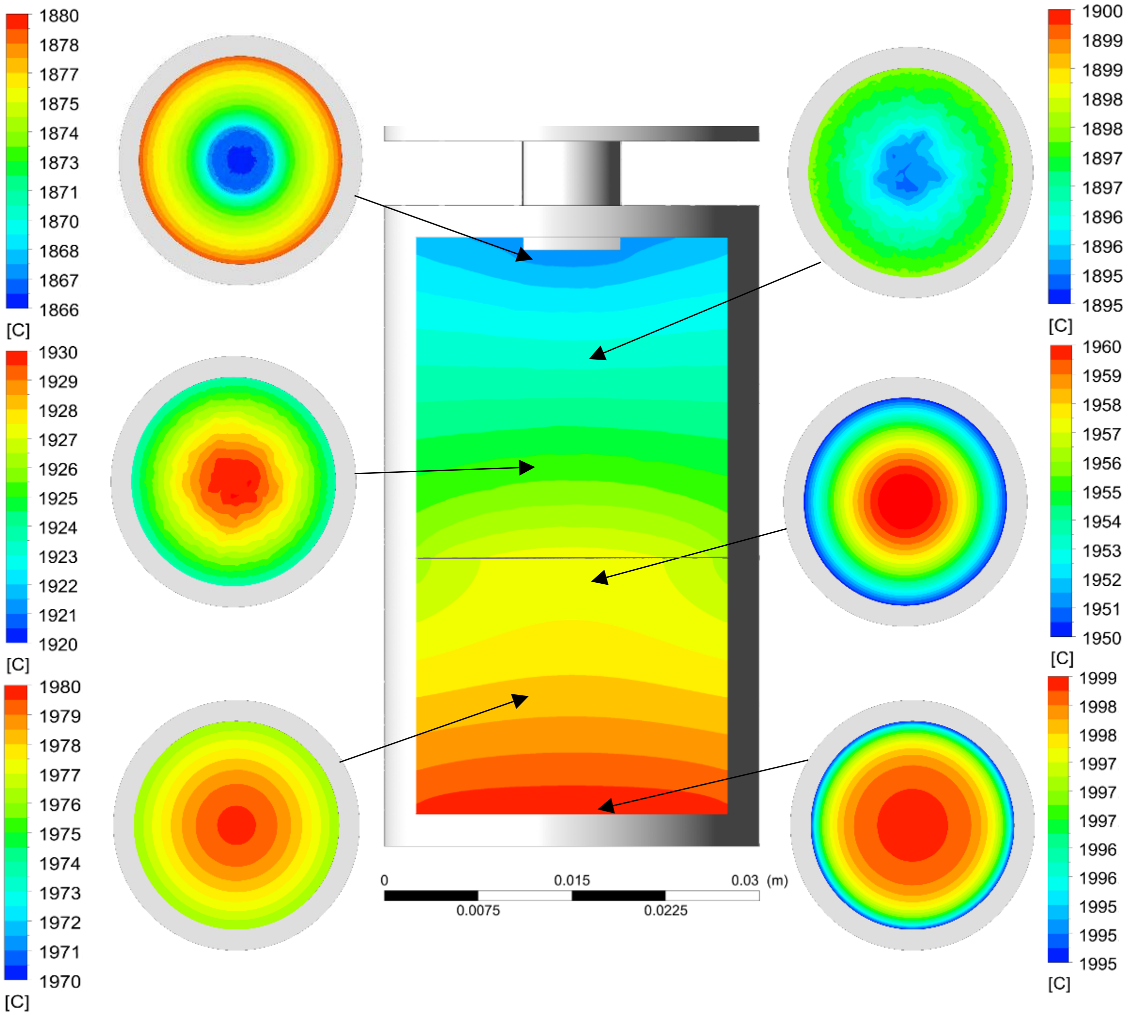

Figure 5.3: *The radial temperature distribution along the modified crucible.*

Inserting the fin reduced the temperature from 1876 ^{o}C on the internal lid surface to 1866 ^{o}C on the seed.

The impact of the lower seed temperature was tested experimentally. The cooling fin drew the heat away from the seed, so the majority of the vapors of Sc and N2 were directed to the seed, where the single crystal growth reaction took place, rather than other surfaces within the growth cavity. Figure 5.5 shows the amount of deposited ScN using the conventional seeded growth crucible and the modified crucible. From the microphotographs (see Figure 5.5a), it is evident that the polycrystalline ScN grown on the lid is much less in the modified crucible than that in the conventional crucible.

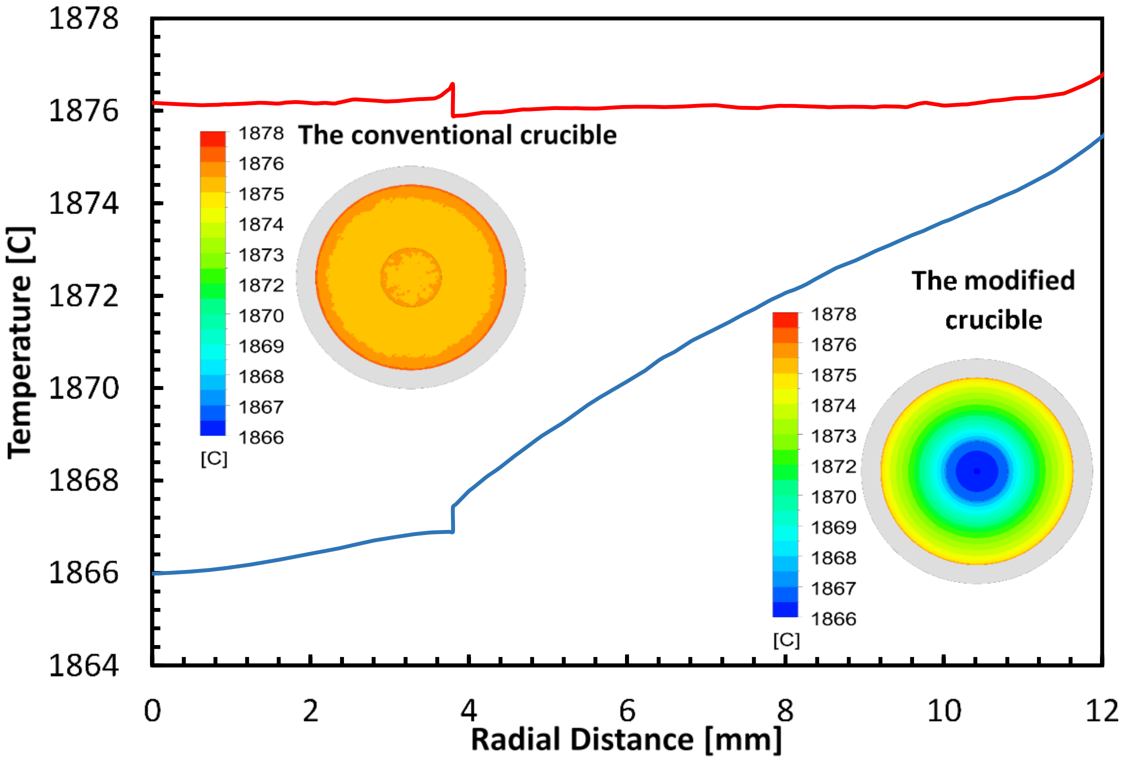

Figure 5.4: *The radial temperature distribution on the seed and the lid (the solid phase only).*

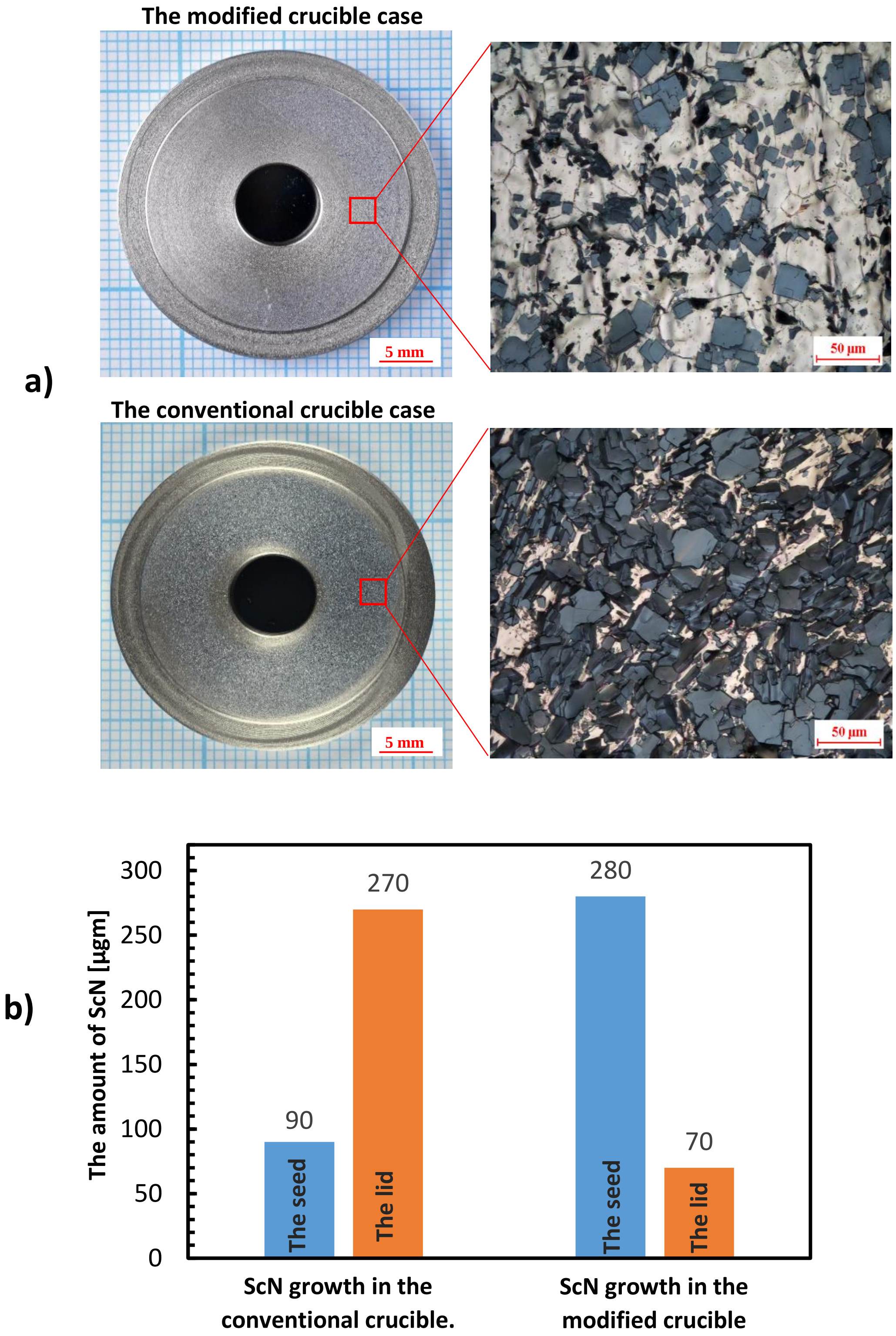

Figure 5.5: *The effect of the cooling fin on the amount/mass of the ScN crystal. (a) photographs for ScN deposited on the lid. (b) the weights of ScN deposited on the lid and the seed.*

Consequently, there was a dramatic increase in the mass of the single crystal ScN grown in the modified crucible comparing to the conventional crucible as shown in Figure 5.5b. This improves the overall efficiency of the growth process of ScN single crystal, and reduces the possibility of crystal growth in other regions, thereby suppressing polycrystalline growth.

5.4.4 The Fin Efficiency

The fin efficiency is a measure of a potential reduction in temperature between the fin and the ambient fluid due to conductive heat transfer along the fin and convective heat transfer from the fin surface.

The fin efficiency is defined by the following equation [16]:

$$\eta_f = \frac{actual\ heat\ transfer\ by\ a\ fin}{heat\ transfered\ if\ the\ entire\ fin\ were\ at\ the\ base\ temperature} \quad (1)$$

Equation (1) is the ratio of the actual heat transfer rate through the fin base divided by the maximum possible heat transfer rate through the fin base. This could be obtained if the entire fin were at the base temperature. Most practical fins are thin, so they are considered as one-dimensional with standard idealizations used for the analysis [17]. The one-dimensional fin efficiency is a function of the fin geometry, fin material thermal conductivity, and convective heat transfer coefficient at the fin surface. It is not, however, a function of the fin base or fin tip temperature, or ambient temperature.

For the circular fin, the efficiency can be calculated from the following correlations:

$$\eta_f = \begin{cases} a(ml_e)^{-b} & for\ \varphi > 0.6 + 2.257(r^*)^{-0.445} \\ \frac{\tanh(\varphi)}{\varphi} & for\ \varphi \leq 0.6 + 2.257(r^*)^{-0.445} \end{cases} \tag{2}$$

$$a = (r^*)^{-0.246} \quad ; \quad \varphi = ml_e(r^*)^n \quad ; \quad n = e^{0.13ml_e - 1.3863} \tag{3}$$

$$b = \begin{cases} 0.9107 + 0.0893r^* & for\ r^* \leq 2 \\ 0.9706 + 0.17125 \ln r^* & for\ r^* > 2 \end{cases} \tag{4}$$

$$m = \left(\frac{2h}{k_f\delta}\right)^{1/2} \quad ; \quad l_e = l_f + \frac{\delta}{2} \quad ; \quad r^* = \frac{d_e}{d_o} \tag{5}$$

Where:

k_f and h are the thermal conductivity of the fin and the convective heat transfer coefficient respectively. The other variables (d_e, d_o, δ, and l_f) are defined in Figure 5.6.

In this study, the fin efficiency was about 95%. This high efficiency is due to the low convective heat transfer coefficient (h) where it was 7.22 W/(m^2·K).

Figure 5.6: *The design of the fin used in this work.*

5.5 Conclusion

The new crucible design with the cooling fin dramatically improved the growth rate of the ScN crystal on the seed via physical vapor transport method comparing to the conventional crucible design. The process simulation by CFD technique employing FLUENT package was performed and validated experimentally. In the modified crucible, the temperature of the seed was colder than the crucible lid in about 10 ^{o}C, while in the conventional crucible the seed was equal or higher than the lid temperature. Decreasing the seed temperature increased the temperature gradient, the driving force of the growth, between the seed and the ScN source. The experimental results showed that the growth rate on the seed increased from 25% in the conventional crucible to 80% in the modified crucible. The calculated fin efficiency was 95% which demonstrates the low heat transfer coefficient (h =7.22 W/m^2-K). The new crucible design with the cooling fin is generally applicable to all seeded crystal growth by physical vapor transport.

Acknowledgments

Support for this project from the National Science Foundation Division of Materials Research (award number 1508172) and Higher Committee for Education Development in Iraq (HCED) is greatly appreciated.

References

[1] B. Liu, J. Edgar, Z. Gu, D. Zhuang, B. Raghothamachar, M. Dudley, A. Sarua, M. Kuball, H. Meyer III, The durability of various crucible materials for aluminum nitride crystal growth by sublimation, Materials Research Society Internet Journal of Nitride Semiconductor Research. 9 (2004).

[2] L. Du, J.H. Edgar, E.A. Kenik, H. Meyer, Sublimation growth of titanium nitride crystals, J. Mater. Sci. : Mater. Electron. 21 (2010) 78.

[3] L. Du, J. Edgar, R.A. Peascoe-Meisner, Y. Gong, S. Bakalova, M. Kuball, Sublimation crystal growth of yttrium nitride, J. Cryst. Growth. 312 (2010) 2896-2903.

[4] H.A. Al Atabi, Z.F. Al Auda, B. Padavala, M. Craig, K. Hohn, J.H. Edgar, Sublimation Growth and Characterization of Erbium Nitride Crystals, Cryst. Growth Des. 18 (2018) 3762-3766.

[5] Hayder A. Al Atabi, N. Khan, E. Nour, J.Mondoux, Y. Zhang, and J.H. Edgar, Bulk (100) scandium nitride crystal growth by sublimation on tungsten single crystal seeds, Appl. Phys. Lett. 113 122106 (2018).

[6] S.G. Müller, R. Eckstein, J. Fricke, D. Hofmann, R. Hofmann, R. Horn, H. Mehling, O. Nilsson, Experimental and theoretical analysis of the high temperature thermal conductivity of monocrystalline SiC. 264 (1998) 623-626.

[7] Q. Chen, Y. Jiang, J. Yan, M. Qin, Progress in modeling of fluid flows in crystal growth processes, Progress in Natural Science. 18 (2008) 1465-1473.

[8] R. Ma, H. Zhang, V. Prasad, M. Dudley, Growth kinetics and thermal stress in the sublimation growth of silicon carbide, Cryst. Growth Des. 2 (2002) 213-220.

[9] M. Pons, M. Anikin, K. Chourou, J. Dedulle, R. Madar, E. Blanquet, A. Pisch, C. Bernard, P. Grosse, C. Faure, State of the art in the modelling of SiC sublimation growth, Materials Science and Engineering: B. 61 (1999) 18-28.

[10] S. Nishizawa, H. Yamaguchi, T. Kato, M.N. Khan, K. Arai, N. Oyanagi, Y. Kitou, W. Bahng, New crucible design for SiC single crystal growth by sublimation, MRS Online Proceedings Library Archive. 640 (2000).

[11] S.I. Nishizawa, T. Kato, Y. Kitou, N. Oyanagi, F. Hirose, H. Yamaguchi, W. Bahng, K. Arai, High-quality SiC bulk single crystal growth based on simulation and experiment. 457 (2004) 29-34.

[12] V.F. Tsvetkov, R. Glass, D. Henshall, D. Asbury, C.H. Carter Jr, SiC seeded boule growth. 264 (1998) 3-8.

[13] M. St G, R. Glass, H. Hobgood, V. Tsvetkov, M. Brady, D. Henshall, J. Jenny, D. Malta, C. Carter Jr, The status of SiC bulk growth from an industrial point of view, J. Cryst. Growth. 211 (2000) 325-332.

[14] J.G. Hust, A.B. Lankford, , Thermal conductivity of aluminum, copper, iron, and tungsten for temperatures from 1 K to the melting point NBSIR report No. PB84-235878 (1984) 259.

[15] S. Saxena, S. Chen, Thermal conductivity of nitrogen in the temperature range 350–2500 K, Mol. Phys. 29 (1975) 1507-1519.

[16] J.H. Lienhard, A heat transfer textbook, Courier Corporation, 2013.

[17] L. Huang, R. Shah, Assessment of calculation methods for efficiency of straight fins of rectangular profile, Int J Heat Fluid Flow. 13 (1992) 282-293.

Chapter 6: Conclusions and Future Work

6.1 Conclusions

The experimental results showed the effectiveness of physical vapor transport method of growing bulk crystals of ErN and ScN. Tungsten metal employed in this work proved its thermal and chemical stability for the sublimation of both compounds. Single crystals of ScN were grown on tungsten single crystal seed with a lattice mismatch of 0.3 %. A new crucible was designed by the CFD technique then validated experimentally by demonstrating a high growth rate of ScN.

The growth temperature had a dramatic impact on the ErN crystal growth, both the rate and crystal morphology. The growth rate increased exponentially with increasing temperature. At 1620 ^{o}C, small crystals with rough surfaces were grown. As the temperature increased (>1620 ^{o}C), the crystal size increased, and the crystal surface morphology changed from rough to smooth. On the other hand, the growth rate was inversely proportional to the growth pressure, but did not influence the crystal morphology. The ErN crystals were sensitive to ambient air exposure, and they degraded to erbium oxide powder presumably from moisture in air. XRD pattern revealed that there was a strong preference for the (100) orientation, matching the dominant orientation of the tungsten substrate (100). XPS and EDX elemental analyses showed that the ErN crystals were nitrogen-rich. The Raman shift spectra of ErN crystal were in a good agreement with the theoretical predictions from the Frozen Phonon Approach.

ScN (100) single crystals were grown on single crystal W (100) in the temperature range of 1850-2000 ^{o}C. Out-of-plane θ-2θ and in-plane ϕ x-ray diffraction scans revealed the epitaxial growth of ScN with a cube-on-cube plane relationship ScN (200) || W (200) and with the normal direction ScN [200] || W [110]. The crystal surface exhibited layer-by-layer fashion growth with steps. Cracks formed in the ScN due to the difference in the thermal expansion between ScN and W. AFM showed that the growth temperature has a dramatic impact on the roughness of the crystal with an inverse relationship. X-ray rocking curve (XRC) showed that the crystal quality is excellent comparing to the previously reported qualities, and FWHM of ScN produced in this work is the lowest value reported to date.

The new crucible design with the cooling fin dramatically improved the growth rate of the ScN crystal grown on a tungsten seed comparing to the conventional crucible design. The process simulation by CFD technique employing FLUENT package was performed and validated experimentally. In the modified crucible, the temperature of the seed was colder than the crucible lid in about 10 ^{o}C, while in the conventional crucible the seed was equal or higher than the lid temperature. Decreasing the seed temperature increased the temperature gradient, the driving force of the growth, between the seed and the ScN source. The experimental results showed that the growth rate on the seed increased from 25% of the total growth rate in the conventional crucible to 80% of the total growth rate in the modified crucible. The calculated fin efficiency was 95% which demonstrates the low heat transfer coefficient. The new crucible design with the cooling fin is generally applicable to all seeded crystal growth by physical vapor transport.

6.2 Recommendations for Future Studies

There is still a room for improving this work, and several aspects can covered in the future.

It’s recommended to study and do more research on the following points:

1. Studying the electrical, thermal, and plasmonic properties of free standing pieces of ScN single crystal grown on a tungsten seed.
2. Doping ScN with manganese to improve the magnetic properties, but since the vapor pressure of manganese is high, gadolinium can also be examined due to its relatively low vapor pressure.
3. Since gadolinium is a rare earth element, ErN can be doped with it to improve its magnetic properties.
4. Growing ErN on different substrates such as SiC and sapphire to study its electrical properties.
5. Growing yttrium nitride doped with holmium element to produce a magnetic semiconductor.
6. Studying the effect of the fin size on the growth rate of the single crystal.
7. Modeling and simulating the mass transfer phenomenon of the new crucible design with the cooling fin.